

Biophysical and structural studies of self-assembled liposome/E-peptide/DNA nanoparticles : correlation with gene delivery

Yan, Jiang

2012

Yan, J. (2012). Biophysical and structural studies of self-assembled liposome/e-peptide/dna nanoparticles : correlation with gene delivery. Doctoral thesis, Nanyang Technological University, Singapore.

<https://hdl.handle.net/10356/50471>

<https://doi.org/10.32657/10356/50471>



**NANYANG
TECHNOLOGICAL
UNIVERSITY**

**BIOPHYSICAL AND STRUCTURAL STUDIES OF
SELF-ASSEMBLED LIPOSOME/E-PEPTIDE/DNA
NANOPARTICLES: CORRELATION WITH GENE
DELIVERY**

**YAN JIANG
SCHOOL OF BIOLOGICAL SCIENCES**

2012

**BIOPHYSICAL AND STRUCTURAL STUDIES OF
SELF-ASSEMBLED LIPOSOME/E-PEPTIDE/DNA
NANOPARTICLES: CORRELATION WITH GENE
DELIVERY**

YAN JIANG

SCHOOL OF BIOLOGICAL SCIENCES

A thesis submitted to the Nanyang Technological University in
partial fulfillment of the requirement for the degree of
Doctor of Philosophy

2012

Acknowledgements

This project was performed at School of Biological Sciences, Nanyang Technological University between August 2007 and August 2011 to fulfill the requirement for the PhD degree.

I would like to express my deepest gratitude to Prof. Lars Nordenskiöld, my supervisor, for his patient, enlightened and knowledgeable guidance, in particular, for his encouragements that carried me through difficulties of my research. Without his continuous support, this dissertation would not have been possible. It has been a great pleasure to work under the guidance of Prof. Lars Nordenskiöld.

My heartfelt thanks go to Prof. James P Tam, my co-supervisor, whose collaborative laboratory synthesized the peptides used in this project. I thank him for his great insight to peptide synthesis and continuous support.

I also would like to thank Dr. Nikolay Korolev for his valuable advises and generous help. He advised me and helped me in various aspects of my research.

I am thankful to my lab mates Liu Ying, Nikolay Berezhnoy, Abdollah Allahverdi and all other members of our group. I also sincerely thank Dr. Khee Dong Eom in Prof. Tam's lab, who synthesized the peptides used in this project.

Finally, I would like to thank my family and friends for their support and concern.

Contents

Contents.....	II
List of Tables.....	IV
List of Figures	V
Abbreviations.....	VII
Summary	IX
1. Introduction	1
1.1 DNA condensation	1
1.1.1 Condensation agents	1
1.1.2 Morphology.....	2
1.1.3 Forces driving DNA condensation.....	4
1.2 Gene delivery.....	5
1.2.1 Gene therapy	5
1.2.2 Viral gene delivery.....	6
1.2.3 Carrier-free gene delivery	8
1.3 Barriers of in vitro gene delivery.....	9
1.4 Review of synthetic vector-based gene delivery.....	12
1.4.1 Lipids	12
1.4.2 Polycations	14
1.4.3 Combination of lipid and polycations	16
1.5 Studies of supramolecular structure in transfection	16
1.5.1 Supramolecular structure of transfection complex.....	17
1.5.2 The influence of the initial supramolecular structure of lipoplexes on transfection.....	18
1.5.3 Structural evolution of complex in the delivery routes	18
1.6 Experimental design and motivation.....	19
1.7 Biophysical methods	22
1.7.1 Dynamic light scattering (DLS)	22
1.7.2 Static light scattering (SLS)	26
1.7.3 Flow cytometry	26
1.7.4 Small-angle X-ray scattering (SAXS).....	29
2. Materials and methods.....	32
2.1 Materials.....	32
2.2 Gene delivery studies.....	33
2.2.1 In vitro transfection	33
2.2.2 Flow cytometric analysis.....	34
2.2.3 Cytotoxicity assay	35
2.3 Biophysical methods	35
2.3.1 Static light scattering.....	35
2.3.2 Dynamic light scattering	36
2.3.3 Small-angle X-ray scattering.....	38
3. Results.....	39
3.1 Studies of gene delivery properties	39
3.1.1 Influence of sequence of the α -substituted side chain.....	39
3.1.2 Evaluation of cytotoxicity of 6 peptides and their mixture with DOTAP.....	42
3.1.3 Transfection as a function of complex formulation	44

3.1.4 Evaluation of cytotoxicity as a function of concentration	47
3.1.5 Relation between transfection and cytotoxicity	48
3.2 <i>Biophysical studies</i>	50
3.2.1 pH dependence of DNA condensation by histidine containing ϵ -oligolysines.....	50
3.2.2 Biophysical properties as a function of complex formulations and the correlation with transfection.....	51
3.3 <i>Studies of supramolecular structure</i>	57
3.3.1 Supramolecular structure of transfection complexes	57
3.3.2 Supramolecular structure at a fixed L/D as a function of P/D.....	61
3.3.3 Supramolecular structure of ϵ -peptide/DNA complexes.....	65
3.3.4 Supramolecular structure at a CR _{+/-} as a function of DOTAP-peptide composition	66
3.3.5 Correlation between zeta potential and d _{DNA}	72
3.3.7 SAXS study of complexes DOPE-DOTAP/ ϵ -(LYR)K10/DNA.....	74
4. Discussion and conclusions	77
4.1 <i>Gene delivery abilities</i>	77
4.2 <i>Correlations between biophysical parameters and transfection</i>	78
4.3 <i>The universal properties of supramolecular structures</i>	80
References	84
Appendix	90

List of Tables

Table 1. Structural parameters of the LD and LPD complees determined from SAXS spectra shown in Fig. 25.	60
Table 2. Structural parameters of the LD and LPD complees determined from SAXS spectra shown in Fig. 27.	64
Table 3. Structural parameters of the LD and LPD complees determined from SAXS spectra shown in Fig. 30.	70
Table 4. Structural parameters of the LD and LPD complees determined from SAXS spectra shown in Fig. 30.	71

List of Figures

Figure 1. Chemical structure of α -substituted derivatives of ϵ -oligolysine studied in this project. (A) Chemical structure of the ϵ -oligolysine backbone. An example of R' group was shown in (B). (B) Chemical structure of Leu-Tyr-Arg (LYR).....	X
Figure 2. The images of folded T4 DNA obtained by electron microscopy.....	3
Figure 3. Schematic phase diagram of a single polymeric chain.....	4
Figure 4. An example of viral-based gene delivery.....	7
Figure 5. Functioning of the gene gun.....	8
Figure 6. An example of DNA compaction.....	14
Figure 7. An example of the correlation function $C(\tau)$ plotted against the time delay.....	24
Figure 8. Illustration of the set-up of a DLS experiment.....	24
Figure 9. The distribution of ions in the surrounding interfacial region between the suspension particle and bulk liquid.....	25
Figure 10. A schematic drawing of static light scattering.....	26
Figure 11. An illustration of fluidics system in flow cytometry and detection of light scattering and fluorescence signal.....	28
Figure 12 An example of FACS Dotplot.....	29
Figure 13. A schematic drawing of the BL23A SAXS/WAXS instrument in national synchrotron radiation research center of Taiwan.....	31
Figure 14. An example of plotting of the intensity of scattered light against the concentration of peptide.....	36
Figure 15. An example of the size distribution graph.....	37
Figure 16. Transfection efficiencies of DOTAP, ϵ -(LYK)K10, ϵ -(LKY)K10, ϵ -(YKL)K10, ϵ -(LYH)K10, ϵ -(LYR)K10, ϵ -(LYRH)K10 and mixtures DOTAP-peptide determined for four cell lines, A549, Mewo, HEK293 and HeLa (indicated in the graphs).....	41
Figure 17. HeLa cell viability after the treatment with DOTAP, ϵ -(LYK)K10, ϵ -(LKY)K10, ϵ -(YKL)K10, ϵ -(LYH)K10, ϵ -(LYR)K10, ϵ -(LYRH)K10 and mixtures DOTAP-peptide at the same concentration as we used in cell transfection.....	43
Figure 18. Transfection efficiency plotted as a function of peptide to DNA charge ratio for ϵ -(LYRH)K10, ϵ -(LYR)K10 and ϵ -(LYR)K10 (indicated in the graphs). (A) is for complex ϵ -peptide/DNA. (B) and (C) are for the ternary DOTAP/ ϵ -peptides/DNA complexes differing in mixing order of the components.....	46
Figure 19. HeLa cell viability as a function of the concentration of transfection agents.....	48
Figure 20. Comparison of HeLa cell transfection efficiency (black points and lines) and HeLa cell viability (blue points and lines) shown as a function of concentration of transfection agents.....	49
Figure 21. Influence of pH on DNA condensation induced by ϵ -(LYH)K10 and ϵ -(YKL)K10.....	51
Figure 22. Comparison transfection efficiency (black lines and symbols) and zeta potential (blue lines and symbols) plotted as a function of peptide to DNA	

charge ratio for ϵ -(LYRH)K10 ϵ -(LYR)K10 and ϵ -(LYR)K10 (indicated in the graphs).....	54
Figure 23. Comparison of transfection efficiency (black lines and symbols) and particle size (red lines and symbols) as a function of peptide to DNA charge ratio.	55
Figure 24. Particle size (red lines and symbols) and absolute values of zeta potential (blue lines and symbols) in dependence of peptide to DNA charge ratio.	56
Figure 25. SAXS spectra of (A) DOTAP/ ϵ -(LYR)K10/DNA complexes in HBS buffer, (B) DOTAP/ ϵ -(LYRH)K10/DNA complexes in HBS buffer, (C) DOTAP/ ϵ -(LYR)K10/DNA complexes in low-salt buffer and (D) DOTAP/ ϵ -(LYRH)K10/DNA complexes in low-salt buffer at L/D=2 as a function of peptide/DNA (P/D) ratio.....	59
Figure 26. Schematic picture illustrating the lamellar phase of DOTAP/ ϵ -peptide/DNA complexes, with alternating lipid bilayers and DNA monolayers.	61
Figure 27. Synchrotron SAXS scans of the complexes DOTAP/ ϵ -(LYR)K10/DNA at the lipid to DNA charge ratio (L/D) 0.5 (A); 1.0 (B); 1.5 (C); and 2.0 (D) determined for the different peptide to DNA charge ratio, P/D.	63
Figure 28. Repeat distances determined from the SAXS spectra in Fig. 27 plotted as a function of the peptide/DNA charge ratio, P/D.	65
Figure 29. Synchrotron SAXS scans of complex ϵ -(LYR)K10/DNA (A) and ϵ -.....	66
Figure 30. Synchrotron SAXS scans of the complexes DOTAP/ ϵ -(LYR)K10/DNA at the low (1(A); 1.5 (B); 2 (C)) and high (3.0 (D); 4.0 (E); 7.0 (F)) total positive (peptide + DOTAP) to negative (DNA) charge ratio, CR _{+/-} , determined for different proportions of peptide and lipid in the mixture (indicated in the graphs).....	69
Figure 31. Repeat distances determined from the SAXS spectra in Fig.30 plotted as a function of the total (ϵ -(LYR)K10 + DOTAP)/DNA charge ratio, CR _{+/-}	72
Figure 32. Dependence of d _{DNA} (black squares) and zeta potential (blue circles) of LPD complex as a function of CR _{+/-}	73
Figure 33. Synchrotron SAXS scans of complex DOPE-DOTAP/ ϵ -(LYR)K10/DNA at L/D=1(A); 1.5(B) pH=7 as a function of P/D.	75
Figure 34. Synchrotron SAXS scans of complex DOPE-DOTAP / ϵ -(LYR)K10/DNA at CR _{+/-} = 1.5 as a function of DOTAP-peptide composition.	76

Abbreviations

BGTC, bis(guanidinium)-tris(2-aminoethyl)amine-cholesterol;

CR, charge ratio;

CR_{+/-}, charge ratio of positive to negative;

d_{DNA}, interaxial DNA-DNA distance ;

d_{interlayer}, interlayer spacing;

DLS, dynamic light scattering;

DMSO, dimethyl sulfoxide;

DMEM, Dulbecco's modified, Eagle medium;

DOTAP, 1,2-dioleoyl-3-trimethylammonium-propane;

DOPE, 1,2-di-(9Z-octadecenoyl)-sn-glycero-3-phosphoethanolamine;

DOPC, 1,2-dioleoyl-*sn*-glycero-3-phosphocholine

DOSP, dioleylsuccinyl paramomycin

DC-Chol, 3β-[N-(N',N'-dimethylaminoethane)-carbamoyl]cholesterol

ε-K10: oligomers of ε-poly(L-lysines) with degree of polymerization 10;

ε-(L)K10, ε-(Y)K10, ε-(R)K10, ε-(YR)K10, ε-(LYR)K10, ε-(LYH)K10, ε-(LYRH)K10, ε-(LKY)K10, ε-(LYK)K10 and ε-(YKL)K10 :

α-substituted ε-K10 homologues, amino acids in the brackets are the α-substitution groups respectively; L, Y, R, H, and K represent amino acid residue leucine, tyrosine, arginine, histidine, and lysine, respectively; YR, Tyr-Arg; LYR, Leu-Tyr-Arg; LYH, Leu-Tyr-His; LYRH, Leu-Tyr-Arg-His; LKY, Leu-Lys-Tyr; LYK, Leu-Tyr-Lys; YKL, Tyr-Lys-Leu;

EC₅₀, the midpoint concentration of condensing agents in the titration curves;

FACS, fluorescence activated cell sorting;

FBS, fetal bovine serum;

FL, fluorescent signal;

FSC, forward-scattered light;

GALA, glutamic acid-alanine-leucine-alanine repeat unit;

GFP, green fluorescence protein;

HBS, Hepes-buffered saline;

KALA, lysine-alanine-leucine-alanine repeat unit;

LPD, lipid/peptide/DNA complexes;
 LD, lipid/DNA complexes;
 L/D, charge ratio of lipids to DNA;
 MTT, 3-(4,5-dimethylthiazol-2-yl)-2,5-diphenyl tetrazolium bromide,
 $C_{18}H_{16}BrN_5S$;
 NLS, nuclear localization signal;
 PD, peptide/DNA complexes;
 P/D, charge ratio of peptides to DNA;
 PCS, photon correlation spectroscopy;
 PBS, phosphate-buffered saline;
 PEI, polyethylenimine;
 PLL, poly(L-lysine);
 PMMA, polymethylmethacrylate;
 QELS, quasi elastic light scattering;
 SAXS, small-angle X-ray scattering;
 SLS, static light scattering;
 SSC, side-scattered light;
 WGA, wheat germ agglutinin

Summary

Recently, novel DNA compaction agents, ϵ -oligo(L-lysines) and their branched α -amino-acid substituted derivatives, have been successfully tested as vectors for *in vitro* gene delivery. The present work exploits a number of newly developed ϵ -oligolysine-based peptides: ϵ -(LYRH)K10, ϵ -(LYH)K10, ϵ -(LYK)K10, ϵ -(LKY)K10 and ϵ -(YKL)K10. ϵ -oligolysine backbone was synthesized with degree of polymerization 10 and α -amino acid triplets (amino acids in the brackets) were attached to each of the α -amino group of ϵ -oligolysine (Fig. 1). Since it was found that combined effect of lipids and polycations can greatly enhance transfection efficiency, our novel ϵ -peptides were used in the combination of cationic liposome DOTAP (1,2-dioleoyl-3-trimethylammonium-propane), resulting in a ternary complex liposome/ ϵ -peptides/DNA (LPD).

The potential usage of those ϵ -peptides and liposome/ ϵ -peptides in gene delivery was evaluated by measuring the *in vitro* transfection efficiency and cytotoxicity. The arginine/histidine-bearing peptides ϵ -(LYH)K10, ϵ -(LYR)K10 and ϵ -(LYRH)K10 show a potential of being successful DNA carriers compared to the peptides with lysine in the side chain, ϵ -(LYK)K10, ϵ -(LKY)K10 and ϵ -(YKL)K10. In the combination of cationic liposome DOTAP, ϵ -(LYR)K10, ϵ -(LYRH)K10 or ϵ -(LYH)K10 result in gene vectors with transfection abilities exceeding that of DOTAP alone, without noticeable increase in cytotoxicity.

In parallel, the zeta potential (an indication of magnitude of surface charge) and sizes of transfection complexes were characterized by dynamic light scattering (DLS) and compared with transfection results. Our results suggest that peptides in LPD complex probably cover the exposed DNA on the particle surface contributing to the increased zeta potential in the presence of peptides. The potentiating effect of peptide addition to the lipids/DNA mixtures may be due to the increase of surface charges. A novel finding is that the high transfection

efficiency of the nanoparticles correlates with increase of zeta potential above +20 mV and requires particle size to be below 500 nm.

Synchrotron small angle X-ray scattering (SAXS) studies reveal self-assembly of the three components (lipid DOTAP, peptides and DNA) to ordered lamellar complexes, where a monolayer of parallel DNA chains are alternatively arranged between lipid bilayers. The interaxial DNA-DNA distance in the DNA layer is dependent on the total charge ratio of positive to negative but the interlayer spacings are similar for various formulations. It is suggested that the peptide infiltrate into the DNA-DNA layers in the aqueous phase between lipid bilayers and intercalate between DNA chains. According to the structure and zeta potential data, a novel model for LPD complexes has been proposed. It is consistent with the synergistic effect of branched ϵ -oligolysines and DOTAP observed in our gene delivery study.

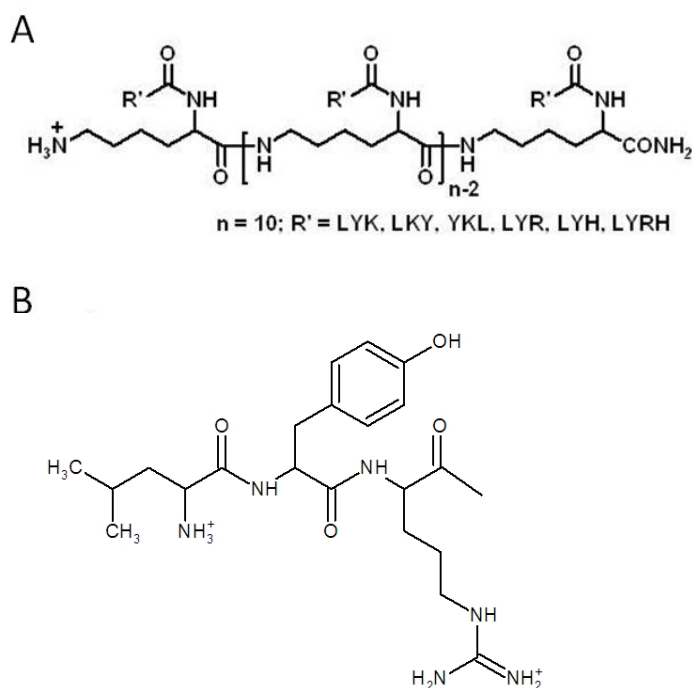


Figure 1. Chemical structure of α -substituted derivatives of ϵ -oligolysine studied in this project. (A) Chemical structure of the ϵ -oligolysine backbone. An example of R' group was shown in (B). (B) Chemical structure of Leu-Tyr-Arg (LYR).

(A) L, Y, R, H, and K represent amino acid residue leucine, tyrosine, arginine, histidine, and lysine, respectively. R' group represents α -substitution group, Leu-Tyr-Lys (LYK), Leu-Lys-Tyr (LKY), Tyr-Lys-Leu (YKL), Leu-Tyr-Arg (LYR), Leu-Tyr-His (LYH), and Leu-Tyr-Arg-His (LYRH). (B) The short peptide LYR is attached to each of the α -amino group of ϵ -oligolysine. Structures of other side chains are shown in appendix III.

1. Introduction

1.1 DNA condensation

As a highly negatively charged polyelectrolyte, DNA displays the random coil conformation in solution. DNA condensation is the collapse of extended DNA molecules into compact particles with a considerable decrease in size (1). This phenomenon has drawn great attention and been detected by a variety of techniques including electron microscopy, fluorescence microscopy, dynamic light scattering and circular dichroism etc (2). It is significant for biological systems, where the huge length of DNA needs to fit into the limited space of the cell nucleus. In gene therapy, free exogenous DNA is easily to be digested by enzymes or bound by some proteins so DNA condensation is necessary (3).

1.1.1 Condensation agents

It has been found that a variety of substances, which work by decreasing electrostatic repulsion between DNA segments, by modifying the interactions between DNA and solvent, or by the combination of those, can cause DNA condensation to form compact and orderly structures (1-2). Agents used commonly in condensation research are multivalent cations, such as naturally occurring polyamines spermidine³⁺, spermine⁴⁺ (4), the inorganic cation $\text{Co}(\text{NH}_3)_6^{3+}$ (5) and synthetic polycation PEI (polyethylenimine); cationic polypeptides such as polylysine; cationic lipids; proteins such as histone H1 (2).

Previous studies indicate that condensation normally requires cations at least of charge +3 in aqueous solutions (1). Divalent cations can produce condensation in water-alcohol mixture (1) although they do not provoke condensation in water except under some special circumstances such as high concentration (6) or elevated temperature (4).

Alcohol also can produce DNA condensates (e.g. 80% ethanol is widely used as a precipitant to purify DNA. DNA condensation by alcohols can cause particles with well-defined structures under some special conditions) (4). In the presence of high (or moderate to high) concentration of salt, psi-DNA (liquid-crystalline-like form of DNA), which has a distinctive CD spectrum, can be formed by neutral or anionic polymers such as polymer PEG at high concentration (1).

Recently a great amount of research has focused on the condensation of DNA with cationic lipids, such as DOTAP (7), since it can be used as an effective transfection agent in eukaryotic cells (2). Cationic liposome can neutralize the negative charges of DNA, protect it from enzymatic digestion, enhance internalization by cells and facilitate intracellular trafficking, all of which increase gene transfer (8). The understanding of biophysical mechanisms and consequences of DNA condensation can be linked to the design and application of vectors for gene therapy.

1.1.2 Morphology

The DNA condensates with varying sizes ranging 50 nm to 300 nm, mainly present three kinds of morphologies: toroids, rods, and sphere, of which toroids and rods are the most common structures in DNA condensation from aqueous solution observed by electron microscopy (9). Toroids are the conformation that circumferentially wound double-helical strands surrounds a well-defined hole in the middle, whose thicknesses and circumferences are similar to the diameters and lengths of the rods. A majority of attention has been paid to the toroidal structure because it is one of the most remarkable features in condensation events. But rods are still seen in electron micrograph of condensed DNA and probably in high proportion over toroids when the solvent or the condensing agent is slightly nonpolar (1,9-10).

A thermodynamic theory indicates that DNA bending free energy contribute the total free energy (The bending free energy is $\Delta G_{\text{bend}} = RTaL/2Rc^2$, where L is the original length of DNA, a is persistence length of DNA condensate, and Rc

is the radius of curvature.) (1). Besides, external osmotic pressure and demixing volume are also mentioned to influence DNA condensate formation (1). It was predicted that short DNA strands condense into toroids due to the greater stiffness of DNA (elastic contribution) and dimixing volume (repulsive contribution) except very short DNAs (The minimum DNA length for condensation into compact particle is 400bp), which is hard to bend sufficiently to form toroids, while long DNA molecules tend to condense into spherical globules without inner holes due to a greater compressive force (1). However, Iwaki et al reported that T4 DNA is condensed into different morphologies by different condensing agents (Fig. 2) (11). Further, they showed a schematic phase diagram a single polymeric chain, which indicated that the spherical globule is stabilized thermodynamically when the attractive interaction overwhelms the bending energy (Fig. 3) (11).

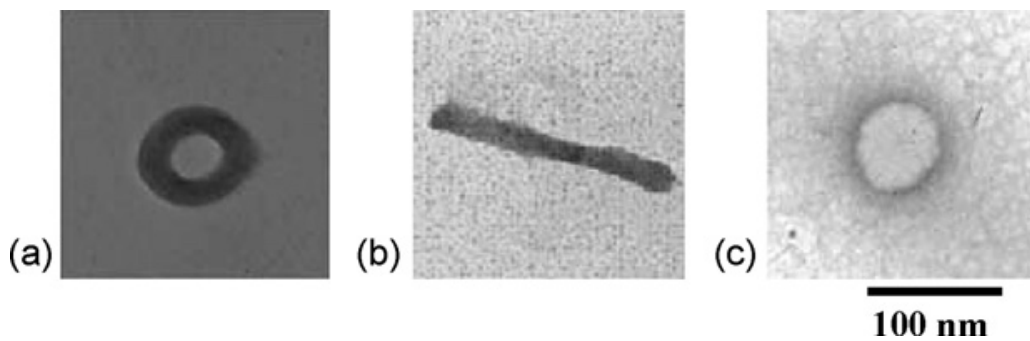


Figure 2. The images of folded T4 DNA obtained by electron microscopy

Figure adapted from ref (11): (a) toroidal globule; (b) rod-like globule; (c) Spherical globule. Condensing agents: (a) spermine, (b) hexammine cobalt (III), and (c) chiral dication.

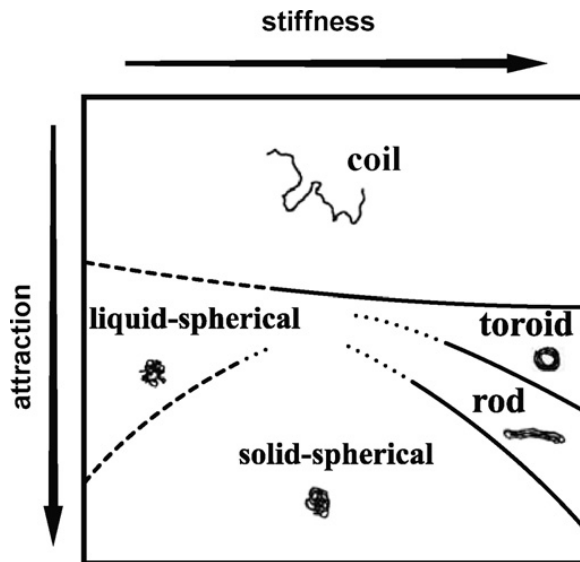


Figure 3. Schematic phase diagram of a single polymeric chain.

Dashed line indicates that a transition across this line has a character of a second-order transition. A region around dotted lines requires a further study to determine the phase boundary. According to the chain stiffness and the depth of the attractive potential, various structures appear in the single-chain conformation. This figure is **adapted from ref (11)**

It is revealed that the choice of morphology is not only determined by thermodynamic stability, but also rests on kinetic factors (1,9). Condensate morphology statistics has been studied as a function of time in plasmid DNA condensation reaction using hexamine cobalt chloride as condensation agent (9). In comparison with the morphological distribution after the reaction reached equilibrium, the higher population of rods was detected at earlier times, that is, a few minutes following the initiation of condensation (9). This result indicates the rods take a kinetic advantage in nucleation, which is considered as the first step of the condensate formation (9).

1.1.3 Forces driving DNA condensation

The various forces driving DNA condensation and their contributions have also been studied both experimentally and theoretically. The chief force against DNA condensation is the electrostatic repulsion between DNA polyions (1,12). Besides, some other factors also resist the formation of condensed DNA particles. Limitations in the formation of sharp bending and kinking are attributed to the stiffness of DNA strands (1). Entropy is lost due to the demixing of DNA and solvent during the collapse of wormlike coils (1).

However, electrostatic neutralization by counterions acts as a major factor to cause condensation (2). Calculations based on Manning's counterion condensation theory (13) produce a significant regularity that neutralization of about 90% of DNA charge is required for condensation to occur (a condition which is met with cations of charges $+3$) (1-2).. It is in agreement with experimental results under various conditions (e.g. mixtures of ions, elevated dielectric constant) (1-2). Thus, when this critical degree of charge neutralization has been met, attractive forces such as fluctuation induced ion-ion correlations may induce attraction between DNA strands (2,12). Attraction in the presence of multivalent ions may also be induced by the entropy increase contributed by hydration force driven by the rearrangement or release of water between macromolecular surfaces (1). Although our knowledge about DNA condensation has increased, the further investigation of the condensing conditions and agents, deeper understanding of the mechanism and more application to other biological fields, remains to be done.

1.2 Gene delivery

1.2.1 Gene therapy

The application of gene delivery has been expanding to basic biological science, biotechnology, agriculture and clinical medicine. One of the most significant applications is gene therapy. "Gene therapy" means an approach for treatment or prevention of diseases by altering or manipulating genes within target cells (8).

The transgene in target cells will replace the deficient genes to restore normal cellular processes, which can be used in the treatment of hemophilia etc (14). Alternatively, expression associated with transgenes will destruct target cells with a cytotoxic pathway, which can be exploited for the treatment of malignant

tumors such as endometrial carcinoma (14); or even stimulate specific cellular responses, e.g. immune response (8,14). Benefiting from the development of proteomics and genomics, the genetic understanding of pathogenesis enables more and more genes and proteins involved in diseases to be identified as targets for gene therapy (8).

Gene transfer for therapeutic purposes can be achieved through ex vivo or in vivo (3,8,14). The in vivo approach is a direct way of delivering the genes or complexes with vectors into the patients such as intravenous delivery of DNA (14). Crucial to the success of in vivo gene therapy is the stability in circulation avoiding aggregation with serum proteins and digestion by a variety of enzymes (3). The efficiency of in vivo gene transfer also has strong bearing on the ability to entry into cells involving crossing biological membranes (e.g., endothelium, plasma membranes) and discriminate between desired and non-desired cells (3). Ex vivo method is performed by isolating target cells from patients, and subsequently reintroduction of the cells transfected in vitro, with the higher transfection efficiency as compared to in vivo system (8). Regardless of the differences in procedures (ex or in vivo), both of them requires to address similar challenges, namely detrimental side effects, such as toxicity, induction of immune response, and mutagenesis.

Two major groups: viral and nonviral vectors have been developed as vehicles for gene delivery. The methods of nonviral gene delivery can be divided into carrier-free gene delivery and synthetic vector-based gene delivery (15).

1.2.2 Viral gene delivery

Viruses are well-known for the outstanding gene transfer ability, which is employed for viral gene delivery. Usually, a recombinant vector lacking replication as well as maintaining the ability to infect cells is produced by insertion of genes encoding the desired proteins into the viruses with removed genome (8). An example of viral-based gene delivery is given in Fig. 4. Many

efforts have been made with molecular biology and protein engineering approaches, to produce engineering viral vectors with improved properties for human therapeutic use, including the enhanced targeting abilities, resistance to the neutralization by host immune responses, and higher transduction of relevant cells (16).

Even though viral gene delivery is an efficient approach as observed in in vitro studies and animal disease models (16), its use is hampered by the following disadvantages: problems associated with insertion mutagenesis, cytotoxicity, and immunogenicity (15,17-18); high cost; restricted targeting of specific cell types (16); the limited space to insert genes in the viral genome (3); packaging and recombination problems due to the complexity of viruses such as multimeric capsids, overlapping reading frame (16). To date, the advances in this field still cannot address fundamental problems, especially safety concerns, e.g. the adenovirus therapy trial that provoked leukemia in several patients. Therefore, the investigation of the nonviral gene delivery has been inspired to overcome the drawbacks of viral gene delivery.

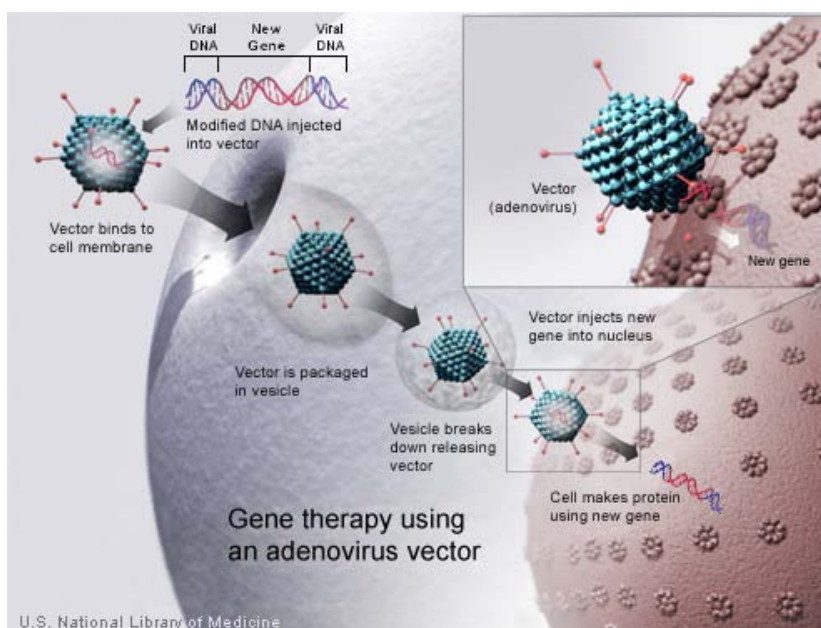


Figure 4. An example of viral-based gene delivery.

The gene delivery from the cell membrane to nucleus is mediated by adenovirus vectors. Figure adapted from <http://ghr.nlm.nih.gov/handbook/therapy/procedures>

1.2.3 Carrier-free gene delivery

Carrier-free gene delivery is based on physical forces comprising gene gun, ultrasound, direct needle injection, electroporation, and hydrodynamic delivery (15). Gene gun allows gold particles with DNA molecules, accelerated by the pressurized gas, to penetrate into a tissue and release DNA in cells, which is illustrated in Fig. 5 (19). Ultrasound facilitates gene transfer by creating membrane pores and thereby making diffusion of DNA across the membranes easier (15). Electroporation, moving DNA along the electric field, works with a pair of electrodes inserted into the selected tissues (20). Gene gun and electroporation shows good efficiency, however, their applications are restricted and procedures are technically complicated. Ultrasound-facilitated gene transfer is a promising tool for site-specific treatment but its efficiency is low. Similar disadvantage is also found in needle injection gene delivery despite its simplicity and safety (15). Hydrodynamic gene delivery is a simple, reproducible and efficient approach for introduction of plasmid DNA into highly perfused internal organs, but it is greatly influenced by the anatomic structure of the organ applied, the speed and volume of injection (15).

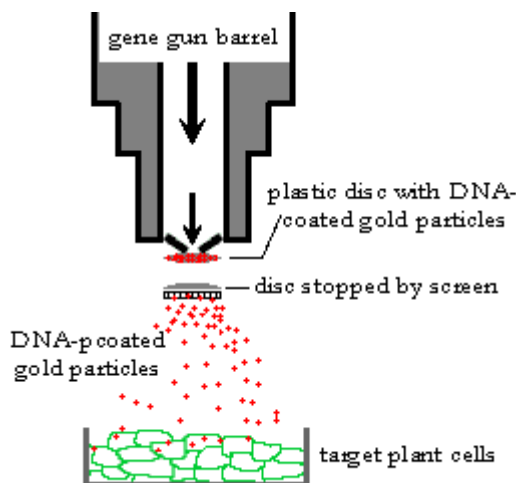


Figure 5. Functioning of the gene gun.

Figure adapted from <http://artsci.wustl.edu/~anthro/blurb/Backgrounder.html>

1.3 Barriers of *in vitro* gene delivery

For *in vitro* gene transfer, the multistep delivery from outside the cell to inside the nucleus involves cell uptake through endocytosis, endosomal escape, nuclear entry, and expression. Each step can be considered as a barrier of gene delivery. DNA loss can be caused by low cell uptake relying on non-specific interactions between complexes and cell membranes. This barrier could be overcome by conjugating targeting ligands to complexes, which provide a specific interaction with the cell surface in addition to non-specific electrostatic interaction (8). Limited stability in cytosol due to degradation in lysosome or cytosol, failure to translocate across nuclear membranes can also decrease the efficiency of gene delivery (21).

The cellular uptake of DNA complexes in general occurs by endocytosis, where DNA molecules are sequestered within membrane-enclosed endosomal vesicles and finally delivered to lysosome for degradation (7-8,22). Such internalization route limits the translocation of DNA from endosome to cytosol and thus greatly reduces the copies of DNA molecules that can reach the nuclear machinery (3,22). In the endocytic pathway, ATP-dependent proton pump located in the endosomal membrane keeps the lumen of endosomes acidic and the maturation of early endosomes to late endosomes is accompanied by a decrease in pH (18,22). Chloroquine is widely used to avoid the fusion with lysosome because it inhibits the maturation of endosomes through neutralizing the endosomal pH as a weak base (3,22). But the effect on transfection is different for various transfection cases (23-24) and it is impractical for *in vivo* application due to its toxicity (3,22).

The design of gene delivery vectors takes advantage of low pH of the lumen of endosomal compartments to trigger the destabilization of endosomes and the resultant DNA release prior to lysosomal degradation (18). Bell et al observed that endosomal pH induced the formation of an inverted hexagonal phase for gemini surfactant lipoplex using SAXS and cryo-EM (25). Its transfection ability was thought to be related to pH-induced phase transition because the

inverted hexagonal phase is preferred for the fusion with endosomal membrane (25). pH-dependent fusogenic peptides mimic the fusion domain of viral transmembrane proteins (22,26). They can be activated at endosomal pH and destabilize membranes by altering lipid packaging of membranes or pore formation (22,26-27). GALA (glutamic acid-alanine-leucine-alanine) peptide changes the conformation from random coil to α -helix as pH is reduced from 7.0 to 5.0, which induces the destabilization of endosomal membrane (28). KALA (lysine-alanine-leucine-alanine) peptide has a similar membrane leakage ability and it can condense DNA with the positively charged amine residues (29). Polymers contain secondary and tertiary amines, such as PEI (polyethylenimine), and histidine-rich peptides are used to facilitate DNA release from endosomes due to the pH buffering capacity (3,8,15,18,30). The “proton sponge” hypothesis has been proposed to explain the mechanism, that is, those polymers are protonated in endosomal pH so they absorb protons in the lumen of endosomes as “proton sponge”, leading to influx of chloride counterions, which raise the osmotic pressure and eventually cause endosomal swelling and DNA release (8,15,18). This hypothesis is supported by the data that transfection mediated by histidine-rich peptides was significantly decreased by the addition of proton pump inhibitor bafilomycin A₁ (18,31-33).

Recently, Bihan et al suggested that the endosomal escape mode and the timing of DNA release probably influence the final transfection outcomes for complexes that are able of inducing endosomal leakage (34). They tracked the intracellular trafficking of BGTC (bis(guanidinium)-tris(2-aminoethyl)amine-cholesterol) lipoplex and DOSP (dioleoylsuccinyl paramomycin) lipoplex by electron microscopy and found that the higher transfection level of DOSP probably resulted from the more direct endosomal escape pathway and the earlier DNA release (34). In both cases, the interaction of vector lipids with endosomal membranes led to the destabilization of endosomal membrane and lipoplex reorganization, where DNA release could take place (34). Tarahovsky et al systematically studied the DNA release from lipoplex upon interacting with anionic lipids and found that the DNA releasing ability depended on the lipid composition of both lipoplex and anionic lipids (35). It was also pointed out that the extent of membrane fusion and mesomorphic structure of the lipid

mixture significantly influenced the kinetics of DNA release (35). Those studies indicate that multiple factors contribute to the rate and extent of DNA release from complexes (34-35). In addition, the location of DNA release is of particular relevance to its following fate (36). When unpacking happens before nuclear entry, free DNA may be subject to the degradation by cytosolic nucleases; but if vectors keep on coating DNA in nucleus, occluded DNA cannot be used for gene expression (21). Since either insufficient or over-protection from the delivery vectors leads to DNA loss, a desirable transfection efficiency requires the “correct” dissociation of DNA (21).

The prerequisite for DNA to gain access to the transcriptional machinery is translocation from cytoplasm to nucleus across nuclear membrane (3). The nuclear membrane breaks down in mitosis of dividing cells, thus increasing possibilities for exogenous DNA to enter nucleus. However, penetration through nuclear membrane is the major rate limiting step for transfection with nondividing cells (36). The transfection complex or unpacked DNA is too big to transport through nuclear pore complex by passive diffusion, which occurs only for small molecules. Although DNA nuclear translocation was observed for free DNA and DNA/vector complex, vectors are always involved in the process and the complex unpacking may influence it (36). Intracellular components can facilitate the nuclear entry by simultaneously associating with transfection complex and nuclear membrane, e.g. cellular phospholipids coat PEI/DNA complexes through electrostatic interaction and fuse with nuclear membranes to transfer the complex into nuclei (37).

A very interesting phenomenon has been observed that wheat germ agglutinin (WGA) lowers the efficiency of gene delivery, in the same way as it does in import of proteins (38). This finding suggests that the pathway of DNA translocation through the nuclear pore complex is essentially similar to proteins (7). Therefore, a number of strategies can be applied to overcome this barrier based on the understanding of nuclear import of proteins. For example, nuclear localization signal (NLS), a short peptide sequence containing short sequences of positively charged lysines or arginines, exposed on the surface of proteins to

bind strongly to importins, has been incorporated into gene transfer complexes to facilitate nuclear entry (39).

1.4 Review of synthetic vector-based gene delivery

Synthetic vector-based gene delivery relying on chemical principles has gained much interest for its safety, biocompatibility and potential for large-scale production (15,17). Its development offers potential to circumvent the limitations of viral gene delivery in both basic research laboratories and clinical settings (8). To date, lipids and polycations are most frequently used gene delivery materials among many synthetic or naturally occurring compounds discovered as nonviral gene delivery vectors (7).

1.4.1 Lipids

Cationic lipids condense DNA resulting in a self-assembled complex called lipoplex and transfection with lipoplex is termed lipofection (23). Cationic lipids are amphiphilic in nature with hydrophilic and hydrophobic domains, e.g. lipid DOTAP (1,2-dioleoyl-3-trimethylammonium-propane; structure is shown in appendix I) has a primary amine head group and two hydrophobic chains.

The hydrophilic part is always an amine group with different substitution (primary, secondary, and tertiary amines) (8). The charged amine groups bind to DNA molecules through electrostatic interaction (2). Cationic lipids of multivalency condense DNA more effectively than those with single amine group but the correlation between transfection ability and the valence is not clear since the dissociation of DNA from lipoplex before transcription is required (40). Besides, the configuration of amine groups influence the transfection capacity for multivalent cationic lipids (8).

The hydrophobic part consists of linear aliphatic chains or a planar group such as the sterol backbone of lipids DC-Chol (3 β -[N-(N',N'-dimethylamino)ethane]-

carbamoyl]cholesterol; structure is shown in appendix I) (39-40). It takes part in the self-assembled process of lipoplex, leading to a lipid rearrangement or even a phase transition (15,39-40). Concomitant with that, the binding of lipids with DNA is strengthened and DNA is occluded within lipoplexes (39-40).

Neutral and anionic lipids are incapable of condensing DNA so DNA complex are formed in the presence of cations or cationic lipids (23,41). Neutral lipids have been extensively used in cationic lipids-mediated gene delivery as co-lipids (23,40). It was suggested by Ferrari et al (42) that transfection activity of lipoplexes was determined by the synergy between cationic lipids and co-lipids. To elucidate the roles of co-lipids in gene transfer, a number of studies paid attention to the structural properties of lipoplexes that contain co-lipids. Safinya and co-workers studied the supramolecular structure and interaction with cell membranes of complex DNA/DOTAP/DOPE (DOPE, 1,2-di-(9Z-octadecenoyl)-sn-glycero-3-phosphoethanolamine; structure is shown in appendix I) and DNA/DOTAP/DOPC (DOPC, 1,2-dioleoyl-sn-glycero-3-phosphocholine; structure is shown in appendix I) (43-45). They found that DOPE-containing complexes with an inverted hexagonal phase induced a higher gene transfer level than complexes DNA/DOTAP/DOPC that showed a lamellar phase (43-44,46). The complexes with lamellar phase remained stable inside cells while those with hexagonal structure fused with cell membranes and thus caused DNA release (44-45).

In agreement with above observations, Xu et al (47) reported that the microscopic structure of lipoplex was determined by the lipids composition and the transfection active lipoplexes were more likely to present high-radius-of-curvature structures. These findings emphasize that co-lipids influence transfection by regulating the structure of lipoplexes (43-47), so the choice of the co-lipid can be rationalized by its phase preference. Besides, Marchini et al suggested that tailoring the lipoplex composition to lipid composition of plasma membrane can improve transfection because the shape coupling between the lipoplex and membrane lipids determined the cellular internalization of DNA (48).

1.4.2 Polycations

In the polycations, primary amines are protonated at physiological pH, so these polymers are highly positively charged (8). Polycations, such as polylysines (PLL) and polyethylenimine (PEI), can compact DNA efficiently and form complexes (49). Fig. 7 shows an example of DNA compaction. A variety of polylysines (PLL) that differ in molecular weight and the degree of branching were synthesized for gene delivery (7-8). The studies using those derivatives demonstrated that high molecular weight PLL can condense DNA more effectively than low molecular weight PLL but have a higher cytotoxicity (8,50). Since the amine groups of PLL are completely protonated, PLL-induced transfection is limited by the inefficient DNA release inside cells (7). It is consistent with the finding of Akinc et al that PLL/DNA complexes fail to avoid the lysosomal trafficking (30).

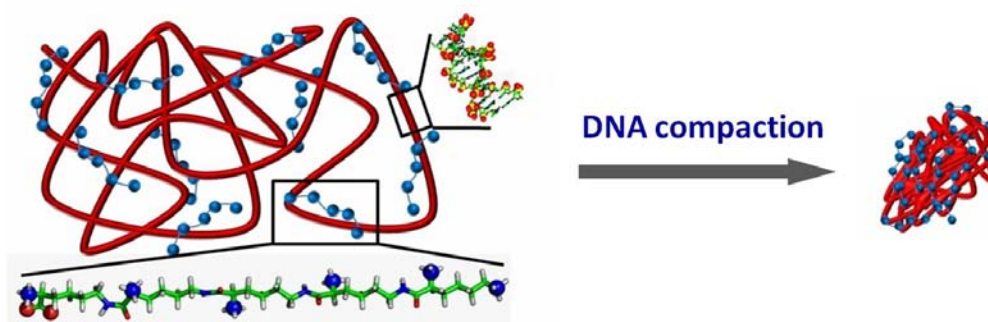


Figure 6. An example of DNA compaction.
The DNA compaction is induced by ϵ -oligolysine.

Polyethylenimine (PEI) was widely used in gene delivery due to the densely positive charges and “proton spongy” effect resulting from protonatable amines at acidic pH (7,15). It was found that PEI/DNA complexes were diverted from the lysosomal trafficking by detecting the pH environment of delivered DNA (30) and confocal microscope imaging (37). Godbey et al visualized the intracellular journey of PEI/DNA complex and found that PEI or PEI/DNA complex enter cell nuclei in an ordered structure (37). Gene delivery properties of PEI were studied with the variation of molecular weights and configurations,

revealing molecular weight-dependence similar to PLL (15). As to PEIs with similar molecular weight, the branched PEI possesses better DNA condensation ability than linear PEI (7,15). Since the toxicity is related to its nonbiodegradable nature, low molecular weight PEI were cross-linked with biodegradable bonds to form a high molecular weight PEI (15).

The extensive usage of polycations in gene delivery is also related to the ease of chemical modification so that their transfection abilities can be improved. Polylysine condenses DNA effectively but it was observed that the complexes ended up being degraded in lysosomes (30). So the incorporation of endosomal lytic constituents into PLL has been tested, of which histidine is most commonly used (7). Since the imidazole group of histidine has a pKa of 6, it is neutrally charged at physiological pH but protonated at the low pH of endosomes, which allows histidine residues to promote endosomal escape (18).

Previous studies showed histidine can provide pH buffering to facilitate endosomal escape by either substituting some ϵ -amino groups of PLL with histidyl groups (31) or adding histidine residues into lysine-containing peptides (51-52). Midoux and Monsigny reported that a partial substitution of ϵ -amino groups by histidyl residues in polylysines resulted in an enhanced transfection and it was related to the protonation of imidazole groups inside endosomes (31). Yu et al found that histidylated oligolysines enhanced lipofections when they were conjugated to liposomes (32). Mixson and co-workers designed a series of histidine-lysine (HK) peptides, combining the DNA condensing ability of lysines and pH-buffering properties of histidines (33,51-53). They first found that linear HK peptides increased the liposome-mediated transfection as co-polymers (51) and the peptides were further improved by adding branches and increasing histidine/lysine ratio (33,52-53). Besides, histidine was introduced into cationic amphipathic peptides by Kichler et al, where its protonation not only led to the endosomal buffering but also changed conformation of the peptide (24,54).

Histidine-containing PLL were further improved by incorporating cysteines and forming disulfide bonds between cysteines (55). The reducible polycations can

be cleaved in the intracellular reducing environment so the reduced cytotoxicity and accelerated DNA release might be achievable (7). Read et al synthesized a low molecular weight HK peptide with terminal cysteine residues, which were cross-linked to form a linear peptide through reducible disulfide linkages (55). They showed that both pH buffering ability and reducible properties contributed to the high transfection ability and low cytotoxicity (55).

1.4.3 Combination of lipid and polycations

Huang and co-workers proposed the combination of liposomes with cationic peptides such as PLL to form a ternary complex of liposome/peptide/DNA (LPD) (56-57). This approach of combining lipids and polycations has recently resulted in some works that exploits this enhancement of liposome-based delivery when a polycation is added to the formulation (33,56-59). The amplification in transfection (compared to the pure liposome vector) resulting from the combination of peptide with the cationic lipid may be caused by further DNA condensation and excessive positive charges provided by the addition of polycations (33,56,58-59). This view is supported by the increased surface charge of transfection vectors reported for the cases when either α -PLL (58) or HIV-1 Tat protein transduction domain peptide (59) were added to the lipid/DNA composition. One more argument in favor of a combined use of lipids and cationic peptides is related to the possibility to increase the versatility of the combined vectors. For example, HIV-1 Tat protein transduction domain peptide (59) and oligomers of the arginine-rich motif of HIV-1 Tat protein (60) are believed to assist gene transfer through the protein transduction domain and nuclear localization sequence, respectively. Additionally, including histidine residues could buffer endosomes so as to protect DNA from digestion in lysosome (18,33,52).

1.5 Studies of supramolecular structure in transfection

1.5.1 Supramolecular structure of transfection complex

Rädler et al observed that lipids DOPC/DOTAP condensed DNA into the lamellar phase by synchrotron small-angle X-ray scattering (SAXS) (61). Its internal organization was probed by measuring the repeat spacings of DNA and lipids quantitatively (61). Inside the complexes, the periodic distance of the multilamellar structure suggested a monolayer of hydrated DNA intercalated between lipid bilayers (61). Within the DNA layer, DNA chains orderly arranged in parallel gave rise to the DNA-DNA correlation peak in SAXS spectra (61). It corresponds to the DNA interaxial distance (d_{DNA}), showing quantitatively the extent of DNA condensation in the multilamellar stacks. In the self-assemble process, the confined DNA in between the lipids are caused by the electrostatic interaction (62). The driving force for the complex formation is the counterion release, including the counterions of DNA and those bound to the lipid membranes (61).

It was shown that the phase formation was dependent on the composition of lipids and charge ratio of lipids to DNA (CR) (43,61-63). The complex formulation-dependent structure variation provides an insight into the interfacial interactions. It was found that the DNA interaxial distance in the DNA/DOTAP/DOPC complexes increased with the cationic lipids dilution (the increasing fraction of neutral lipids DOPC) at isoelectric point (CR=1) (44,61). This result suggests that the positive charges of the cationic lipids have a propensity for completely neutralizing the negative charges of DNA so as to maximize the counterion release from both DNA and lipids (44).

Besides, DNA rich complexes (CR < 1) were found to have the higher DNA packing density than those at isoelectric conditions (CR=1) while DNA poor complexes (CR >1) have a lower DNA density (larger d_{DNA}) (63). It seems that the lipoplex absorbs the excess DNA or lipids by adjusting d_{DNA} inside the lamellar structure (63). For CR <1, d_{DNA} is reduced to accommodate more DNA in comparison with the isoelectric complex while it increases to bind more lipids for CR >1 (63). The entry of excess DNA or lipids is driven by the

release of their counterions but the intake is limited by the electrostatic repulsion. The minimum and maximum of d_{DNA} is due to the electrostatic repulsion between DNA chains and lipid membranes.

1.5.2 The influence of the initial supramolecular structure of lipoplexes on transfection

It is recognized that the morphologies of transfection complexes at supramolecular level greatly influence the interactions with cell membranes in gene delivery process (45,64). Koltover et al observed the rapid fusion of anionic vesicles with DOPE/DOTAP/DNA complexes that exhibited an inverted hexagonal phase (43). In contrast, the replacement of DOPE by DOPC resulted in a lamellar structure being relatively stable in the same experiment (43). Similar behaviors of the lipoplexes were found when those complexes contacted with the plasma membrane in mouse L-cell transfection (45). According to these results, the cellular uptake of lipoplexes showing a lamellar structure was proposed to occur via the endocytic pathway (45). The structure-transfection correlation implies that transfection behaviors can be modulated by controlling the supramolecular structure of complexes.

1.5.3 Structural evolution of complex in the delivery routes

In the process of *in vitro* gene transfer, the interaction between transfection complexes and cellular components, such as plasma membranes and endosomal membrane, and the exposure to physiological salt conditions determine the transfection efficiency (3). Some studies reported the phase transition resulting from the interaction and correlated it with the transfection behaviors (35,65). Tarahovsky et al monitored DNA release from lipoplexes upon the mixing with anioinic lipids and studied the phase organization of the mesomorphic lipids mixtures (35). They found that DNA-releasing ability was related to the phase preference (35). Koynova et al rationalized the transfection data of two cationic phospholipid derivatives by the phase transition occurring when the cationic

lipids were mixed with biomembrane lipids (65). Fifty-times discrepancy in transfection efficiency was found for two lipoplexes with a similar multilamellar phase, but the superior phospholipid displayed a more extensive membrane fusion and a tendency to form non-lamellar phase when it was interacting with biomembrane lipids (65).

The structural evolution of lipoplexes upon the interaction with cellular membranes in living cells was observed at the nanometric scale by Bihan et al using electron microscopy (34). This information contributes to the understanding of lipofection mechanism, especially endosomal escape (34). The influence of physiological salt conditions was suggested by monitoring the structure variation of DOPC/DOTAP/DNA complex as a function of NaCl concentration (63). It was found that the internal cohesion of the complex was weakened with the increasing ionic strength, suggesting a tendency of lipoplexes to dissociate inside cells (63). For *in vivo* transfection, serum components can bind to the transfection complexes and possibly inhibit the gene transfer (39). Marchini et al compared the SAXS patterns of the lipoplexes in the presence and absence of serum and found that the lamellar phase was swelled while the DNA packing density was unaffected upon the addition of serum (66). It was suggested that the serum components mainly interacted with the lipid membranes rather than DNA, which was supported by the DNA protection data (66). According to the quantitative analysis of the Bragg peak intensities, they indicated that a lamellar-to-hexagonal phase transition could be induced by serum for the formulation that exhibited the coexistence of lamellar and hexagonal phases (66).

1.6 Experimental design and motivation

In a previous study of our group (67), the design and characterization of gene transfer vectors based on ϵ -oligolysines (Fig. 1) was motivated by their favorable physical and biological properties (soluble, biodegradable and nontoxic) compared to the frequently used gene delivery peptides such as α -PLL (67-68). Those results showed that ϵ -oligolysines exhibited higher

transfection ability as well as lower cytotoxicity and induced smaller DNA condensates than α -lysines (67), supporting the idea that such ϵ -lysines are potentially promising building blocks in the design of gene delivery vehicles. The ϵ -lysines with a branched design containing pendent groups of short α -oligopeptides [ϵ -(R)K10, ϵ -(Y)K10, ϵ -(L)K10, ϵ -(YR)K10, and ϵ -(LYR)K10] displayed the improved transfection ability, especially peptide ϵ -(LYR)K10 (67). Those data give confidence for the rationale behind this design and motivate further optimization.

In the present work, some predictions based on our previous results and literature data were exploited to develop new ϵ -oligolysine-based peptides, ϵ -(LYRH)K10, ϵ -(LYH)K10, ϵ -(LYK)K10, ϵ -(LKY)K10 and ϵ -(YKL)K10 (Fig. 1). ϵ -oligolysine backbone was synthesized with degree of polymerization 10 and α -amino acid triplets (amino acids in the brackets) were attached to each of the α -amino group of ϵ -oligolysine. Since histidine residue was reported to enhance endosomal escape through the “proton sponge” effect (18,33,52), the novel histidine-containing peptides ϵ -(LYH)K10 and ϵ -(LYRH)K10 are expected to facilitate gene transfer.

The side chain LYK is chosen for the reason that the residues Arg and Lys have many similar properties. The study of peptides ϵ -(LKY)K10 and ϵ -(YKL)K10 parallel to the peptide ϵ -(LYK)K10 aims to investigate the influence of the sequential arrangement of residues of the side chain. Since it was reported that combined effect of lipids and polycations can greatly enhance transfection efficiency (33,52,56,59-60,69), the novel ϵ -peptides were used in the combination of cationic liposome DOTAP (N-[1-(2,3-Dioleoyloxy)propyl]-N,N,N-trimethylammonium methylsulfate), resulting in a ternary complex liposome/ ϵ -peptides/DNA (LPD). The choice of DOTAP in our study is due to the fact that the characteristics and supramolecular properties of this transfection agent is well studied (44). Also unlike other commercial transfection formulations, the chemical composition of DOTAP is well defined and known.

The potential usage of ϵ -peptides and liposome/ ϵ -peptides in gene delivery can be estimated by measuring the *in vitro* transfection efficiency and cytotoxicity. Complex DOTAP/DNA (LD) is used as a positive control because DOTAP is a widely-used commercial transfection agent. The *in vitro* transfection efficiency of complexes ϵ -peptides/DNA and liposome/ ϵ -peptides/DNA were evaluated in four cell lines (HeLa, HEK-293, A549 and Mewo). HeLa and HEK-293 cells are commonly used in transfection studies. A549 and Mewo cells have a significant difference in cell surface receptors and they are the negative and positive control for RGD (arginine-glycine-aspartic acid)-mediated transfection, respectively (70). Since the same DOTAP/DNA stoichiometry were used for both complexes DOTAP/ ϵ -peptides/DNA and DOTAP/DNA, the effect of peptides on the DOTAP-mediated transfection emerged by simply comparing the LPD data with control results. MTT assay was performed to examine the cytotoxicity of individual peptides and binary peptide/DOTAP mixtures at the doses similar to or higher than that applied in the transfection study.

After scanning gene delivery properties of all the peptides, various formulations were tested to optimize their efficiency for the most effective peptides. Since we focused on the potentiating effect of ϵ -peptides on lipofection, the DOTAP/DNA stoichiometry was fixed for LPD complexes and the formulations differed in the charge ratio of ϵ -peptide to DNA. It was reported that the coverage of DNA by lipids in lipoplexes is incomplete even when the lipids is in excess (71). To know whether ϵ -peptides can coat the exposed DNA, zeta potential of transfection particles were measured as an indicative of surface charge. Contradictory results were reported for the variations of particle size upon the addition of polycations to the DNA/lipid recipes, which may be attributed to the limited formulations used for displaying the variation tendency (33,56,59). To address this issue, particle sizes of the LPD complex with a variety of formulations were quantified. Besides, pH dependence of DNA condensation by histidine containing ϵ -peptides was investigated by light scattering because the incorporation of histidine residues into peptides is based on its pH buffering effect at endosomal pH (18,24,31,33,52-53).

It was proposed that DNA condensation can be improved by the peptides in LPD complex as compared to the lipoplex (33,56). Previous studies of the supramolecular structure of lipoplexes by synchrotron SAXS showed that DNA and lipids were orderly organized in the complex and the phase of complex influenced the gene delivery process (43,45,61-62). Here, a similar SAXS scanning was conducted for the ternary LPD complexes in transfection-relevant formulation. It was expected to show the phase organization, especially the extent of DNA condensation inside the complex. By tailoring the complex formulations, it is possible to identify the factors governing the structure variation and the roles of DOTAP and peptides in complex formation.

Significant attention has been paid to the relationship between the biophysical and structural parameters and effectiveness of transfection in order to explain the reported transfection results, and more importantly, to collect advantageous information or find some clues for the design of new vectors (7). Since LPD is a newly emerged transfection system, its properties were previously little studied. Therefore, the transfection results are correlated with biophysical properties and supramolecular structures. This correlation would be not only significant for understanding the LPD transfection system, but also valuable for the general gene delivery study.

1.7 Biophysical methods

1.7.1 Dynamic light scattering (DLS)

Particle size measurement

The technique is used to determine the sizes of small particles in Brownian motion in solution, known as photon correlation spectroscopy (PCS) or Quasi Elastic Light Scattering (QELS). In light scattering theory, light can be treated as an electro-magnetic wave. The scattered light comes from the oscillating changes of the electrons in particle induced by the oscillating electro-magnetic

field. Light scattered by particles results in the time dependence of intensity fluctuation due to the Brownian motion of the particles in solution. So by observing fluctuation of the scattered light, one can obtain information about the motion of the particles.

In QELS, each measurement is divided into small time intervals and the intensity in each of these intervals is represented by the number of detected photons of scattered light. The intensity autocorrelation function is crucial for measurement, formed by averaging the products of the intensities in the small time intervals as a function of the time between intervals. The autocorrelation function is related to the diffusion properties of particles.

As Fig. 7 shows, there are two limits in the correlation: it is high for short times and lost as time decays. The function decays exponentially with time for monodisperse suspension of rigid and globule particles. According to equation:

$$C(\tau) = \langle I(t) \cdot I(t + \tau) \rangle = A e^{-\Gamma \tau} + B \quad (1)$$

where τ is the time delay, A and B are an optical constant determined by the instrument design, and Γ is related to the relaxation of the fluctuations by

$$\Gamma = Dq^2 \quad [\text{rad/sec}] \quad (2)$$

The value of q is calculated from

$$q = (2\pi n / \lambda_0) \sin(\theta/2) \quad (3)$$

θ is the scattering angle ($= 173^\circ$ in our experiment as illustrated in Fig. 8), λ_0 is the wavelength of the laser light, and n is the index of refraction of the suspending liquid.

D is the coefficient of diffusion and it is the principle quantity measured by DLS. For a sphere, following equation assumes that the particles are moving independently of one another.

$$D = (k_B T) / [3\pi\eta d] \quad (4)$$

Where k_B is Boltzmann's constant, T is the temperature in K, η (in centi poise) is the viscosity of the liquid in which the particle is moving, and d is the particle diameter.

The determination of particle size d can be done by equation (4) and value of D , which is calculated from equation (2), where Γ is given by fitting the measured function to equation (1).

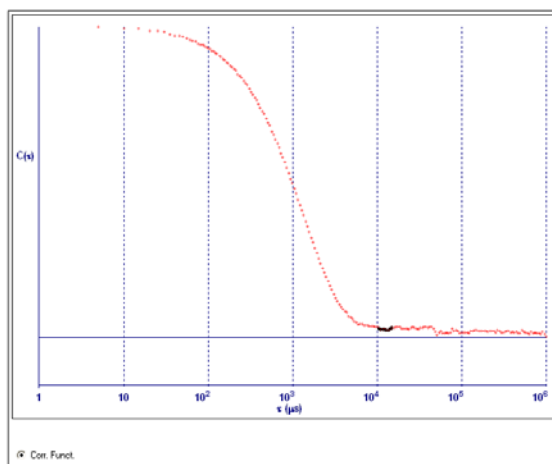


Figure 7. An example of the correlation function $C(\tau)$ plotted against the time delay.

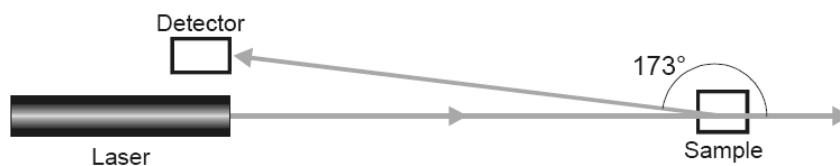


Figure 8. Illustration of the set-up of a DLS experiment.

Figure adapted

from [http://www.biophysics.bioc.cam.ac.uk/files/Zetasizer Nano user manual Man0317-1.1.pdf](http://www.biophysics.bioc.cam.ac.uk/files/Zetasizer%20Nano%20user%20manual%20Man0317-1.1.pdf)

Zeta potential measurement

Figure 9 characterizes the distribution of ions surrounding dispersed particles. Ions are absorbed directly onto the particle surface, forming the inner layer of the electrical double layer, called Stern layer. Within the outer layer (diffuse layer), ions are less strongly bound but they are attached to and move with moving particles within a boundary, named slipping plane (Fig. 9). Zeta potential is the potential difference between the bulk liquid and slipping plane at the surface of dispersed particle.

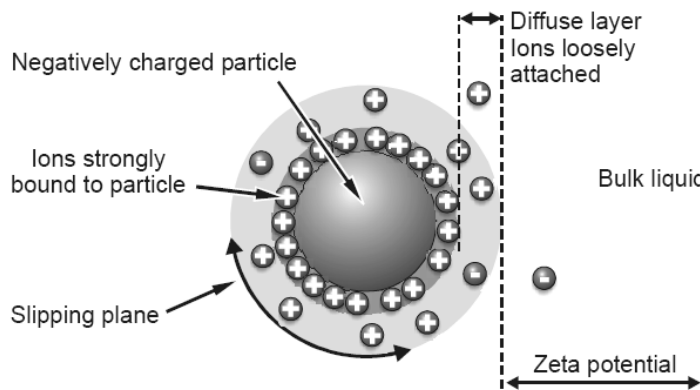


Figure 9. The distribution of ions in the surrounding interfacial region between the suspension particle and bulk liquid.

Figure adapted

from http://www.biophysics.bioc.cam.ac.uk/files/Zetasizer_Nano_user_manual_Man0317-1.1.pdf

Zeta potential is calculated from the experimentally determined electrophoretic mobility, i.e. the constant moving velocity of a particle in an applied electrical field. It is related to the rate of fluctuation of scattered light by moving particles, which enables it measurable by laser Doppler velocimetry (LDV).

The measured velocity depends on the strength of electric field, zeta potential, the dielectric constant and viscosity of the medium, which is expressed as Henry equation:

$$U_E = 2\epsilon z f(ka) / 3\eta,$$

where z is zeta potential; U_E is electrophoretic mobility; ϵ is dielectric constant; η is viscosity; $f(Ka)$ is 1.5 in aqueous media and moderate electrolyte concentration according to the Smoluchowski approximation.

1.7.2 Static light scattering (SLS)

Unlike the time-dependent intensity given by DLS, the time-averaged intensity of scattered light is measured by static light scattering (SLS) based on the principle that the larger particles generate more scattered light than the smaller ones. The scattered intensity as a function of the detector angle depends on the particle size. In this case, SLS is useful to monitor the course of the DNA condensate formation. In our light scattering experiments, the scattered light was detected at a 90 degree angle to the incident beam, of which intensity values were collected during typical 2 min record (Fig. 10). The intensity of SLS signal is defined by two major factors: particle size and difference in refraction indices between solvent and particles. Refraction index of the condensed particle is dependent on the composition of the particle and for the cases when a particle contains significant amount of solvent, the signal intensity might be lower from big swollen particle than from the small dense one.

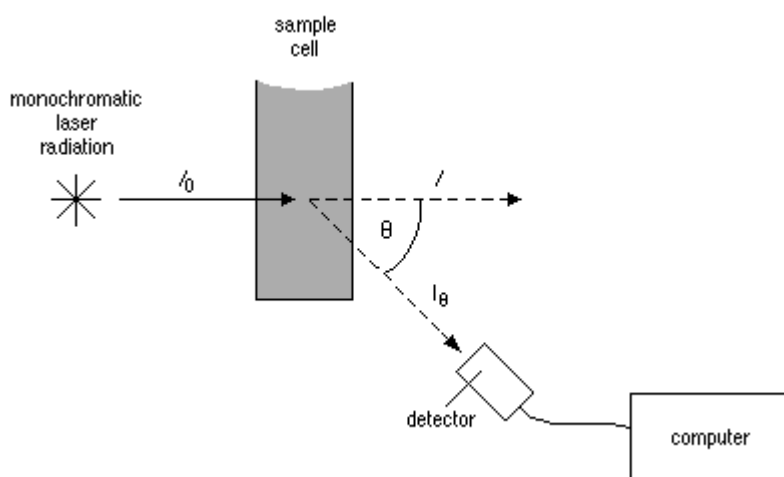


Figure 10. A schematic drawing of static light scattering.

Detector records the time-averaged scattered light intensity, $I(\theta)$. In our experiment, $\theta = 90^\circ$. I_0 represents the incident intensity. Figure adapted from <http://www.currentprotocols.com/protocol/ps0708>

1.7.3 Flow cytometry

Flow cytometry, based on the principles of light scattering, light excitation, and emission of fluorochrome molecules, simultaneously measures and analyzes multiple physical characteristics of particles when they flow in a liquid stream through a beam of light. It is a combined system including a fluidics system to introduce and focus the cells suspended in the solution, optics system to generate and collect the light signals, and electronics system to convert the optical signals to proportionate electronic signals and digitize them for further analysis on the computer.

The sample is carried and accelerated to the flow of sheath within a flow chamber. Sample core, the portion of the fluid stream where cells are located, is focused in the center of the sheath fluid where the laser beam will interact with them and irradiate one at a time. Two types of parameters are measured when individual cell of interest pass through the laser intercept: light scattering and fluorescence. Figure 11 illustrates the fluidics system in flow cytometry and detection of light scattering and fluorescence signal. The light scattering is related to the size, internal complexity, and granularity of the cell. Forward-scattered light (FSC) is proportional to cell-surface area or size and side-scattered light (SSC) is proportional to cell granularity or internal complexity. An electron in fluorochrome is excited to a higher energy state and quickly decays to its ground state, releasing energy as a photon of light. The fluorescent signal (FL) detected is proportional to the number of fluorochrome molecules on the cell, reflecting its relative fluorescence intensity.

The scattered and emitted light signals from cells are collected by lenses, sent to different detectors by a combination of beam splitters and optical filters, and converted to electronic signals (voltages) proportional to the optical signal by photomultiplier (PMT) or photodiodes. The voltage pulse is processed by a series of linear and log amplifiers and assigned a digital value by the Analog to Digital Converter. An example of FACS Dotplot results is shown in Fig. 12, where each dot in the graph represents the single particle analyzed.

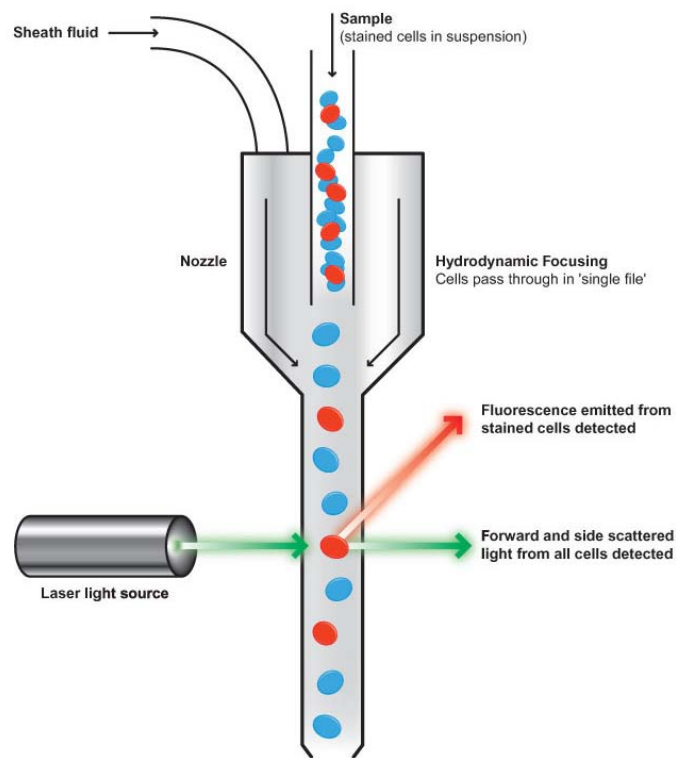


Figure 11. An illustration of fluidics system in flow cytometry and detection of light scattering and fluorescence signal.

Figure adapted from <http://www.abcam.com/index.html?pageconfig=resource&rid=11446>

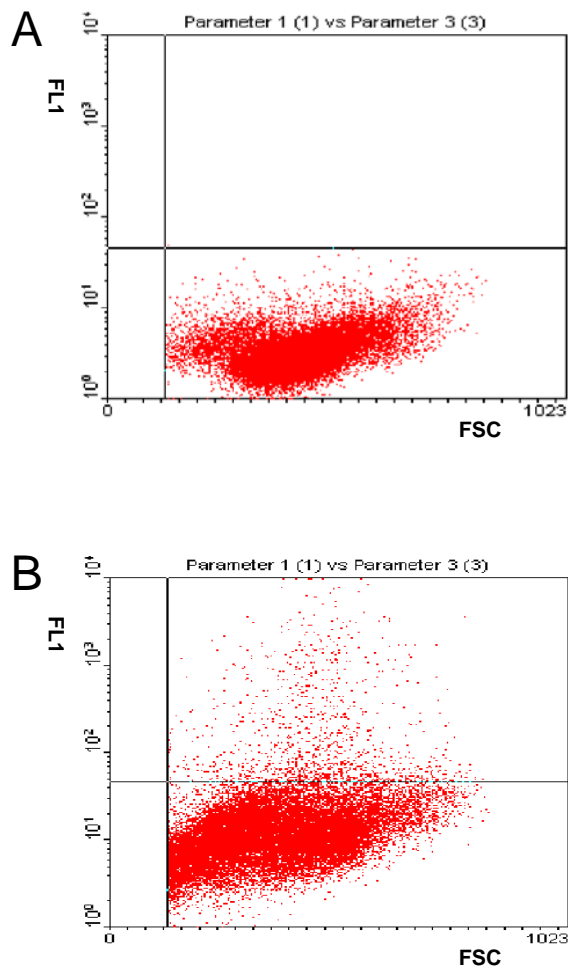


Figure 12 An example of FACS Dotplot.

Fluorescent signals (FL) were measured through channel 1, called FL1. A total of 3×10^4 cells from a sample were analyzed in each measurement. Parameter of X axis is FSC and of Y axis is FL1. Fig. 3A shows negative control, whereas Fig. 3B shows A549 cells transfected with the complex of plasmid DNA and peptide ϵ -(LYH)K10.. Data were analyzed with WinMIDI (version 2.5) software, where events were filtered by correlated measurements of FSC and SSC (cell debris and cell agglomerates were discarded by gating). Quadrant is drawn to separate positive events from negative events according to the negative control data. The events, which are at the upper right region, represent transfected cells.

1.7.4 Small-angle X-ray scattering (SAXS)

Small-angle X-ray scattering (SAXS) is used to study the ordered structure of various objects in the nanometer scale by analyzing the X-ray scattering at an angle less than 5° . Since the scattering intensities of biological samples are always weak, the high intensity of synchrotron radiated X-ray is often used as a

beam source for biological samples. The high energy of X-ray (> 12 eV) is capable of penetrating into the samples and producing the spectrum with a good resolution.

In the typical SAXS experiment, focused X-ray beam is directed to the sample and the 2-D scattering pattern is recorded by a highly collimated detector. For ordered structures, the scattering pattern follows Bragg's law:

$$n\lambda = 2d\sin\alpha,$$

where n is an integer, λ is the wavelength and d is the distance between scattering centers and α is the angle between incident beam and scattering plane.

The distance between the sample and detector determines the scattering angles and subsequently intercepts the range of scattering wave vector q , which is defined as:

$$q = 4\pi\sin(\theta)/\lambda,$$

where 2θ is the scattering angle and λ is the x-ray wavelength. The detector behind the sample records scattering signals while non-scattered beam that pass directly through the sample is blocked by the beamstop. Fig. 13 shows the schematic drawing of SAXS instrument in national synchrotron radiation research center of Taiwan (72). The SAXS spectrum can be extracted from the 2-D scattering pattern by converting it to one-dimensional spectrum $I(q)$ profiles, which is the intensity as a function of the magnitude of the scattering vector q .

Position and periodicity of Bragg peaks present the phase, e.g. the lamellar phase produces peaks with periodicity of 1:2:3:4 and the hexagonal phase gives rise to peaks with q values in relation: $1:\sqrt{3}:\sqrt{4}:\sqrt{7}:\sqrt{9}$ (44). The periodic distance d was calculated from the q value of the corresponding peak using the relation $d = 2\pi/q$. For a lamellar lattice, the interlayer spacing (d) can be calculated from the equation:

$$d = 2\pi / q;$$

for the unit spacing (a) of a hexagonal phase, it is calculated according to the equation:

$$a = (2/\sqrt{3})2\pi / q,$$

where the q is the first order of peaks.

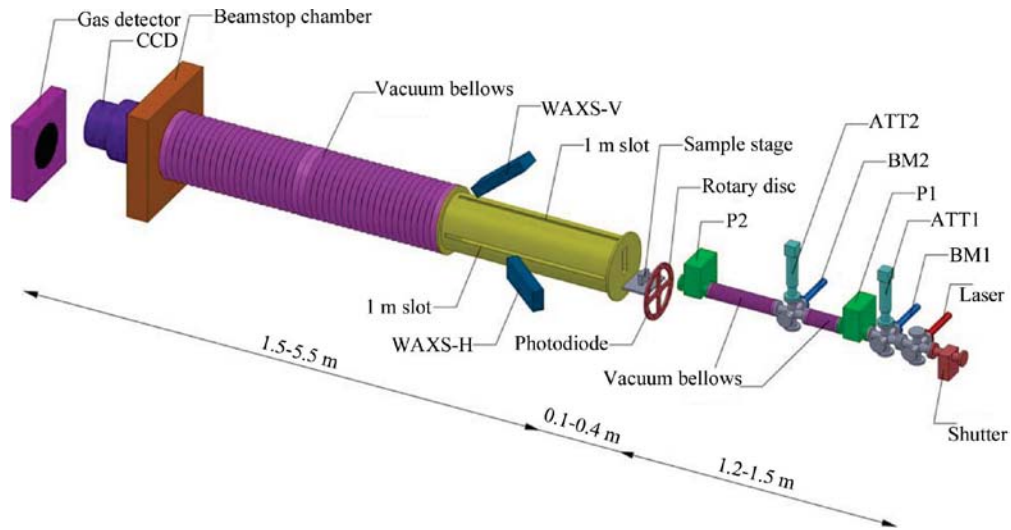


Figure 13. A schematic drawing of the BL23A SAXS/WAXS instrument in national synchrotron radiation research center of Taiwan.

Starting from the right-hand side we show the collimation stage with the beam shutter, the laser alignment system, the two beam-intensity monitors, the two sets of attenuators, the pinhole-slit systems, and the rotary disc containing a photodiode detector and nine standard metal foils for beam-energy calibration. Figure adapted from reference (72).

2. Materials and methods

2.1 Materials

DNA. The plasmid pEGFP-N1 (4.7 kbp), which encodes the green fluorescent protein, GFP, was used. The plasmid was amplified in the *E. coli* DH5 α strain and isolated using the QIAGEN (Valencia, CA, USA) HiSpeed Plasmid Purification Maxi Kit or extracted by alkaline lysis method.

Peptides. α -substituted ϵ -peptides ϵ -(LYK)K10, ϵ -(LKY)K10, ϵ -(YKL)K10, ϵ -(LYH)K10, ϵ -(LYRH)K10 and ϵ -(LYR)K10 (chemical structure is shown in Fig. 1) were synthesized using solid-phase peptide synthesis as described in detail in a previous study (67). The peptide stock solutions (5 mg/ml; or 25 mg/ml for SAXS sample preparation) were prepared in sterile, double-distilled water.

Cell culture. HeLa human cervical carcinoma cells (CCL-2), 293F human embryonic kidney cells (PEAKrapid, CRL-2828), Mewo human melanoma cells (HTB-65) and A549 human lung carcinoma (CCL-185) were purchased from ATCC (Manassas, VA, USA). Cells were grown in Dulbecco's modified Eagle's medium (DMEM; Gibco, Eggenstein, Germany) supplemented with 10% fetal bovine serum (FBS; Hyclone) at 37 °C in a humidified 5% CO₂ atmosphere. The cells were fed every 2-3 days and split when almost confluent employing trypsin/EDTA (Gibco).

Liposome. Transfection agent DOTAP solution was purchased from Roche (Basel, Switzerland). It was used in gene delivery studies directly. DOTAP lipids used in SAXS samples were purchased from Avanti Polar Lipids, Inc. (Alabaster, AL, USA). DOTAP suspension in chloroform was dried under vacuum at room temperature for 1 hour and dissolved in deionized water to concentration 25 mg/ml. Resuspended DOTAP was either extruded by LiposoFast-Basic with 100 nm polycarbonate membrane (Avestin, Inc., Canada)

or sonicated with 1 s pulse of 30% amplitude for 10-15 min to clarity by tip sonicator Sonics vibra cell™ (Sonics & materials Inc., USA). The freshly prepared DOTAP (hydrodynamic diameter of ~ 100 nm and polydispersity of ~ 0.1 according to DLS measurement) was stored at room temperature.

Chemical reagents. DMSO (dimethyl sulfoxide), MTT (3-(4,5-dimethylthiazol-2-yl)-2,5-diphenyl tetrazolium bromide) were purchased from Sigma-Aldrich (St. Louis, MO, USA). All other chemicals for buffers were purchased from Fisher Scientific (Pittsburgh, PA, USA).

2.2 Gene delivery studies

2.2.1 *In vitro* transfection

3×10^5 cells per dish were seeded in 60-mm tissue culture dishes (TPP, Trasadingen, Switzerland) and grown in 5 ml DMEM supplemented with 10% FBS, sodium pyruvate (100 mM), and L-glutamine (200 mM). When the cells were at 80% confluency, the culture medium was replaced with serum-free medium and cells were transfected with the complexes carrying the plasmid pEGFP-N1. The preparation of complexes was as following:

DOTAP, the commercial transfection agent, was used with concentration of 1 mg/ml aqueous dispersion (liposomes) in MBS (MES-buffered saline). HBS solution (pH 7.05) was 25 mM Hepes buffer containing 70 mM NaCl, and 0.75 mM Na_2HPO_4 . 50 μl (5.6 μg) plasmid DNA solutions were prepared by diluting 1.4 mg/ml stock DNA solution by HBS buffer. For all four cell lines, the transfection was made under the optimal conditions suggested in our previous study (67); DOTAP/DNA complexes were prepared by adding 50 μl (5.6 μg) plasmid DNA solution to 30 μl DOTAP (1 mg/ml) in 70 μl HBS. Peptide/DNA complexes were prepared by adding 50 μl (5.6 μg) plasmid DNA solution to 60 μl peptide solution (5 mg/ml) in 40 μl HBS. DOTAP/peptide/DNA complexes were prepared by adding 50 μl (5.6 μg) plasmid DNA solution to a mixture of

30 μ l peptide solution (5 mg/ml) and 30 μ l DOTAP (1 mg/ml) in 40 μ l HBS. In transfection with charge ratio variation, the plasmid DNA solution was 50 μ l (5.6 μ g) and peptide was added according to the charge ratio of peptide to DNA. Ternary complexes DOTAP/peptide/DNA were prepared according to two protocols, where the charge ratio of DOTAP to DNA was constantly equal to 2. Complexes of peptide-DNA-DOTAP were prepared by adding DNA to the mixture of peptide and DOTAP while for systems denoted (peptide-DNA)+DOTAP, DNA was first condensed by peptides and then peptide/DNA complexes was added into DOTAP solution. Complexes were incubated at room temperature for 30 min prior to transfection.

After the cells were incubated with complexes for 5 h, the medium containing the complex was replaced with 5 ml of growth medium. After forty-eight hours post-transfection, the gene expression was measured using fluorescence activated cell sorting (FACS).

2.2.2 Flow cytometric analysis

Cells in each dish were harvested by trypsin digestion after a final 48 h incubation and subsequently re-suspended to a final volume of 1 ml in PBS buffer (137 mM NaCl, 2.7 mM KCl, 4.3 mM Na₂HPO₄ and 1.47 mM KH₂PO₄; pH 7.2) as a sample for analysis. The cell-associated fluorescence was studied by flow cytometry (FACSCalibur, BD Biosciences, San Jose, CA) using the green channel FL-1H. A total of 3×10^4 cells from a sample were counted for each measurement. Data were analyzed with the WinMIDI (version 2.5) software, where events were filtered by correlating measurements of FSC and SSC (cell debris and cell agglomerates were discarded by gating). The transfection efficiency was calculated as the ratio of the number of cells expressing GFP to the number of cells analyzed.

2.2.3 Cytotoxicity assay

HeLa cells were incubated (37 °C, 5% CO₂) at an initial density of 1×10^4 cells in 200 μ l growth media per well in 96 well plate. Sixteen hours later, the growth medium was replaced with 188 μ l DMEM and 12 μ l HBS containing DOTAP, peptides or mixtures of peptide and DOTAP at the same concentration as transfection under optimal conditions. In the concentration-dependent cytotoxicity study, a series of concentrations 0.006 to 0.18 mg/ml were used in peptide-mediated system. In mixtures of DOTAP and peptides, the concentration ratio of peptide to DOTAP was 5 and concentrations of 0.0006 to 0.018 mg/ml and 0.003 to 0.09 mg/ml was used for DOTAP and peptides. In the control well, 188 μ l DMEM and 12 μ l HBS was used. After 16 h incubation, DMEM and solution was discarded and cells were incubated with 100 μ l DMEM and 20 μ l PBS containing 5-mg/ml MTT for 4 h. Following that, the solution was discarded and when the crystals in each well were dissolved by DMSO, the optical density, which is directly correlated with cell quantity, was measured at 590 nm by microplate reader (Bio-Rad, Hercules, CA).

2.3 Biophysical methods

2.3.1 Static light scattering

Static light scattering (SLS) experiments were performed by a Brookhaven 90plus particle size analyzer (Long Island, NY). The excitation wavelength was 600 nm and the scattered light was detected at a 90-degree angle to the incident beam. DNA compaction was monitored by SLS during titration of DNA with cationic peptide [5 μ M plasmid DNA (charged groups) was titrated by 15 μ M ϵ -(YKL)K10 or 25 μ M ϵ -(LYH)K10 in appropriate buffer]. The titration was done in the 1.5 ml cuvettes, where the solution containing compaction agents was gradually added into DNA solution. We recorded the scattering intensities of the titration points, which corresponded to the concentrations of compaction agent. Buffers provided the pH conditions were as following: Citrate buffer (70 mM NaCl, 10 mM citrate) was used for pH 5-6.5; phosphate buffer (10 mM

NaH₂PO₄, 70 mM NaCl) was used for pH 6.5-7.5; HBS buffer (25 mM Hepes, 70 mM NaCl, and 0.75 mM Na₂HPO₄) was used for pH 6.5-8.0. All buffers were filtered through 0.2 µm filters.

The scattering intensity was plotted against the concentration of compaction agent, resulting in a titration curve. EC₅₀ values (the concentration of peptide at the midpoint of the titration curve) were calculated from experimental data, using a sigmoidal fitting with the software Origin 7.0 (OriginLab Corp., Northampton, MA). Fig. 14 shows an example of titration curve and EC₅₀ value, where the black points represent the titration points and red curve is the sigmoidal fitting curve.

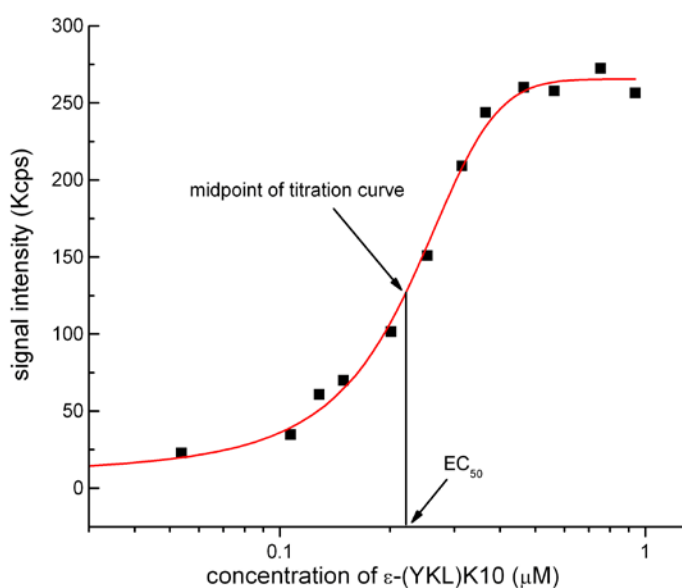


Figure 14. An example of plotting of the intensity of scattered light against the concentration of peptide.

Points are measured data and the curve displays sigmoidal fitting of the experimental results. EC₅₀ value is the concentration of peptide at the midpoint of the titration curve.

2.3.2 Dynamic light scattering

DOTAP/DNA, ε-peptides/DNA and DOTAP/ε-peptides/DNA complexes were prepared in a volume of 1 ml, where DNA is 1.12 µg/ml. The complex formulation was defined as the charge ratio of DOTAP to DNA (L/D), peptide to DNA (P/D). The charge ratio of positive to negative (CR_{+/-}) is the sum of L/D

and P/D for ternary LPD complexes. For DOTAP/DNA complex, L/D from 1 to 7 were used; for ϵ -peptides/DNA complexes, P/D from 1 to 36 were used. Ternary complexes DOTAP/peptide/DNA were prepared according to two protocols, where the L/D was constantly equal to 2 and P/D from 1 to 20 were used. Complexes of peptide-DNA-DOTAP were prepared by adding DNA to the mixture of peptide and DOTAP while for systems denoted (peptide-DNA)+DOTAP, DNA was first condensed by peptides and then peptide/DNA complexes were added into DOTAP solution. Complexes were incubated at room temperature for 30 min prior to DLS measurement.

Particle size and zeta potential were measured at 25 °C using a Malvern Zetasizer Nano (Malvern Instruments, U.K.) with a laser source operating at a wavelength of 633 nm. For particle size measurement, light scattered by the sample was detected at an angle of 173° and the size distribution profile was determined by applying standard theory using software provided by equipment manufacturer. As Fig. 15 shows, the average diameter of particles suspended in the sample was calculated from the distribution, which was the result of particle size measurement. For zeta potential measurement, light scattered by the sample was detected at an angle of 17° and zeta potential values were calculated from measured velocities using Smoluchowski model.

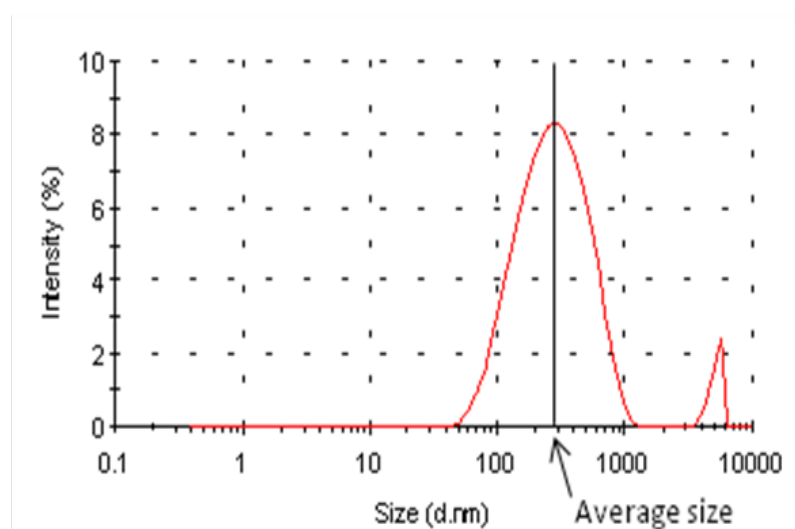


Figure 15. An example of the size distribution graph.

It is the size measurement of DOTAP/DNA complex at L/D =2 in HBS buffer.

2.3.3 Small-angle X-ray scattering

DOTAP/DNA complex was formed by mixing 100 µg plasmid DNA in 75 µl HBS with a proper amount DOTAP lipids in 75 µl HBS according to the charge ratio lipids to DNA (L/D). DOTAP/peptide/DNA complex was formed by adding 100 µg plasmid DNA in 75 µl HBS into the mixture of DOTAP and peptides in 75 µl HBS, where the amount of DOTAP and peptide are determined by the charge ratio lipid to DNA (L/D) and charge ratio peptide to DNA (P/D). Since both peptides and lipids carry positive charges, the charge ratio of positive to negative ($CR_{+/-}$) is defined as the sum of L/D and P/D. The complexes were sealed in 2 mm quartz capillaries (Charles Supper Company, USA) and centrifuged to force precipitates to pellet in the bottom of capillaries.

SAXS experiments were performed with 14.0 keV ($\lambda = 0.886 \text{ \AA}$), at the Beamline 23A SWAXS endstation at the National Synchrotron Radiation Research Center (Hsinchu, Taiwan) (72). Data were recorded by a charge-coupled device-based area detector (MarCCD165, Mar Evanston, IL, USA) at 1.75 m sample-to-detector distance. The scattering wave vector $q = 4\pi\lambda^{-1}\sin\theta$ (with 2θ the scattering angle) was calibrated using silver behenate. SAXS profiles were circularly averaged from the isotropic 2-D patterns measured. All the SAXS data were corrected for background scattering and sample transmission. The ordered distance d was calculated from the q value of the corresponding peak using the relation $d = 2\pi/q$.

3. Results

3.1 *Studies of gene delivery properties*

3.1.1 Influence of sequence of the α -substituted side chain

The transfection abilities of the six peptides ϵ -(LYK)K10, ϵ -(LKY)K10, ϵ -(YKL)K10, ϵ -(LYH)K10, ϵ -(LYR)K10 and ϵ -(LYRH)K10 and their mixtures with DOTAP were examined for the four cell lines: HeLa, HEK 293, Mewo and A549. The transfection experiments were performed using the optimal peptide/DNA and DOTAP/peptides/DNA stoichiometry determined in a previous study (67). The results are summarized in Fig. 16.

In complexes of peptide and DNA, no transfection is detected for the peptides ϵ -(LYK)K10 or ϵ -(LKY)K10 in any of the four cell lines. ϵ -(YKL)K10 is capable of delivering plasmid DNA to the nuclei of the HEK 293, A549 and Mewo cells but the efficiencies are rather low ($< 1.6\%$). Much higher transfection efficiencies are obtained for ϵ -(LYH)K10, ϵ -(LYR)K10 and ϵ -(LYRH)K10. In particular, the transfection efficiency of ϵ -(LYH)K10 or ϵ -(LYR)K10 is similar to DOTAP in A549 and Mewo cells and ϵ -(LYH)K10 or ϵ -(LYRH)K10 is more effective than DOTAP in HEK 293 cells.

For the ternary complexes of DOTAP/peptide/DNA (LPD), addition of DOTAP results in increased transfection for all cell lines and some peptides do actually produce an additive effect whereby the transfection of the LPD recipe exceeds that of the positive control (DOTAP/DNA mixture applied according to the transfection protocol of the DOTAP manufacturer). In the cases of LPD complexes including the peptide ϵ -(LYK)K10, ϵ -(LKY)K10 or ϵ -(YKL)K10, different cell lines show different levels of transfection. In HeLa cells, the addition of peptide reduces transfection. In HEK 293 cells the addition of peptide makes little difference in transfection relative to positive control, while

for both A549 and Mewo cell lines, combination of ϵ -(LKY)K10 or ϵ -(YKL)K10 with DOTAP significantly improves transfection (ϵ -(LYK)K10 showing neither positive nor negative effect relative to the control).

Variations of transfection efficiencies between cell lines are probably due to the difference in cell surface receptors (70). In all four cell lines, the highest GFP expression levels are always provided by mixtures of DOTAP and the arginine or histidine containing peptides, ϵ -(LYH)K10, ϵ -(LYR)K10, ϵ -(LYRH)K10 (with an exception of HeLa cells and ϵ -(LYH)K10). Up to 1.9, 4.4, 6.5 and 3.1 fold increased transfection is observed in HEK 293, A549, Mewo and HeLa cells, respectively. That data confirms the improved transfection ability of the mixture peptide/DOTAP over DOTAP. In HeLa cells, only ϵ -(LYR)K10 or ϵ -(LYRH)K10 improves transfection and the effect of combination of DOTAP with either of these two peptides is significant.

Those results unravel the effect of sequence of the α -substituted side chain on transfection abilities of ϵ -oligolysine based peptides. In peptide-mediated systems, arginine or histidine containing branches are more effective than lysine-containing, which is also observed in the combination of DOTAP. Results of ϵ -(LYK)K10, ϵ -(LKY)K10 and ϵ -(YKL)K10 show the influence of sequential arrangement of residues of α -substituted side chain on transfection activities.

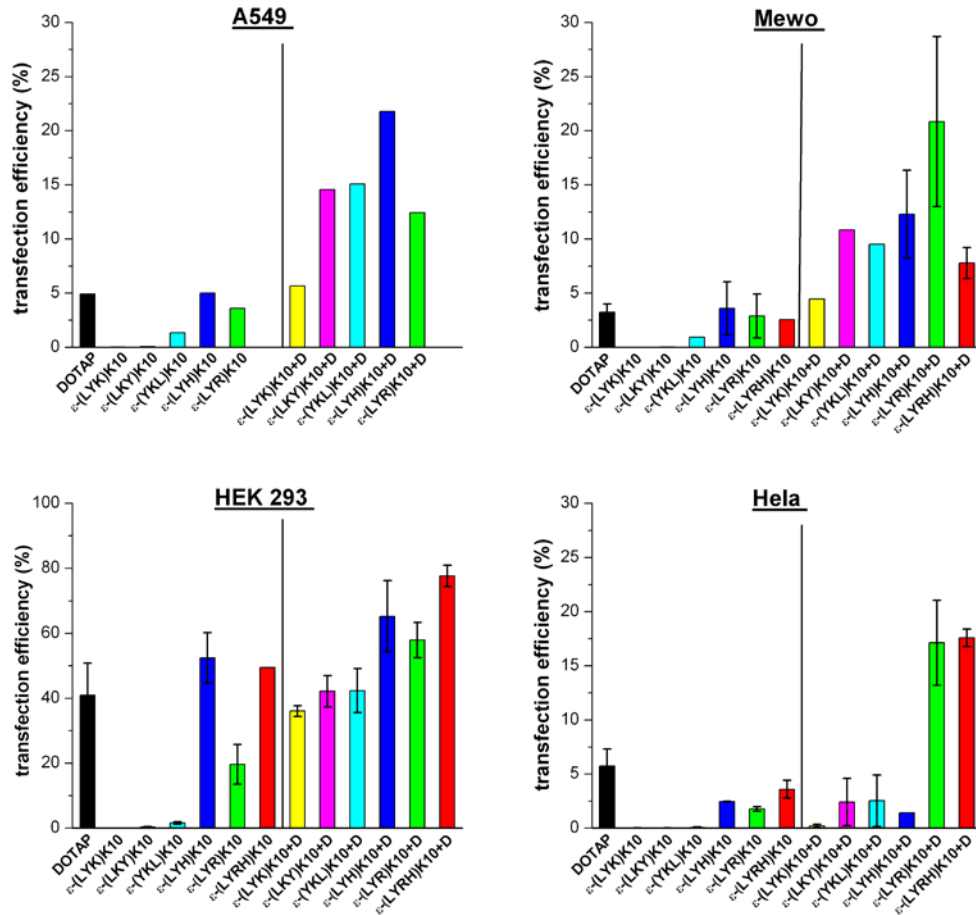


Figure 16. Transfection efficiencies of DOTAP, ϵ -(LYK)K10, ϵ -(LKY)K10, ϵ -(YKL)K10, ϵ -(LYH)K10, ϵ -(LYR)K10, ϵ -(LYRH)K10 and mixtures DOTAP-peptide determined for four cell lines, A549, Mewo, HEK293 and HeLa (indicated in the graphs).

Transfection efficiency (mean value of 3-5 measurements with standard deviation) was measured as the ratio of the number of cells expressing GFP to the number of cells analyzed by flow cytometry. The black vertical bar separates data for peptides and mixtures of peptide + DOTAP.

3.1.2 Evaluation of cytotoxicity of 6 peptides and their mixture with DOTAP

Gene delivery is not only dependent on the transfection ability of the vectors, but also related to their cytotoxicity. As important as transfection ability, it is a determinant for the application of transfection agents. Cytotoxicity of individual peptides and binary peptide/DOTAP mixtures at the doses similar to that applied in the transfection study (shown in Fig. 16) was evaluated in HeLa cells by MTT assay. Results are displayed in Fig. 17. ϵ -(LYK)K10, ϵ -(LKY)K10, ϵ -(YKL)K10 and ϵ -(LYH)K10 are non-cytotoxic with cell viability of over 80%. DOTAP, ϵ -(LYR)K10 and ϵ -(LYRH)K10 display 50% - 70% cell viability, revealing moderate cytotoxicity. Similar or higher cell viabilities are also observed for the mixture peptide/DOTAP, with an exception of ϵ -(LYH)K10/DOTAP (30% cell viability).

Despite their low toxicity, the usage of ϵ -(LYK)K10, ϵ -(LKY)K10 and ϵ -(YKL)K10 in gene delivery is limited by their limited transfection efficiency (Fig. 16). Arg- and His-containing peptides, ϵ -(LYH)K10, ϵ -(LYR)K10 and ϵ -(LYRH)K10, are promising gene delivery vectors in view of their transfection and cytotoxicity data. When ϵ -(LYR)K10 or ϵ -(LYRH)K10 is combined with DOTAP, an enhanced transfection is observed with the cell viability level (50%–70%) being only slightly worse than that displayed by the commercial transfection agent, DOTAP (about 60%).

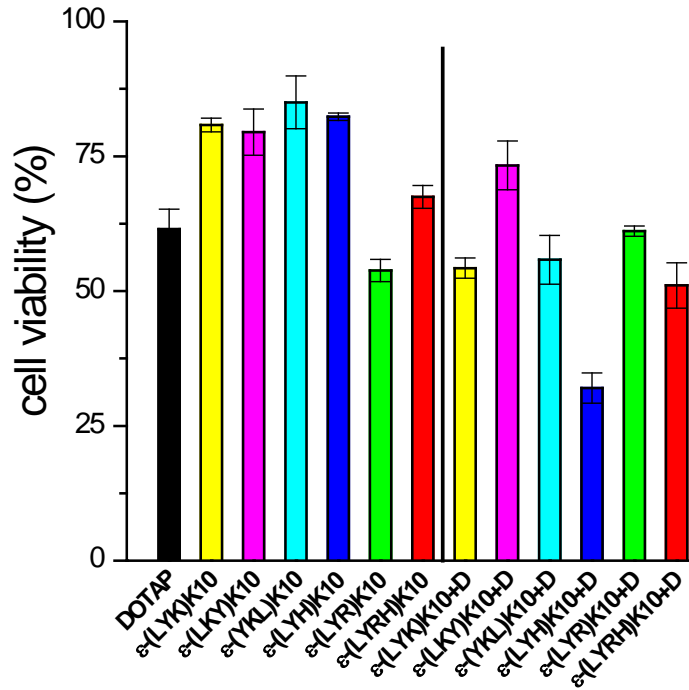


Figure 17. HeLa cell viability after the treatment with DOTAP, ϵ -(LYK)K10, ϵ -(LKY)K10, ϵ -(YKL)K10, ϵ -(LYH)K10, ϵ -(LYR)K10, ϵ -(LYRH)K10 and mixtures DOTAP-peptide at the same concentration as we used in cell transfection.

(Viability is shown as the mean value of 3-5 measurements with standard deviation). The black vertical bar separates data for peptides and mixtures of peptide + DOTAP.

3.1.3 Transfection as a function of complex formulation

According to the data shown in Fig. 16, our branched ϵ -oligolysines enhanced DOTAP-mediated transfection as co-transfection agents. In order to study formulation dependence of the potentiating effect, we measured transfection abilities of complexes in HeLa cells with various formulations using the most effective peptides ϵ -(LYH)K10, ϵ -(LYR)K10 and ϵ -(LYRH)K10. Since one of the major determinants of the transfection properties is the charge ratio between the compaction agent and the DNA (39), transfection complexes were prepared at L/D (DOTAP to DNA charge ratio) = 2, as a function of P/D (peptide to DNA charge ratio). Complex of DOTAP/DNA at L/D = 2 was used as a control and shown in the Fig. 18 C as ϵ -peptide-DNA-DOTAP at P/D equal to 0. To compare with LPD data, the black horizontal lines in Fig. 18 represent the transfection efficiency of the control complex. So the points above the black lines indicate the higher transfection efficiencies than DOTAP/DNA control.

In Fig. 18 A, ϵ -(LYH)K10, ϵ -(LYR)K10 or ϵ -(LYRH)K10 is incapable of inducing gene transfer for $P/D \leq 5$. From $P/D = 10$, GFP expression is observed for all three peptides but they display different transfection efficiencies: ϵ -(LYRH)K10 shows the highest efficiency among three peptides and it is even better than the control results at $P/D = 10$ and 20; ϵ -(LYR)K10 is not as good as ϵ -(LYRH)K10 but its transfection efficiency is higher than ϵ -(LYH)K10. This result indicates that both charge ratio P/D and peptide sequence are determinant factors for transfection activities. An absence of gene translation at the low charge ratio indicates the necessity of the excess positive charges for transfection, which is consistent with previous findings (7,15). With an increase of P/D, the transfection efficiencies of ϵ -(LYRH)K10 and ϵ -(LYR)K10 both decrease after the maximum. This effect is related to the toxicity and explained in Fig. 20.

The effect of ϵ -peptides on DOTAP-induced gene transfer was also studied. Ternary complexes DOTAP/peptide/DNA were prepared according to two protocols differing in mixing order of the components and results are shown in

Fig. 18 B and C. Fig. 18 B shows systems denoted by “(peptide-DNA)+DOTAP”, in which DNA was first condensed by peptides and then peptide/DNA complexes was added into DOTAP solution. Fig. 18 C shows the complexes prepared by adding DNA to the mixture of peptide and DOTAP, indicated by “peptide-DNA-DOTAP”. In Fig. 18 B and C, none of three peptides increases the transfection as compared to DOTAP/DNA complex at $P/D < 5$. A significant enhancement in transfection is observed at $P/D \geq 5$ for peptide ϵ -(LYR)K10 or ϵ -(LYRH)K10 and the enhancing effect is independent on the preparation protocol. However, peptide ϵ -(LYH)K10 fails to improve the DOTAP-induced gene transfer. Comparing ϵ -(LYH)K10 data in Fig. 18 B and C, it is found that the transfection abilities of ternary complexes DOTAP/ ϵ -(LYH)K10/DNA are influenced by the different mixing procedures.

Besides, it is found that the transfection behaviors of binary PD complex and ternary LPD complex containing the same peptides are rather consistent with each other. ϵ -(LYRH)K10 is an efficient transfection vector at $P/D > 5$ and a potentiating co-transfection agent at $P/D \geq 5$. In contrast, neither binary nor ternary complexes containing ϵ -(LYH)K10 give good transfection results. Among the three peptides, ϵ -(LYR)K10 induces the moderate transfection efficiencies in the absence and presence of DOTAP. Those data imply that peptides retain their transfection ability when they are used with liposomes.

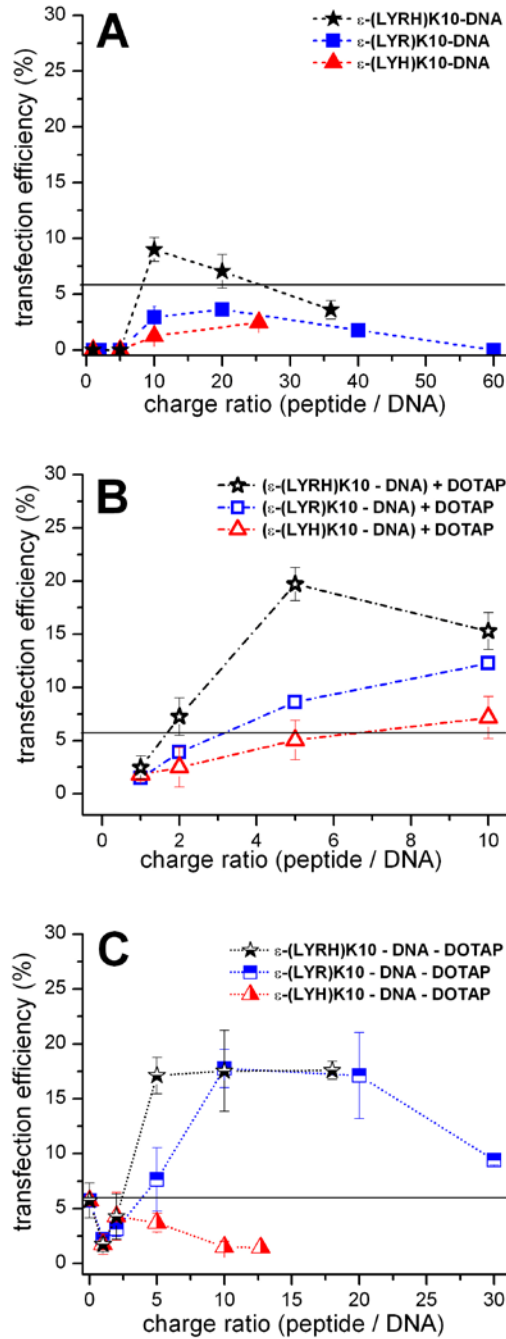


Figure 18. Transfection efficiency plotted as a function of peptide to DNA charge ratio for ϵ -(LYRH)K10, ϵ -(LYR)K10 and ϵ -(LYR)K10 (indicated in the graphs). (A) is for complex ϵ -peptide/DNA. (B) and (C) are for the ternary DOTAP/ ϵ -peptides/DNA complexes differing in mixing order of the components.

In (B), DNA was condensed by peptides first and then peptide/DNA complexes were added into DOTAP. In (C), complexes were prepared by adding DNA to the mixture of peptides and DOTAP. The black horizontal lines mark transfection efficiency of control complex DOTAP/DNA (L/D =2). For the ternary complex of DOTAP/peptide/DNA (shown in panels B and C), the charge ratio of DOTAP to DNA is constant and equal to 2. All data are shown as mean values of 3-5 measurements with standard deviation.

3.1.4 Evaluation of cytotoxicity as a function of concentration

The cytotoxicity of DOTAP, ϵ -(LYH)K10, ϵ -(LYR)K10, ϵ -(LYRH)K10 and peptide/DOTAP mixtures was further studied using HeLa cells as a function of concentration (Fig. 19). Figure 19 A shows that the cell viability decreased significantly when concentration of peptide in the absence of DOTAP was changed from 0.006 to 0.18 mg/ml. Less than 10% cells lose their normal metabolic activities up to 0.018 mg/ml regardless of the nature of α -substituted group. With the increasing concentration, ϵ -(LYH)K10 induces a higher cell viability than ϵ -(LYR)K10 or ϵ -(LYRH)K10. At 0.18 μ mg/ml, ϵ -(LYR)K10 gives 2% of cell viability while 20 % of cells still survived with ϵ -(LYH)K10.

The concentration dependence of the cell viability was also studied for the mixtures peptide/DOTAP. When the concentration of DOTAP is below 0.018 mg/ml and that of the peptide is below 0.009 mg/ml, DOTAP and peptide/DOTAP mixtures display over 80% cell viability and addition of peptide slightly reduces cytotoxicity as compared to pure DOTAP. Different cytotoxic behavior is observed for each peptide as the concentration of their mixtures with DOTAP is increased. For DOTAP = 0.006 mg/ml and peptide = 0.030 mg/ml, ϵ -(LYR)K10 causes no extra cytotoxicity but ϵ -(LYRH)K10 induces \sim 10% less cell viability. Higher cytotoxicity is caused by ϵ -(LYH)K10/DOTAP mixture. All agents result in more than 70% of cell death at DOTAP = 0.018 mg/ml and peptide = 0.09 mg/ml. Thus, ϵ -(LYR)K10 and ϵ -(LYRH)K10 cause no significantly further cytotoxicity than DOTAP alone.

Comparing Fig. 19 A and B one may conclude that cytotoxicity of the mixtures peptide/DOTAP is not a linear and additive function of the peptide and DOTAP content. For example, ϵ -(LYH)K10 is the least toxic without DOTAP but the most harmful in ϵ -(LYH)K10/DOTAP mixtures.

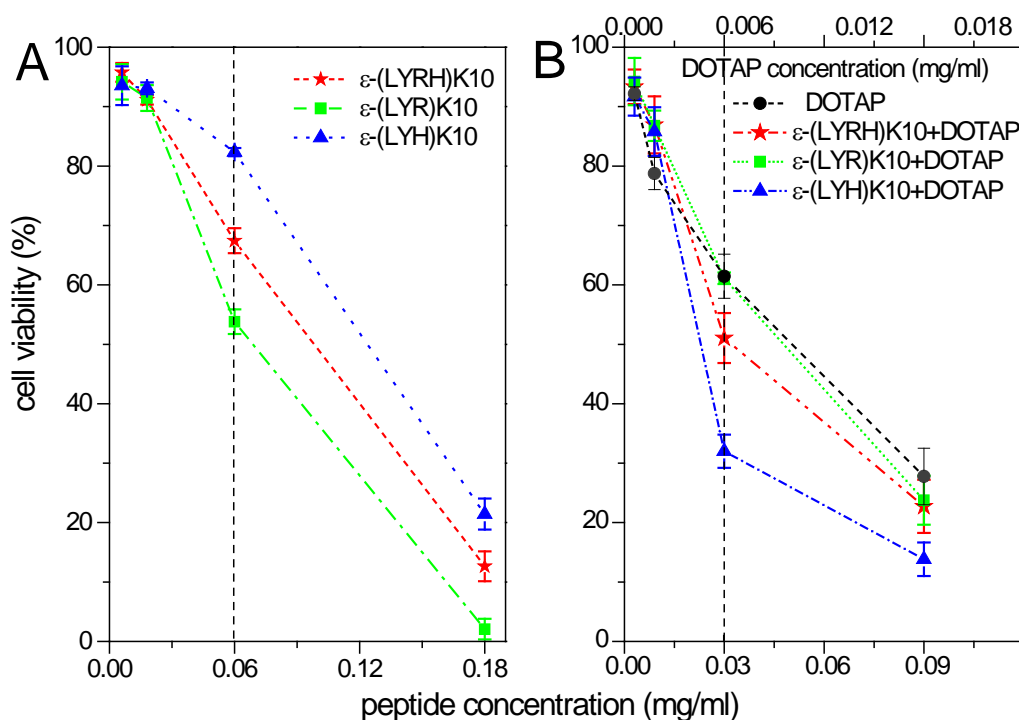


Figure 19. HeLa cell viability as a function of the concentration of transfection agents. Vertical dashed lines show the concentration of transfection agents used in transfection assay (shown in Fig. 7). (Viability is shown as the mean value of 3-5 measurements with standard deviation).

3.1.5 Relation between transfection and cytotoxicity

Figure 20 displays the correlation between transfection efficiency and cytotoxicity in HeLa cells for the three arginine- and histidine-containing peptides having shown the highest transfection potential. At peptide concentration ≤ 0.012 mg/ml, neither transfection nor cytotoxicity is observed. With more peptide present, transfection appears and reaches a maximum (indicated by black dash lines). Although the maximum transfection efficiency occurs at different concentrations, a cell viability of 80% or higher is observed at optimal peptide concentration combined with high transfection. Increase of the peptide concentration results in a reduction of transfection in parallel with an increase of cell death (Fig. 20 A, B). In case of ϵ -(LYR)K10, no transfection is observed when less than 50% of cells survive (Fig. 20 A).

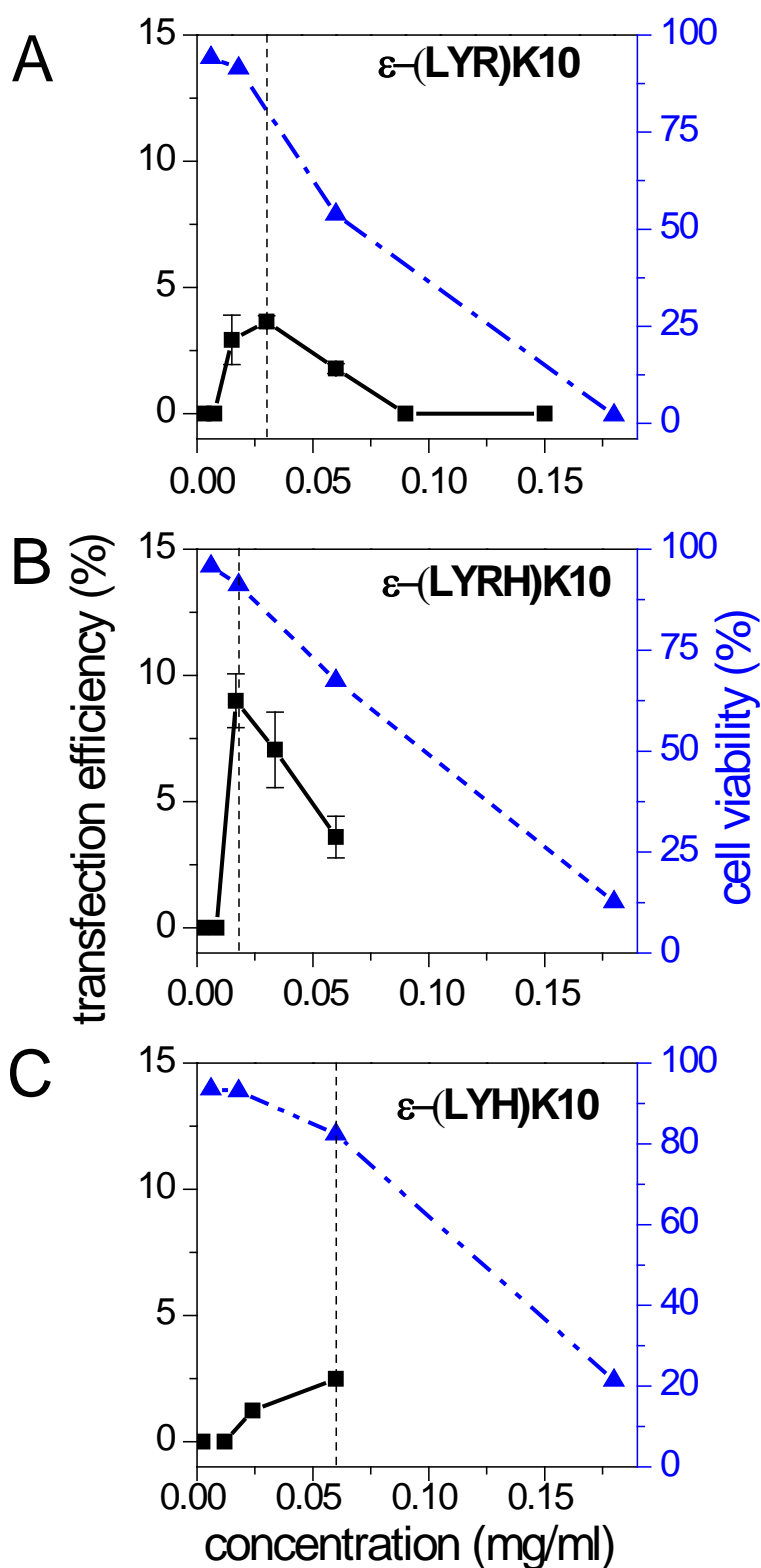


Figure 20. Comparison of HeLa cell transfection efficiency (black points and lines) and HeLa cell viability (blue points and lines) shown as a function of concentration of transfection agents.

Vertical lines show maximum transfection efficiency and the corresponding cell viability. (A) ϵ -(LYR)K10; (B) ϵ -(LYRH)K10; (C) ϵ -(LYH)K10.

3.2 Biophysical studies

3.2.1 pH dependence of DNA condensation by histidine containing ϵ -oligolysines.

A rationale for including the histidine residues in cationic peptides for improved delivery, is based on the “proton sponge” hypothesis (18), whereby the buffering effect of its amine group at the low pH of the endosomes promotes osmotic swelling, disruption of the endosome membrane and release of DNA. The low pH of the endosomes may also promote the condensation ability of the polycationic peptide and further protect DNA. In order to establish the pH dependence of the DNA condensation ability of the ϵ -peptides including histidine, we investigated the DNA condensation in various buffer environments.

Figure 21 presents data of static light scattering during a titration study for ϵ -(LYH)K10 and ϵ -(YKL)K10 (not expected to show pH dependence and included as a control). The values of EC_{50} , the concentration of peptide needed to induce a 50% increase in the scattering intensity, are shown as a function of pH. An increase of EC_{50} with the increase of pH is found for ϵ -(LYH)K10. This means that at lower pH (similar to that in the endosomes), the efficiency of the histidine-containing peptide is significantly higher. This general increase of EC_{50} values with pH can be explained by the decrease of the positive charge of the ϵ -(LYH)K10 due to deprotonation of the imidazole side chain group of histidine (pK_a 6.5). There is also some (relatively small) dependence of EC_{50} values of ϵ -(LYH)K10 on the nature of buffer with EC_{50} values displaying an increase at pH 6.5 in the order citrate > phosphate > HBS. This dependence can be explained by interaction of the anionic component of the buffer with the peptide. Citrate anions being the most negatively charged are capable to interacting with the cationic peptide with a concomitant reduction in its DNA condensation efficiency.

Unlike ϵ -(LYH)K10, increase of pH up to 8.0 has a little effect on the EC_{50} value of ϵ -(YKL)K10. Since the pK_a of the amino group of the lysine in the side chain of the ϵ -(YKL)K10 is about 9, it is expected that this ϵ -oligolysine is fully protonated in the physiological range of pH. The peptides ϵ -(LYH)K10 and ϵ -(YKL)K10 show a similar DNA compaction ability under conditions where all basic groups are protonated (EC_{50} is in the range 0.19 ~ 0.23 μ M for both ϵ -(LYH)K10 and ϵ -(YKL)K10 at the 5 μ M DNA concentration used).

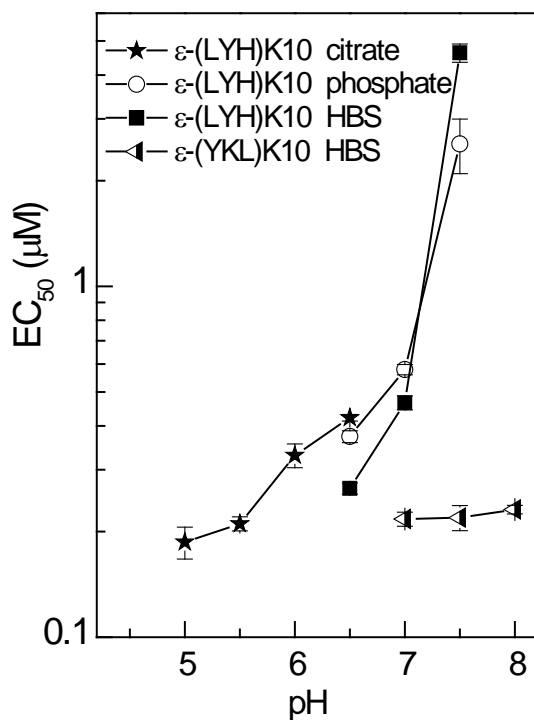


Figure 21. Influence of pH on DNA condensation induced by ϵ -(LYH)K10 and ϵ -(YKL)K10.

The EC_{50} values were determined at pH 5, 5.5, 6.0, 6.5 in citrate buffer; pH 6.5, 7.0, 7.5 in phosphate buffer; pH 6.5, 7.0, 7.5, 8.0 in HBS buffer.

3.2.2 Biophysical properties as a function of complex formulations and the correlation with transfection

We studied transfection abilities as a function of complex formulation (Fig. 18). In parallel, biophysical properties (particles sizes and zeta potential) of those

transfection complexes were investigated and compared with transfection data in Fig. 18.

Results of zeta potential measurements (combined with the transfection data) are collected in Fig. 22. At $P/D = 1$, the zeta potential of all binary peptide/DNA complexes is about -29 mV. For the binary ϵ -(LYRH)K10/DNA and ϵ -(LYR)K10/DNA complexes, a positive zeta potential appears at $P/D = 2$. It increases to $+10 \sim +14$ mV with further increase in P/D . The zeta potential of ϵ -(LYH)K10/DNA complex is close to zero in the range of $P/D = 2$ to $P/D = 25$ (with slight increases with P/D). A similar behavior is observed for the ternary LPD complexes, however, the potential is shifted to much higher positive values. Zeta potentials of the ternary complexes with the ϵ -(LYRH)K10 or ϵ -(LYR)K10 are much higher than these values of the ϵ -(LYH)K10 complexes. This indicates that for a given peptide/DNA charge ratio, the zeta potential is influenced by the presence of DOTAP and the peptide sequence. In the presence of DOTAP, despite some peptide sequence dependence, an addition of peptides always results in a shift of the potential to more positive values relative to the control complex DOTAP/DNA, which has a zeta potential of -30.4 ± 0.8 mV. Importantly, this observation demonstrates an inclusion of the positively charged peptides in the transfection complexes.

Figure 23 combines the results of the data on the particle size of the complexes obtained by DLS method with the results of transfection efficiency. Binary peptide/DNA complexes have the smallest sizes (< 300 nm) at $P/D = 1$ followed by a striking increase at $P/D = 2$ but no steep charge ratio dependence is observed at $P/D > 2$; a rather gradual decrease of the particle size is seen with increase of P/D (except the ternary complex ϵ -(LYH)K10-DNA-DOTAP; Fig. 23). Considering individual peptides, it is observed that ϵ -(LYH)K10 forms larger particles than ϵ -(LYRH)K10 and ϵ -(LYR)K10 (Fig. 23). A common feature is that all peptides drastically increase the size of the control complex DOTAP/DNA at $P/D = 1$. The size of the particles is related to the zeta potential since particles tend to repel each other when their surface charges (represented by zeta potential) are high, otherwise they are more likely to form aggregates

with large diameters. The relation is evident by plotting sizes and absolute values of zeta potential against the charge ratio in Fig. 24.

Biophysical properties of the ternary transfection complexes of DOTAP/ ϵ -peptides/DNA are dependent on peptide type and on the ratio P/D. For the binary complexes of peptide/DNA, on the other hand, the sizes are independent of peptide type or P/D, which can be explained by their instability as inferred from low zeta potential values (Fig. 22). The transfection abilities were tested in HeLa cells and correlations between biophysical properties and transfection efficiency can be revealed by comparing transfection efficiency against zeta potential (Fig. 22) and particle size (Fig. 23). Black lines in Fig. 22 and 23 represent the transfection efficiency of the control complex DOTAP/DNA. Thus, the transfection data above the black lines indicate enhanced transfection efficiencies relative to the DOTAP/DNA control. For the ternary LPD complexes, enhanced transfection is observed when the zeta potential is above +20 mV (this threshold potential is indicated by blue dash line; Fig. 22). As concerns the effect of particle size, enhancement of transfection is seen when the sizes are less than 500 nm (red points below red dash lines in Fig. 23). The complex (ϵ -(LYH)K10-DNA)+DOTAP at P/D =10 is an exception. In contrast, similar correlations cannot be drawn for the binary complexes of peptide/DNA, where zeta potentials do not exceed +20 mV (Fig. 22) and small particle sizes (200~500 nm) appears to be unable to reach transfection efficiency comparable to that of the control DOTAP/DNA mixture (Fig. 23).

The results from zeta potential measurements indicate that the increase of surface charge of LPD complexes induced by addition of the branched ϵ -oligolysines correlates with the augmentation of transfection. Additionally, it is observed that efficiency of transfection increases with decrease of the particle size. This sort of correlation (smaller size – higher efficiency) was observed in many other studies (e.g. (33,56)). However, not only the particle size but also the presence of oligopeptide is important since most effective LPD complexes are larger than those composed of DOTAP/DNA.

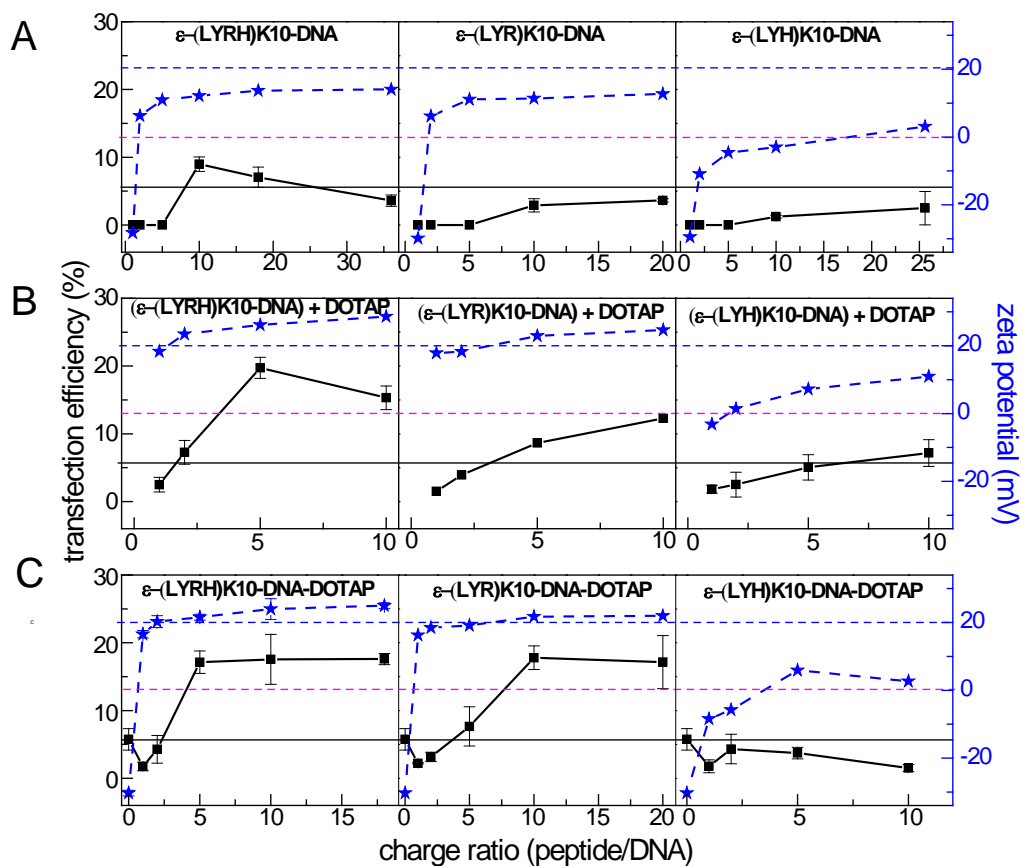


Figure 22. Comparison transfection efficiency (black lines and symbols) and zeta potential (blue lines and symbols) plotted as a function of peptide to DNA charge ratio for ϵ -(LYRH)K10 ϵ -(LYR)K10 and ϵ -(LYH)K10 (indicated in the graphs).

Panel (A) displays data determined for the binary peptide-DNA mixtures. Panels (B) and (C) are for the ternary DOTAP/ ϵ -peptides/DNA complexes differing in mixing order of the components. In panel (B), DNA was condensed by peptides first and then peptide-DNA complex were added into DOTAP; while for complexes peptide-DNA-DOTAP shown in panel (C), complexes were prepared by adding DNA to the mixture of peptides and DOTAP. The black and blue horizontal lines mark respectively transfection efficiency of control complex DOTAP/DNA and zeta potential of +20 mV. The magenta dashed lines indicate zero value of zeta potential. For the ternary complex of peptide/DNA/DOTAP (shown in panels B and C), the charge ratio of DOTAP to DNA is constant and equal to 2. All data are shown as mean values of 3-5 measurements with standard deviation.

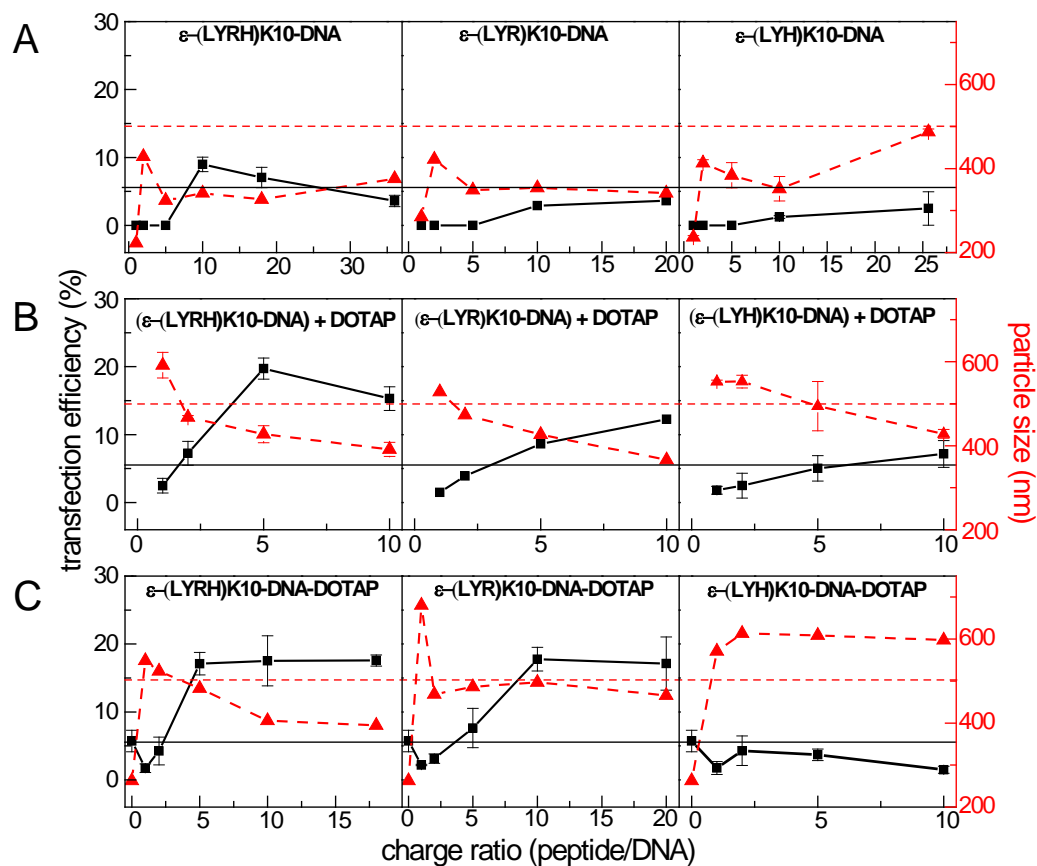


Figure 23. Comparison of transfection efficiency (black lines and symbols) and particle size (red lines and symbols) as a function of peptide to DNA charge ratio.

The black solid line indicates transfection efficiency of the control complex DOTAP/DNA. The red dash line marks particle size of 500 nm. For ternary complexes of DOTAP/ ϵ -peptides/DNA, the charge ratio of DOTAP to DNA is always 2. Panel (A) show the results obtained for binary peptide/DNA complexes. In panel (B), DNA was condensed by peptides first and then peptide-DNA complex were added into DOTAP; while for complexes peptide-DNA-DOTAP shown in panel (C), complexes were prepared by adding DNA to the mixture of peptides and DOTAP. All data are shown as mean values of 3-5 measurements with standard deviation.

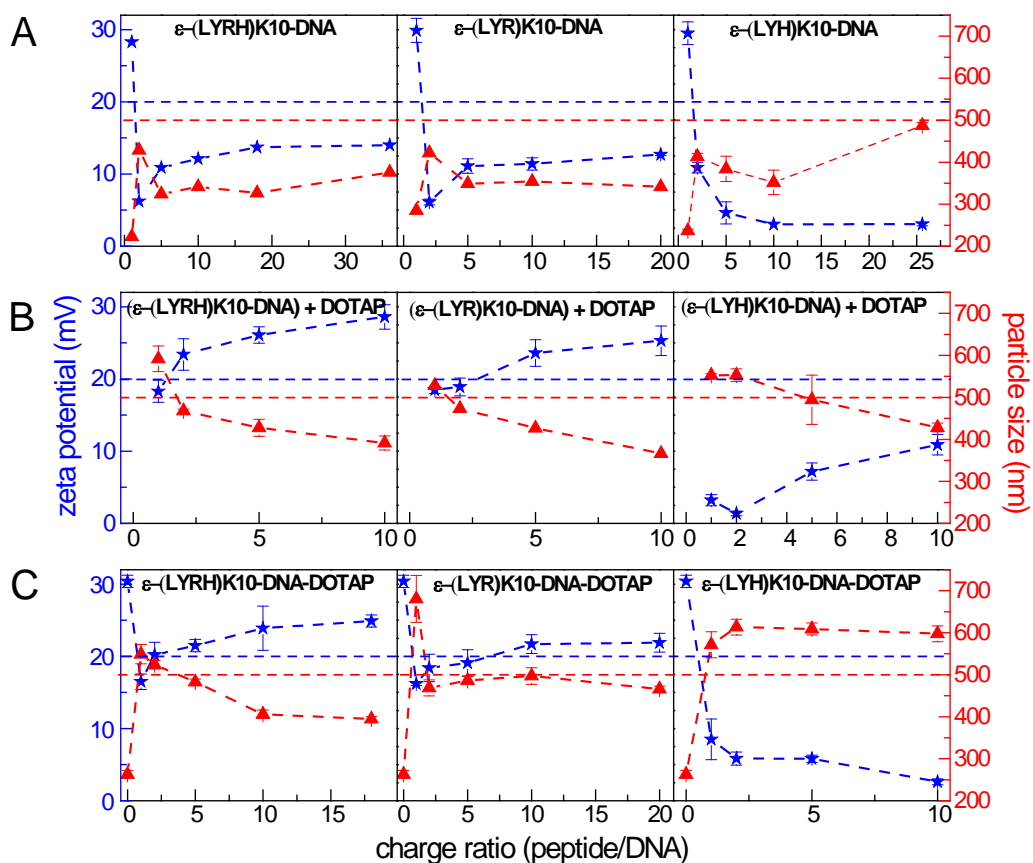


Figure 24. Particle size (red lines and symbols) and absolute values of zeta potential (blue lines and symbols) in dependence of peptide to DNA charge ratio.

The blue dash line indicates zeta potential of +20 mV and red dash line indicates particle size of 500 nm. For ternary complexes DOTAP/ ϵ -peptides/DNA, charge ratio of DOTAP to DNA is 2 for all measurements. Panel (A) show the results obtained for binary peptide/DNA complexes; In panel (B), DNA was condensed by peptides first and then peptide-DNA complex were added into DOTAP; while for complexes peptide-DNA-DOTAP shown in panel (C), complexes were prepared by adding DNA to the mixture of peptides and DOTAP. All data are shown as means \pm SD (n=3~5).

3.3 Studies of supramolecular structure

3.3.1 Supramolecular structure of transfection complexes

The supramolecular structures of the transfection complexes DOTAP/ ϵ -(LYRH)K10/DNA, DOTAP/ ϵ -(LYR)K10/DNA at L/D = 2 with variations of P/D were investigated by synchrotron small angle X-ray scattering (SAXS) and spectra are shown in Fig. 25 A and B and the corresponding repeat distances are listed in Table 1. The complex of DOTAP/DNA at L/D = 2 was examined as a reference. The transfection complexes were prepared in HBS buffer, which is 25 mM Hepes buffer containing 70 mM NaCl, and 0.75 mM Na₂HPO₄. The high ionic strength reduces the entropy gain of the counterion release in the complex formation and the salt counterions at high concentration can compete with polyelectrolytes to bind the opposite charged macromolecules (63). For comparison, the structures of complexes formed in low-salt buffer were also detected, which contains 10 mM Hepes and 0.75 mM Na₂HPO₄.

All complexes showed spectra of typical lamellar phases with interlayer spacing (59.3 Å ~ 61.6 Å) that did not depend on the peptide nature, buffer conditions or peptide/DNA ratio. The two lamellar peaks (denoted q_{001} and q_{002}) follow the relation $d = 2\pi n/q_{00n}$. The interlayer distance, $d = \delta_w + \delta_m$, is consistent with one aqueous layer including the double helical DNA (δ_w about 24 Å in diameter) plus the thickness of a bilayer of pure DOTAP, $\delta_m = 37.2 \pm 0.3$ Å (62). Considering the increased surface charge in the presence of peptides, the structure is schematically illustrated in Fig. 26. Consequently, there is no space between DNA and lipids layer to accommodate peptide molecules. In addition, there is a peak corresponding to the DNA-DNA correlation distance, d_{DNA} , due to DNA helices arranged in parallel within the aqueous region between the bilayers. These observations demonstrate that self-assembly to multilamellar LPD complexes with the arrangement of DNA in between the bilayers is similar to that of the DNA-DOTAP lipid control.

DNA-DNA separation within one aqueous layer is extracted from the relation $d_{\text{DNA}} = 2\pi/q_{\text{DNA}}$, and the results are compiled in Table 1. In Fig. 25 A and B, the control DOTAP/DNA complex in HBS buffer shows a high DNA packing density with DNA-DNA distance (d_{DNA}) of about 28 Å, which is in agreement with literature data for DOTAP-DNA complexes (44). Comparing with the control in absence of peptide, the distance between the DNA rods is increased when peptide is added to the DOTAP/DNA system. The amount of peptide is indicated by the charge ratio of peptide to DNA (P/D). For the lowest peptide/DNA ratio of P/D = 0.3, d_{DNA} is 32.1 Å and 33.4 Å for complex DOTAP/ε-(LYR)K10/DNA (Table 1A) and DOTAP/ε-(LYRH)K10/DNA (Table 1B), respectively. With the addition of peptides, from P/D=0.3 to P/D=5, the DNA-DNA correlation peaks indicated by q_{DNA} shift to lower q (Å⁻¹) values, corresponding to an increase of d_{DNA} (Table 1). At P/D = 5, d_{DNA} increases to more than 37 Å irrespective of peptide (Table 1A and 1B). Compared to the control DOTAP/DNA complex, d_{DNA} increases by around 10 Å at P/D=5. A similar tendency is observed for the complexes prepared in low-salt buffer (Fig. 25 C and D, Table 1C and 1D). For the present lamellar systems, the data do not support an increased DNA condensation in the presence of the peptides (33,56), since the DNA chains in the LPD complexes are packed less tightly than in the DOTAP/DNA complex.

The structural parameters (interlayer spacing and d_{DNA}) of the complexes prepared in low-salt buffer are close to those in HBS (Table. 1). This result indicates that the ionic strength in HBS buffer has no significant influence on the supramolecular structure of the complexes, which is consistent with previous studies reported by Safinya and his co-workers (63).

The in-plane DNA-DNA distance with the increase of peptide content suggests that the peptide molecules infiltrate between the DNA-DNA layers in the aqueous phase between the bilayers and intercalate between DNA chains. The increased DNA-DNA distance is consistent with accommodation of peptides having a relatively thin ε-K10 backbone with a diameter of 3 ~ 4 Å and with the side chains somewhat penetrating into the DNA grooves as schematically

illustrated in Fig. 26. It is necessary to point out that Fig. 26 is a very schematic presentation of the lamellar structures formed by DOTAP, DNA and cationic peptides.

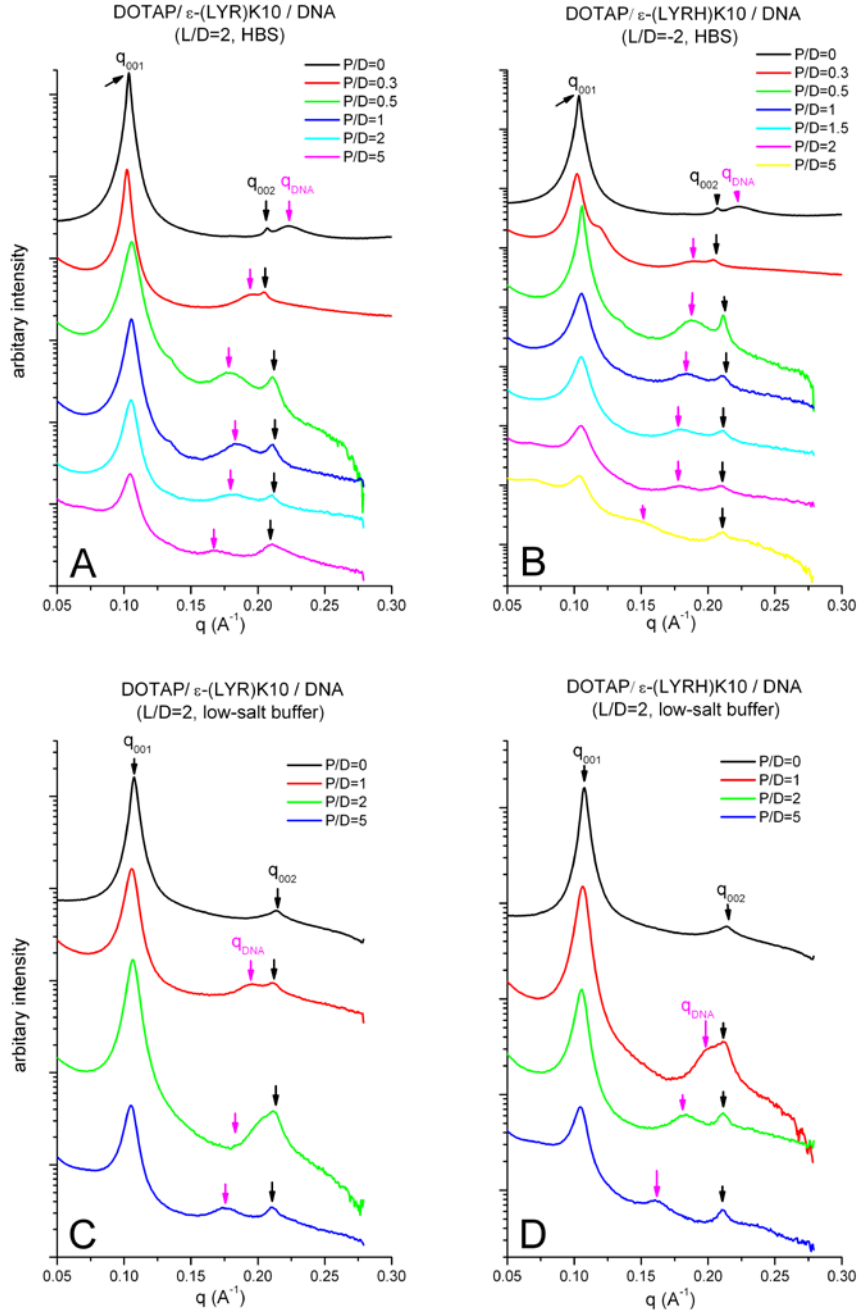


Figure 25. SAXS spectra of (A) DOTAP/ε-(LYR)K10/DNA complexes in HBS buffer, (B) DOTAP/ε-(LYRH)K10/DNA complexes in HBS buffer, (C) DOTAP/ε-(LYR)K10/DNA complexes in low-salt buffer and (D) DOTAP/ε-(LYRH)K10/DNA complexes in low-salt buffer at $L/D=2$ as a function of peptide/DNA (P/D) ratio.

Black arrows indicate the lamellar peaks of the phase with DNA molecules; pink arrows indicate the DNA-DNA correlation peaks. The q value of peaks and calculated distances are given in Table 1.

Table 1. Structural parameters of the LD and LPD complees determined from SAXS spectra shown in Fig. 25.

Table 1A, B, C and D list the q values and the corresponding distance of the synchrotron SAXS spectra shown in Fig. 25 (A), (B), (C) and (D), respectively.

Table 1 (A).							
L/D	P/D	CR _{+/-}	q ₀₀₁ (Å ⁻¹)	q _{DNA} (Å ⁻¹)	q ₀₀₂ (Å ⁻¹)	d interlayer(Å)	d _{DNA} (Å)
2	0	2	0.103	0.22	0.206	61	28.6
2	0.33	2.33	0.102	0.196	0.205	61.6	32.1
2	0.5	2.5	0.105	0.178	0.211	59.8	35.3
2	1	3	0.105	0.184	0.211	59.8	34.1
2	2	4	0.105	0.182	0.211	59.8	34.5
2	5	7	0.104	0.168	0.21	60.4	37.4
Table 1 (B).							
L/D	P/D	CR _{+/-}	q ₀₀₁ (Å ⁻¹)	q _{DNA} (Å ⁻¹)	q ₀₀₂ (Å ⁻¹)	d interlayer(Å)	d _{DNA} (Å)
2	0	2	0.103	0.22	0.206	61	28.6
2	0.33	2.33	0.102	0.188	0.204	61.6	33.4
2	0.5	2.5	0.106	0.188	0.211	59.3	33.4
2	1	3	0.105	0.185	0.211	59.8	34
2	1.5	3.5	0.105	0.179	0.211	59.8	35.1
2	2	4	0.105	0.178	0.21	59.8	35.3
2	5	7	0.104	0.15	0.21	60.4	41.9
Table 1 (C).							
L/D	P/D	CR _{+/-}	q ₀₀₁ (Å ⁻¹)	q _{DNA} (Å ⁻¹)	q ₀₀₂ (Å ⁻¹)	d interlayer(Å)	d _{DNA} (Å)
2	0	2	0.108		0.214	58.2	
2	1	3	0.106	0.196	0.211	59.3	32.1
2	2	4	0.106	0.183	0.212	59.3	34.3
2	5	7	0.105	0.174	0.21	59.8	36.1
Table 1 (D).							
L/D	P/D	CR _{+/-}	q ₀₀₁ (Å ⁻¹)	q _{DNA} (Å ⁻¹)	q ₀₀₂ (Å ⁻¹)	d interlayer(Å)	d _{DNA} (Å)
2	0	2	0.108		0.214	58.2	
2	1	3	0.106	0.2	0.212	59.3	31.4
2	2	4	0.105	0.182	0.211	59.8	34.5
2	5	7	0.104	0.16	0.21	60.4	39.3

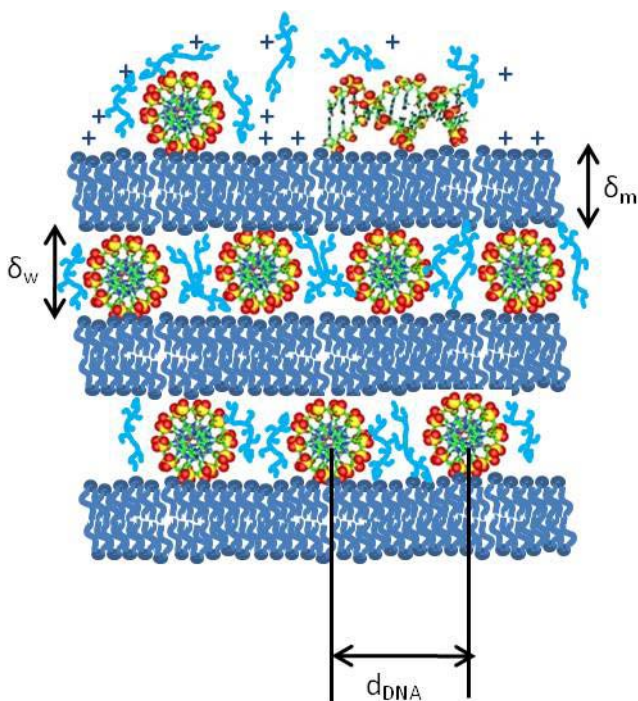


Figure 26. Schematic picture illustrating the lamellar phase of DOTAP/ε-peptide/DNA complexes, with alternating lipid bilayers and DNA monolayers.

Peptides are arranged between DNA chains within the DNA monolayers. The DNA interaxial spacing is d_{DNA} . The interlayer spacing is $d = \delta_m + \delta_w$.

3.3.2 Supramolecular structure at a fixed L/D as a function of P/D

The dependence of supramolecular structure of LPD complexes on P/D were also studied for $L/D = 0.5, 1$ and 1.5 . Figure 27 shows synchrotron SAXS scans of complex DOTAP/ε-(LYR)K10/DNA in HBS buffer at fixed $L/D = 0.5, 1, 1.5$ and 2 as a function of P/D. The peaks q_{001} and q_{002} from the lamellar periodic structures with $d = 2\pi/q_{00n} = 57.6 \sim 61.6 \text{ \AA}$ are independent of the P/D. It is in agreement with a multilamellar structure containing stacked bilayers with intercalated monolayers of DNA of $\sim 20 \text{ \AA}$ in diameter. However, DNA-DNA correlation peaks shift to lower q value with the increased P/D, corresponding to an enlarged distance between DNA chains arranged in parallel within the same layer calculated from $d = 2\pi/q_{\text{DNA}}$. When the d_{DNA} are plotted as a function of P/D (Fig. 28), it appears that the total $CR_{+/-} (L/D + P/D)$ controls d_{DNA} rather than either L/D or P/D. It is observed that d_{DNA} increases significantly upon the

addition of peptides compare to lipids/DNA complex and the augmentation becomes insignificant when total $CR_{+/-}$ is above 3.

At $L/D = 0.5$ (Fig. 27 A), the DNA molecules are tightly packed in the absence of peptides ($d_{DNA} \sim 24.2 \text{ \AA}$). When peptides is added to $P/D=0.5$, an increased d_{DNA} ($\sim 28.6 \text{ \AA}$) is indicated by a peak at q value of $\sim 0.218 \text{ \AA}^{-1}$. But for complexes formed at $P/D=1$ or 1.5 , two peaks appear in the spectra which may be attributed to the DNA-DNA correlation, corresponding to 34 \AA and 29 \AA (respectively indicated by blue and black arrows in Fig. 28). It cannot be explained based on those two spectra at $L/D = 0.5$. SAXS data of ϵ -peptide/DNA complexes provide more information for it and suggest its origin. An explanation is provided in the subchapter 3.3.4.

At $L/D=1$ (Fig. 27 B), d_{DNA} increases by 6.5 \AA from $P/D=0$ (25.9 \AA) to $P/D=0.5$ (32.4 \AA) but the increment of d_{DNA} is less than 4 \AA from $P/D=0.5$ (32.4 \AA) to 2 (36.1 \AA). Beyond $P/D=2$ ($CR_{+/-} = 3$), d_{DNA} is almost unchanged. At $L/D=1.5$ (Fig. 27 C), the increase of d_{DNA} from $P/D=0$ to 0.5 (7.7 \AA) is more considerable than the enhancement of d_{DNA} from $P/D=0.5$ to 1.5 (2.6 \AA). Fig. 27 D shows that the effect of P/D on d_{DNA} for $L/D=2$ is the same as $L/D=1, 1.5$. At $L/D=2$, an increase of P/D from 2 to 5 cannot lead to a significant growth d_{DNA} .

Therefore, Fig 28 indicates that the saturation of d_{DNA} occurs for the complexes of charge ratio $CR_{+/-} \geq 3$ (solid points in Fig. 28). That suggests the $CR_{+/-}$ is the major determinant for the ternary LPD complex formation.

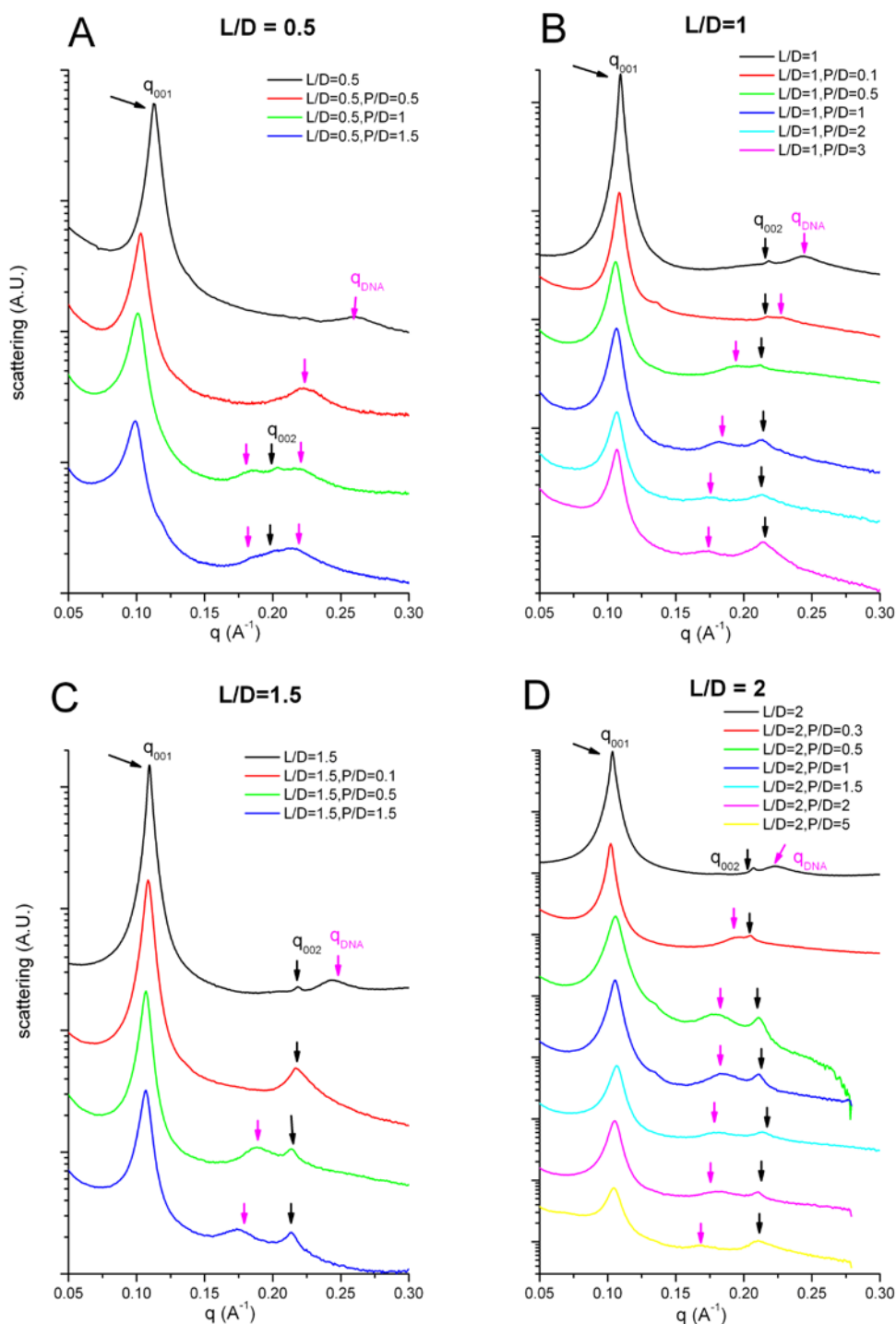


Figure 27. Synchrotron SAXS scans of the complexes DOTAP/ ϵ -(LYR)K10/DNA at the lipid to DNA charge ratio (L/D) 0.5 (A); 1.0 (B); 1.5 (C); and 2.0 (D) determined for the different peptide to DNA charge ratio, P/D .

Black arrows indicate the lipid lamellar peaks; pink arrows indicate the DNA-DNA correlation peaks. Structural parameters of the complexes are shown in Fig. 19 below and listed in Table 2.

Table 2. Structural parameters of the LD and LPD complexes determined from SAXS spectra shown in Fig. 27.

Table 2A, B, C and D list the q values and the corresponding distance of the synchrotron SAXS spectra shown in Fig. 27 (A), (B), (C) and (D), respectively.

Table 2 (A).									
L/D	P/D	CR _{+/−}	q_{001} (\AA^{-1})	q_{DNA} (\AA^{-1})	q_{002} (\AA^{-1})	q_{DNA} (\AA^{-1})	d interlayer (\AA)	d_{DNA} (\AA)	d_{DNA} (\AA)
0.5	0	0.5	0.113	0.26			55.6	24.2	
0.5	0.5	1	0.103	0.22	0.206		61	28.6	
0.5	1	1.5	0.101	0.185	0.204	0.218	62.2	33.9	28.8
0.5	1.5	2	0.099	0.186	0.2	0.213	63.5	33.8	29.5
Table 2 (B).									
L/D	P/D	CR _{+/−}	q_{001} (\AA^{-1})	q_{DNA} (\AA^{-1})	q_{002} (\AA^{-1})	q_{DNA} (\AA^{-1})	d interlayer (\AA)	d_{DNA} (\AA)	d_{DNA} (\AA)
1	0	1	0.109	0.243	0.218		57.6	25.9	
1	0.1	1.1	0.108	0.228	0.217		58.2	27.6	
1	0.5	1.5	0.106	0.194	0.212		59.3	32.4	
1	1	2	0.106	0.18	0.212		59.2	34.9	
1	2	3	0.107	0.174	0.214		58.7	36.1	
1	3	4	0.107	0.17	0.214		58.7	37	
Table 2 (C).									
L/D	P/D	CR _{+/−}	q_{001} (\AA^{-1})	q_{DNA} (\AA^{-1})	q_{002} (\AA^{-1})	q_{DNA} (\AA^{-1})	d interlayer (\AA)	d_{DNA} (\AA)	d_{DNA} (\AA)
1.5	0	1.5	0.109	0.244	0.219		57.6	25.8	
1.5	0.1	1.6	0.108		0.216		58.2		
1.5	0.5	2	0.107	0.188	0.215		58.7	33.4	
1.5	1.5	3	0.106	0.174	0.214		59.3	36.1	
Table 2 (D).									
L/D	P/D	CR _{+/−}	q_{001} (\AA^{-1})	q_{DNA} (\AA^{-1})	q_{002} (\AA^{-1})	q_{DNA} (\AA^{-1})	d interlayer (\AA)	d_{DNA} (\AA)	d_{DNA} (\AA)
2	0	2	0.103	0.22	0.206		61	28.6	
2	0.3	2.3	0.102	0.196	0.205		61.6	32	
2	0.5	2.5	0.105	0.178	0.211		59.8	35.3	
2	1	3	0.105	0.184	0.211		59.9	34	
2	1.5	3.5	0.106	0.18	0.213		59.3	34.9	
2	2	4	0.105	0.182	0.211		59.8	34.5	
2	5	7	0.104	0.168	0.21		60.4	37.4	

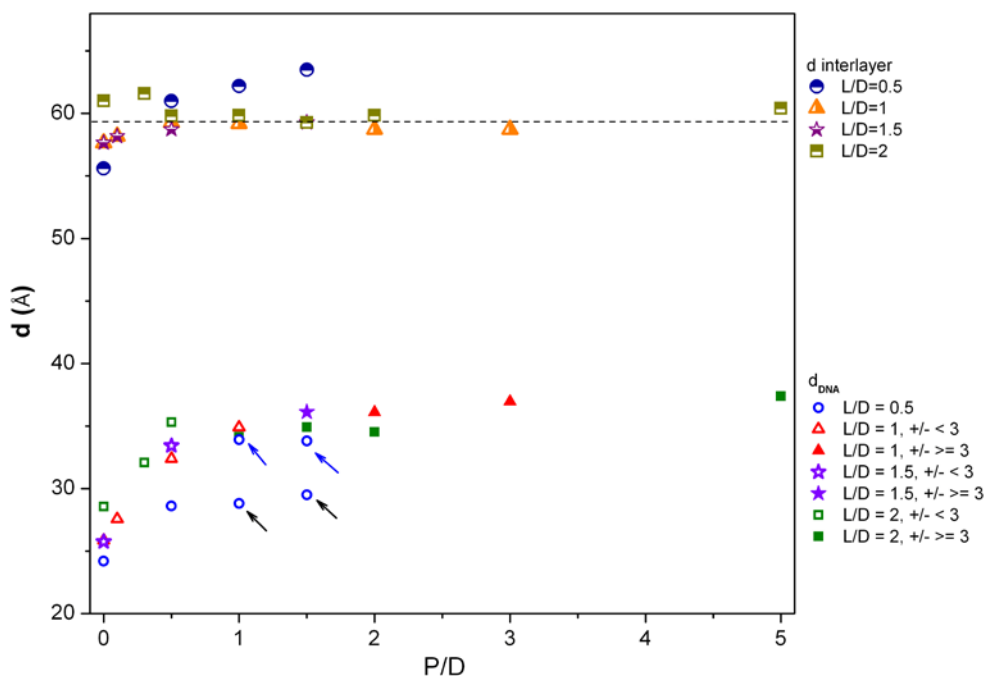


Figure 28. Repeat distances determined from the SAXS spectra in Fig. 27 plotted as a function of the peptide/DNA charge ratio, P/D.

The dashed line is an average of all $d_{\text{interlayer}}$ values. The solid points denote the complex with $CR_{\pm} \geq 3$ and the hollow points denote the complex with $CR_{\pm} < 3$. A group of two points (hollow circles, indicated by black arrows) which fall outside general trend correspond to the second DND-DNA correlation peaks obtained in the series with low lipid/DNA charge ratio $L/D=0.5$ (Fig. 27 A). Another DNA-DNA correlation peak from the same complex is indicated by blue arrows.

3.3.3 Supramolecular structure of ϵ -peptide/DNA complexes

The complex of ϵ -peptide and DNA at $P/D = 1$ displays a structure with low level of organization, with single peak in SAXS spectrum (Fig. 29). The peak is suggested to corresponds to the DNA-DNA correlation in condensed DNA, with a distance $d_{\text{DNA}}^* = 2\pi/q_{\text{DNA}}^*$. For the case of peptide-DNA complexes, we studied two branched ϵ -oligolysines, ϵ -(LYR)K10 and ϵ -(LYH)K10. The peptides ϵ -(LYR)K10 and ϵ -(LYH)K10 showed the highest transfection efficiency in our earlier studies. In ϵ -(LYR)K10/DNA complex, the peak corresponds to $d_{\text{DNA}}^* = 28.6 \text{ \AA}$; while for ϵ -(LYH)K10/DNA, d_{DNA}^* is 31.4 \AA . This small difference in the DNA packing density might be cause by different charge density of ϵ -(LYR)K10 and ϵ -(LYH)K10 and different mode of

interaction of the Arg and His amino acids with DNA. The arginine residue has a positive charge with a flexible side chain capable of penetrating the DNA grooves, whereas histidine is largely uncharged and has bulky side group that require more space in the condensed peptide-DNA complex.

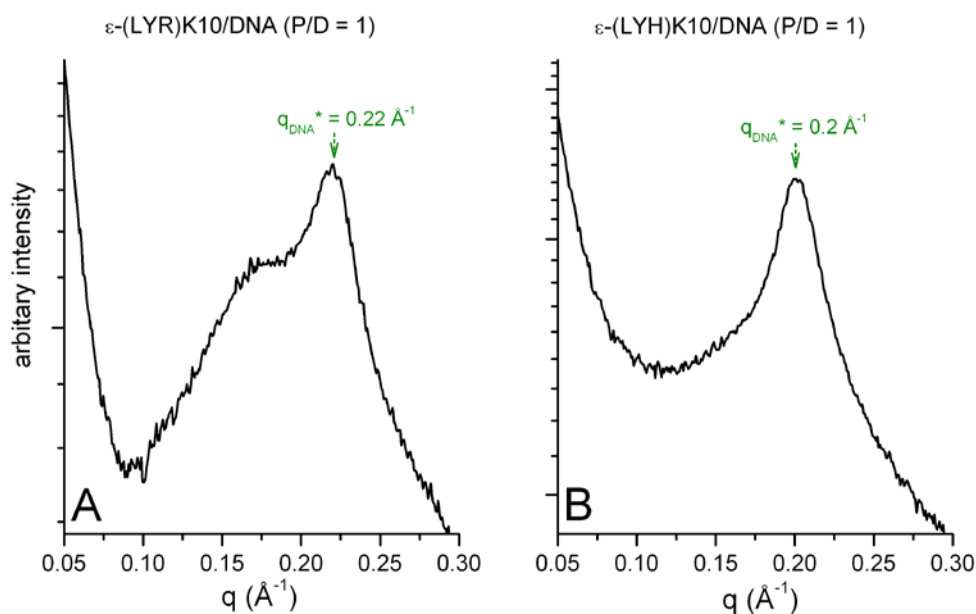


Figure 29. Synchrotron SAXS scans of complex ϵ -(LYR)K10/DNA (A) and ϵ -(LYH)K10/DNA (B) at P/D=1.

Green arrows denote the DNA-DNA correlation peaks in the ϵ -peptide/DNA complex, indicated as q_{DNA}^* and q value of the peak is given.

3.3.4 Supramolecular structure at a $\text{CR}_{+/-}$ as a function of DOTAP-peptide composition

Since the above results suggests $\text{CR}_{+/-}$ is the major factor governing the internal organization of the ternary LPD complex, the structures of LPD complexes were examined as a function of $\text{CR}_{+/-}$ from 1 to 7. At each $\text{CR}_{+/-}$, various formulations were tested to clarify the universality of $\text{CR}_{+/-}$ dependence and identify the roles of peptides and DOTAP in the structure formation.

In Fig. 30, only lipids contribute the positive charges for LD complexes but positive charges are provided by both peptides and lipids for LPD complexes, where the composition of positive molecules is indicated by L/D and P/D. So, when L/D decreases, P/D is increased to compensate the reduction of L/D,

thereby maintaining $CR_{+/-}$. In other words, peptides replace positive charges provided by lipids as L/D decreases for LPD complexes. The roles of peptides and DOTAP in the structure formation could be identified by observing the variation of structures with the extent of the positive charge substitution, which is quantified by P/D.

Fig. 30 present the SAXS spectra grouped accordingly to the value of $CR_{+/-}$ for different compositions of DOTAP and ϵ -(LYR)K10. In Fig. 30 A, the positions of the peaks remain unchanged but the signal intensities of the first lamellar peak q_{001} at $L/D \leq 0.33$ are significantly lower than those at $L/D > 0.33$. At $L/D = 0.17$, the q_{001} almost vanishes. It indicates that the internal organization of LPD complex tends to be less ordered with the reduction of the lipids content. However, it has a limited influence on the structural parameters (interlayer spacing of ~ 59.9 Å and d_{DNA} of ~ 28.3 Å) if the peaks are visible. These results suggest that peptide could participate in the complex formation while lipids are the building blocks to maintain the ordered multilamellar stacks.

The SAXS spectra of complex LPD at $CR_{+/-} = 1.5$ and 2 are shown in Fig. 30 B and C. In Fig. 30 B, DNA-DNA correlation peaks were observed at $q = \sim 0.189$ Å⁻¹ (indicated by blue arrows in Fig. 31), corresponding to d_{DNA} of ~ 33.2 Å. Noteworthy, an extra peak at $q = \sim 0.219$ Å⁻¹ (Table. 3 B, indicated by black arrows in Fig. 31) were found for $L/D=0.67$ and 0.5. The extra peak probably originates from a compact packing of DNA chains corresponding to a d_{DNA}^* of ~ 28.7 Å originating from DNA condensed by peptides in lipid-free aggregates. Ordered structure with a peak at a similar position can be observed for peptide/DNA complex without lipids at a peptide to DNA ratio, P/D = 1 (Fig. 29). Under these conditions, aggregates are formed and visually seen in the solution that give rise to a weak peak in SAXS spectra that is likely to originate from the DNA-DNA correlation in condensed DNA (73). This suggests that two phases with different DNA packing regimes ($d_{DNA}^* \sim 28.7$ Å and $d_{DNA} \sim 33$ Å) coexist at $L/D=0.67$ and 0.5 for the LPD systems. The phase with the larger DNA-DNA spacing is similar to the observations for LPD complexes at higher L/D in Fig. 30 and is a ternary complex, while the aggregate with shorter

DNA-DNA separation is attributed to DNA condensed by peptides. The coexistence of the two phases with different q_{DNA} also occurs for $\text{CR}_{+/-} = 2$ ($d_{\text{DNA}}^* \sim 29.3 \text{ \AA}$ and $d_{\text{DNA}} \sim 34 \text{ \AA}$).

At $\text{CR}_{+/-} = 3$ or 4 (Fig 30 D and E; Table. 4 A and B), d_{DNA} of LPD complex with various formulations are very close ($\sim 35.5 \text{ \AA}$). When $\text{CR}_{+/-}$ is up to 7, d_{DNA} increases to $\sim 38 \text{ \AA}$. The increase of d_{DNA} from $\text{CR}_{+/-} = 3$ to 7 (2.5 \AA) is much less than the shift registered to increase of $\text{CR}_{+/-}$ from 1 to 3 (7.2 \AA). No lipid free peptide-DNA complex is observed at high $\text{CR}_{+/-}$, probably because the amount of lipid is sufficient to involve all available DNA in the multilamellar phase.

The average values of structural parameters (interlayer spacing and d_{DNA}) for each $\text{CR}_{+/-}$ were calculated and plotted against $\text{CR}_{+/-}$ in Fig. 31. The negligible deviations of the average values confirm the similarity of the structural parameters at a fixed $\text{CR}_{+/-}$. In Fig. 31, the interlayer spacing stays at $\sim 59 \text{ \AA}$ independent of $\text{CR}_{+/-}$. Although two DNA packing densities at $\text{CR}_{+/-} = 1.5$ and 2 are observed, it is clear that the increasing $\text{CR}_{+/-}$ to 3 results in the significant enlargement of d_{DNA} but it turns to be insignificant when $\text{CR}_{+/-}$ goes above 3. It is in agreement of the results in Fig. 28, indicating that the internal structure of LPD complex is governed by $\text{CR}_{+/-}$.

The structure parameters of complex DOTAP/DNA at $\text{CR}_{+/-}$ from 1 to 7 are plotted against $\text{CR}_{+/-}$ in Fig. 31, which are close to those of the LPD complexes but d_{DNA} in LD complex is smaller at $\text{CR}_{+/-} = 1, 1.5$ and 3. The discrepancy ($< 3 \text{ \AA}$) is probably due to the distribution of peptides in between DNA chains in LPD complexes. The data for LD complexes is in agreement with previous studies (63).

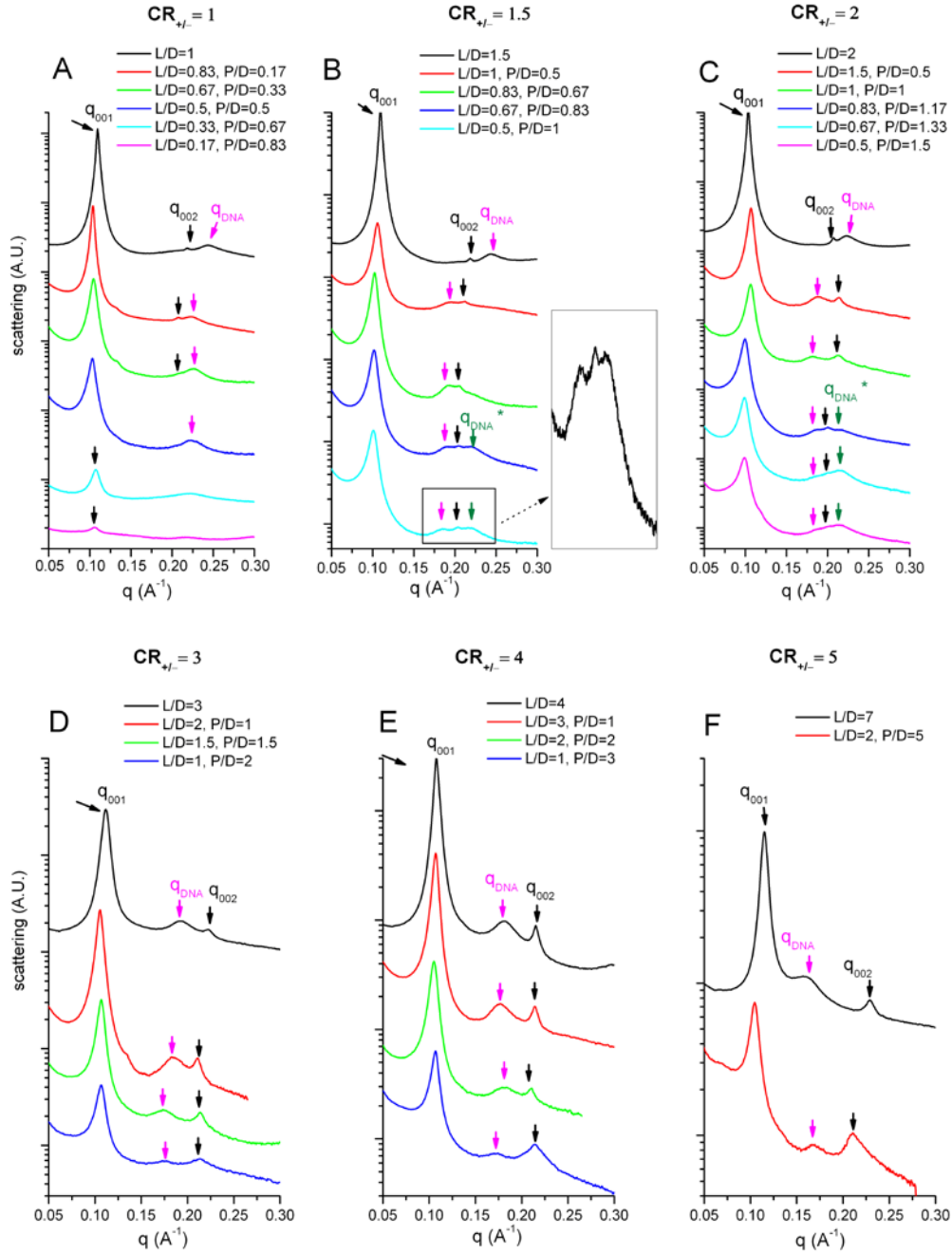


Figure 30. Synchrotron SAXS scans of the complexes DOTAP/ ϵ -(LYR)K10/DNA at the low (1(A); 1.5 (B); 2 (C)) and high (3.0 (D); 4.0 (E); 7.0 (F)) total positive (peptide + DOTAP) to negative (DNA) charge ratio, $CR_{+/-}$, determined for different proportions of peptide and lipid in the mixture (indicated in the graphs).

Black arrows indicate the lipid lamellar peaks; pink arrows indicate the DNA-DNA correlation peaks generated from ternary complexes. Green arrows denote the DNA-DNA correlation peaks in the ϵ -peptide/DNA complex, indicated as q_{DNA}^* . Structural parameters of the complexes are shown in Fig. 31 below and listed in Table 3 and 4. The inset is the enlarged graph of the spectra in the box.

Table 3. Structural parameters of the LD and LPD complexes determined from SAXS spectra shown in Fig. 30.

Table 3 A, B and C list the q values and the corresponding distance of the synchrotron SAXS spectra shown in Fig. 30 (A), (B) and (C), respectively.

Table 3 (A).									
L/D	P/D	CR _{+/−}	q_{001} (\AA^{-1})	q_{DNA} (\AA^{-1})	q_{002} (\AA^{-1})	q_{DNA}^* (\AA^{-1})	d interlayer (\AA)	d_{DNA} (\AA)	d_{DNA}^* (\AA)
1	0	1	0.109	0.243	0.218		57.6	25.9	
0.83	0.17	1	0.104	0.225	0.208		60.4	27.9	
0.67	0.33	1	0.104	0.226	0.211		60.4	27.8	
0.5	0.5	1	0.103	0.22			61	28.6	
0.33	0.67	1	0.107				58.7		
0.17	0.83	1	0.106				59.3		
Table 3 (B).									
L/D	P/D	CR _{+/−}	q_{001} (\AA^{-1})	q_{DNA} (\AA^{-1})	q_{002} (\AA^{-1})	q_{DNA}^* (\AA^{-1})	d interlayer (\AA)	d_{DNA} (\AA)	d_{DNA}^* (\AA)
1.5	0	1.5	0.109	0.244	0.219		57.6	25.8	
1	0.5	1.5	0.106	0.194	0.212		59.3	32.4	
0.83	0.67	1.5	0.102	0.191	0.206		61.6	32.9	
0.67	0.83	1.5	0.1	0.189	0.204	0.219	62.8	33.2	28.7
0.5	1	1.5	0.101	0.185	0.204	0.218	62.2	33.9	28.8
Table 3 (C).									
L/D	P/D	CR _{+/−}	q_{001} (\AA^{-1})	q_{DNA} (\AA^{-1})	q_{002} (\AA^{-1})	q_{DNA}^* (\AA^{-1})	d interlayer(\AA)	d_{DNA} (\AA)	d_{DNA}^* (\AA)
2	0	2	0.103	0.22	0.207		61	28.6	
1.5	0.5	2	0.107	0.188	0.215		58.7	33.4	
1	1	2	0.106	0.18	0.212		59.3	34.9	
0.83	1.17	2	0.1	0.186	0.2	0.216	62.8	33.8	29.1
0.67	1.33	2	0.1	0.183	0.2	0.215	62.8	34.1	29.2
0.5	1.5	2	0.099	0.186	0.2	0.213	63.5	33.8	29.5

Table 4. Structural parameters of the LD and LPD complexes determined from SAXS spectra shown in Fig. 30.

Table 4 A, B and C list the q values and the corresponding distance of the synchrotron SAXS spectra shown in Fig. 30 (D), (E) and (F), respectively.

Table 4 (A).							
L/D	P/D	CR _{+/−}	q_{001} (\AA^{-1})	q_{DNA} (\AA^{-1})	q_{002} (\AA^{-1})	d interlayer (\AA)	d_{DNA} (\AA)
3	0	3	0.11	0.192	0.22	57.1	32.7
2	1	3	0.105	0.184	0.211	59.8	34.1
1.5	1.5	3	0.106	0.174	0.214	59.3	36.1
1	2	3	0.107	0.174	0.214	58.7	36.1
Table 4 (B).							
L/D	P/D	CR _{+/−}	q_{001} (\AA^{-1})	q_{DNA} (\AA^{-1})	q_{002} (\AA^{-1})	d interlayer (\AA)	d_{DNA} (\AA)
4	0	4	0.107	0.18	0.215	58.7	34.9
3	1	4	0.107	0.177	0.214	58.7	35.5
2	2	4	0.105	0.182	0.211	59.8	34.5
1	3	4	0.107	0.172	0.214	58.7	36.5
Table 4 (C).							
L/D	P/D	CR _{+/−}	q_{001} (\AA^{-1})	q_{DNA} (\AA^{-1})	q_{002} (\AA^{-1})	d interlayer (\AA)	d_{DNA} (\AA)
7	0	7	0.114	0.162	0.228	55.1	38.8
2	5	7	0.105	0.166	0.109	59.8	37.9

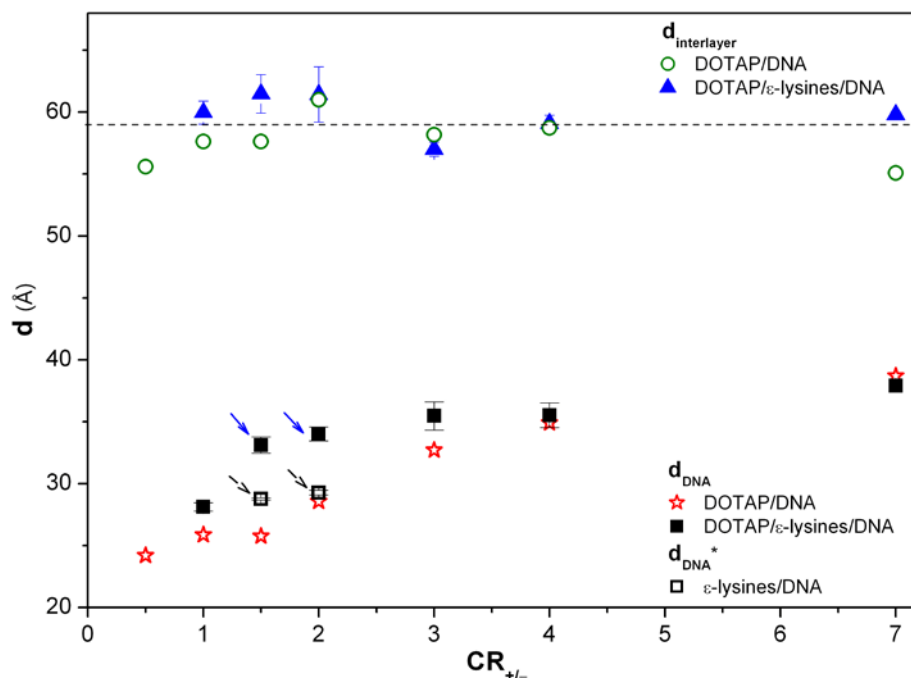


Figure 31. Repeat distances determined from the SAXS spectra in Fig.30 plotted as a function of the total (ϵ -(LYR)K10 + DOTAP)/DNA charge ratio, $CR_{+/-}$.

For the interlayer spacing ($d_{\text{interlayer}}$), circles and triangles are respectively for the binary (DOTAP/DNA) and ternary (ϵ -(LYR)K10/DOTAP/DNA) mixtures; the dashed line is an average of all values $d_{\text{interlayer}}$. For the DNA-DNA distances, values of d_{DNA} were averaged for the binary DOTAP/DNA mixtures (stars) or for the ϵ -(LYR)K10/DOTAP/DNA (squares) compositions for a given $CR_{+/-}$. Solid (indicated by blue arrows) and hollow (indicated by blue arrows) squares are used when SAXS spectra show two peaks of the DNA-DNA correlation at $CR_{+/-} = 1.5$ and 2. Blue arrows indicate the d_{DNA} of 33 ~ 34 Å observed for all the formulations at $CR_{+/-} = 1.5$ and 2. Black arrows indicate the d_{DNA}^* of 28 ~ 29 Å occurring in parallel with the d_{DNA} of 33 ~ 34 Å for $L/D \leq 0.67$, $CR_{+/-} = 1.5$; $L/D \leq 0.83$, $CR_{+/-} = 2$.

3.3.5 Correlation between zeta potential and d_{DNA}

In addition to SAXS studies of internal structure, the zeta potential of LPD complexes were determined with the same formulation as SAXS samples. The zeta potential data are the average values calculated from the all the formulations at a certain $CR_{+/-}$, which are plotted as a function of $CR_{+/-}$ in Fig. 32. The small error bars of the points indicate the similarity of zeta potentials for the LPD complexes differing in the formulations at fixed $CR_{+/-}$.

LPD complexes are negatively charged (~ -28.8 mV) at $CR_{+/-} = 1$ but the zeta potential reverses the sign to ~ + 3 mV when $CR_{+/-}$ increases to 1.5. With the further increase of $CR_{+/-}$, a continuous and sharp rise is followed by a plateau at ~ +17 mV for $CR_{+/-} > 3$, implying that positive charges on the surface are

saturated at $CR_{+/-} = 3$. The zeta potential result supports the LPD model (Fig. 26), where the DNA molecules located on the outer surface is coated by peptides. Interestingly, the variation of the surface potential has a similar tendency to the changes in d_{DNA} inside the complex shown in Fig. 31. In Fig. 32, the enlargement of d_{DNA} from $CR_{+/-} = 1$ to 3 is accompanied by a significant increase of the zeta potential after it reverses from negative to positive. It may demonstrate that the additional positive molecules are included into the LPD complex with cationic peptides absorbed on the particle surface. The plateaus at $CR_{+/-} > 3$ for both d_{DNA} and zeta potential suggest the inclusion of positive molecules is saturated at $CR_{+/-} = 3$.

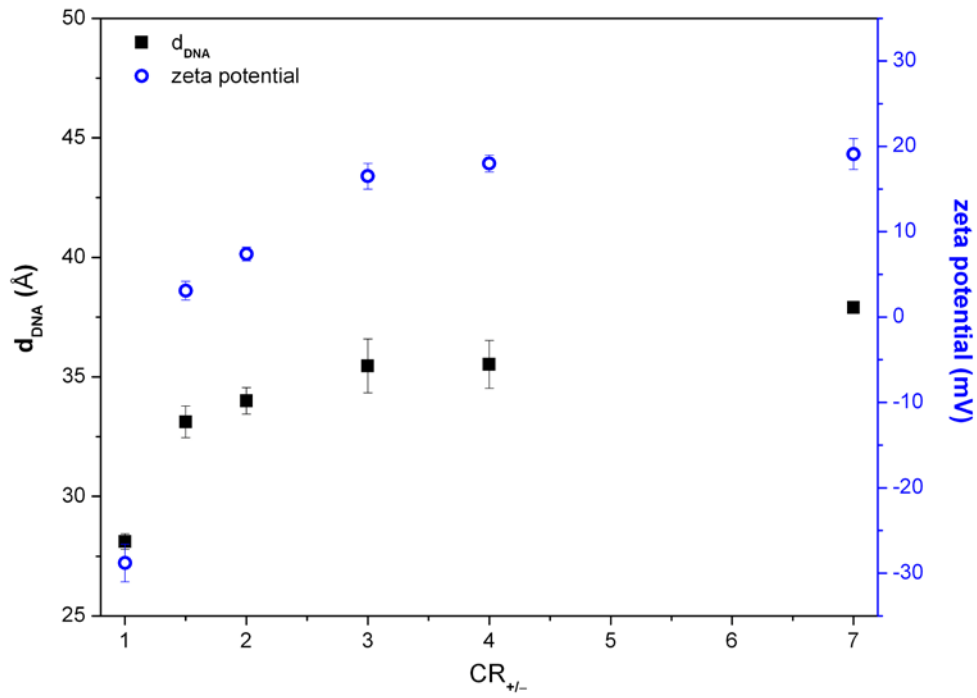


Figure 32. Dependence of d_{DNA} (black squares) and zeta potential (blue circles) of LPD complex as a function of $CR_{+/-}$. Blue circles denote the average zeta potentials calculated from the all the formulations at a certain $CR_{+/-}$. Black squares are the average d_{DNA} of the LPD complexes with various formulations at a fixed $CR_{+/-}$ shown in Fig. 31.

3.3.7 SAXS study of complexes DOPE-DOTAP/ ϵ -(LYR)K10/DNA

Several of the studies using LPD complexes and demonstrating the potentiating effect of cationic peptides in transfection (33,56-59) used a lipid formulation that would form the inverted hexagonal phase in combination with DNA (43). In these lipoplexes, cylinders consisting of DNA coated with a lipid monolayer, arranged in hexagonal packing of the cation lipid-DNA complex. The result of the present study, strongly suggests that in LPD complexes based on lipids that promote a multilamellar lamellar phase, peptides are immersed between the DNA in the hydrophilic region. Therefore, the question arises what is the structure of LPD complexes, based on a lipid formulation that prefers the inverted hexagonal phase.

Consequently, the preliminary SAXS measurements were performed on such a system, in order to address this issue. The liposomes formed by a mixture of DOTAP and the neutral lipid DOPE (1,2-di-(9Z-octadecenoyl)-sn-glycero-3-phosphoethanolamine) prefers the non-bilayer phase and promotes an inverted hexagonal phase in DNA lipoplexes (43). The supramolecular structures of the complex DOPE-DOTAP/ ϵ -(LYR)K10/DNA at $\phi_{\text{DOPE}} = 0.75$, L/D = 1 and 1.5 were examined as a function of P/D. And the results are shown in Fig. 33. The composition of lipids mixture is defined as $\phi_{\text{DOPE}} = \text{DOPE} / (\text{DOPE} + \text{DOTAP})$ weight fraction. The spectra are independent on the L/D and P/D and q values indicated by the black dash lines follow the series: $1:\sqrt{3}:\sqrt{4}:\sqrt{7}:\sqrt{9}$. These results indicate that the complexes display an inverted hexagonal phase. According to the relation between the geometry and q values of the peak, the unit cell spacing of the hexagonal structure (denoted as “a”) can be calculated from q value of the first order of peaks (denoted as q_{10} in Fig. 33). The equation is

$$a = 4\pi / [(3)^{0.5} q_{10}]$$

Fig. 33 shows that q_{10} is 0.108 \AA^{-1} , so the unit cell spacing is 67.4 \AA .

However, we also observed a peak at $q = 0.093 \text{ \AA}^{-1}$ indicated by a green dash line in Fig. 33 (A), which may be due to a pure lipid lamellar phase ($d = 67.6 \text{ \AA}$) co-existing with the hexagonal phase.

25%DOTAP+75%DOPE / ϵ -(LYR)K10 / DNA (L/D=1)

25%DOTAP+75%DOPE / ϵ -(LYR)K10 / DNA (L/D=1.5)

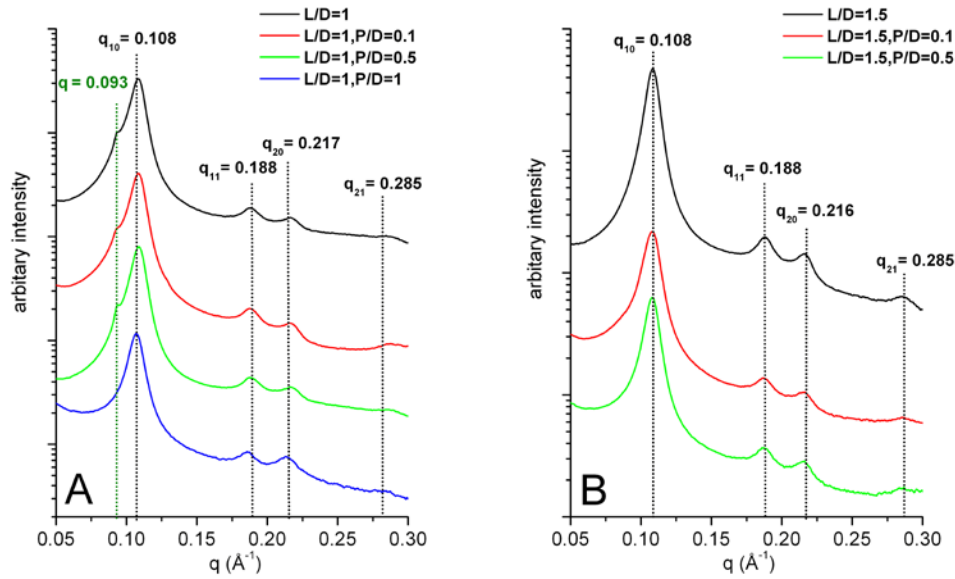


Figure 33. Synchrotron SAXS scans of complex DOPE-DOTAP/ ϵ -(LYR)K10/DNA at L/D=1(A); 1.5(B) pH=7 as a function of P/D.

Black dash lines indicate an inverted hexagonal phase.

The structures at fixed $CR_{+/-} = 1.5$ were also studied as a function of lipids-peptide composition, which is shown in Fig. 34. The inverted hexagonal phases with a unit cell spacing of $a = 67.4$ \AA are independent on the complex formulation. The thickness of lipids monolayer is around 20 \AA , so the diameter of the micellar void in the structure is ~ 28 \AA , which is sufficient for a DNA double-helix strand. It is not clear that whether the peptides are included into this structure or not. Clearly further studies, investigating other biophysical properties as well as the transfection properties of these LPD complexes must be undertaken, in order to understand the supramolecular structure and how cationic peptides take part in the complexes and contribute to transfection.

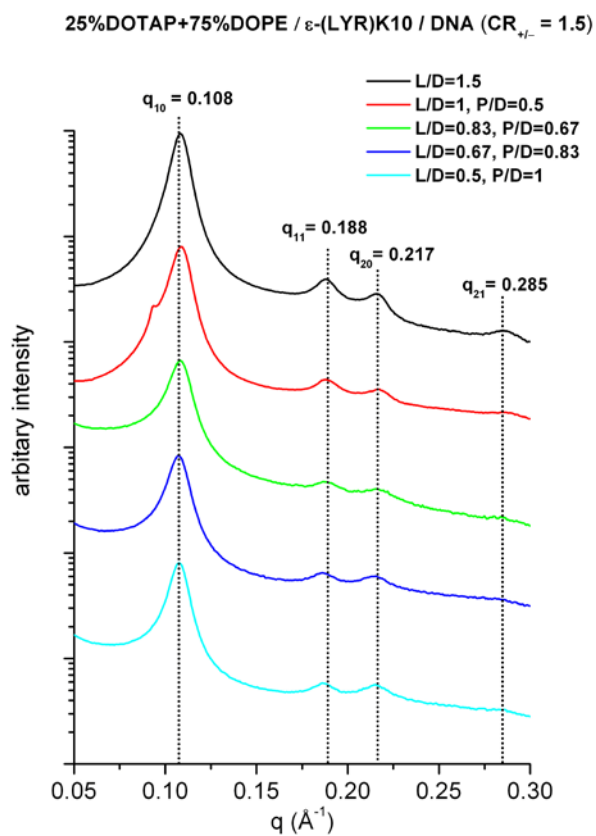


Figure 34. Synchrotron SAXS scans of complex DOPE-DOTAP / ϵ -(LYR)K10/DNA at $CR_{+/-} = 1.5$ as a function of DOTAP-peptide composition.
Black dash lines indicate an inverted hexagonal phase.

4. Discussion and conclusions

4.1 Gene delivery abilities

The data obtained in the present study confirms and extends the conclusion of earlier work (67) that α -substituted ϵ -lysines are promising gene delivery vectors. The arginine/histidine-bearing peptides ϵ -(LYH)K10, ϵ -(LYR)K10 and ϵ -(LYRH)K10 show a potential of being successful DNA carriers compared to the peptides with lysine in the side chain, ϵ -(LYK)K10, ϵ -(LKY)K10 and ϵ -(YKL)K10 (Figs. 16 and 17). Histidine-containing peptides are believed to facilitate the gene transfer relied on the enhancement of DNA endosomal escape through the “proton sponge” effect of the imidazole group of histidine (18,32-33,52,69). Mixson and co-workers (33,52,69) reported that a series of histidine-lysine co-polymers in combination with cationic liposomes significantly enhanced the transfection efficiency. pH dependence of ϵ -(LYH)K10-induced DNA compaction within pH 5.0~7.5 (Fig. 21) indicates that histidine-containing branched ϵ -oligolysines studied in the present work could buffer and disrupt endosomes by mechanism similar to proposed earlier (18).

Comparison of transfection efficiencies induced by ϵ -(LYK)K10 and ϵ -(LYR)K10 demonstrates that gene expression is greatly increased when lysine in the side chain is substituted by arginine. The advantage of Arg over Lys residue was reported for protamine molecules mediated transfection (57). Although Lys and Arg have many similar properties, the special role of arginine was found in cell membrane translocation (74-75). Arginine-rich domains were found in many membrane-permeable peptides (74), therefore a variety of arginine-rich peptides were studied as gene delivery agents (59-60,76-79). The presence of both His and Arg in the ϵ -(LYRH)K10 was expected to combine advantages of these two amino acids found in different transfection studies. The result indicates that multiple advantageous components for transfection can be integrated into a single peptide by using our ϵ -oligolysine backbone design. The

ϵ -(LYRH)K10 showed the best transfection in HEK 293 and HeLa cells while this peptide is not as good as ϵ -(LYR)K10 or ϵ -(LYH)K10 in Mewo cell, indicating cell line dependence. The variation of transfection results between cell lines is interesting and needs further investigation in regard to cell-targeting delivery. The addition of cell-targeting components in peptide may improve transfection.

A number of studies reported that combined effect of lipids and polycations can greatly enhance transfection efficiency (33,52,56,59-60,69). In agreement with that finding, it is observed that in many cases the ϵ -lysine based peptides are effective co-agents in DOTAP-mediated transfection, i.e. peptide/DOTAP mixtures are more effective than DOTAP alone. The most significant enhancement of transfection is achieved when ϵ -(LYH)K10, ϵ -(LYR)K10 or ϵ -(LYRH)K10 is combined with DOTAP regardless of cell line. Although the transfection efficiencies of ϵ -(LKY)K10 and ϵ -(YKL)K10 are very low, it is still possible to achieve enhanced transfection in A549 and Mewo cells when these peptides are combined with DOTAP.

4.2 Correlations between biophysical parameters and transfection

In addition to the chemical and biological nature of transfection agents, physical parameters of transfection complex influence the efficiency, of which the most studied are size and zeta potential (33,56,58-59,66,80-81). Optimal zeta potential allows strong cell association and size limitation indicates that ternary transfection complexes share a common cell internalization pathway. Zeta potential correlates with the affinity of transfection complexes for charged cell surfaces, so the positive value of zeta potential is essential for effective transfection (39). It was reported that the excess positive charges provided by polycations increased surface charges as compared to the negatively charged complexes of DNA and lipids (58-59). That might explain potentiating effect of peptide addition to the DNA/DOTAP mixtures observed in our study.

As shown in Fig. 22 B and C, ternary DOTAP/ ϵ -peptide/DNA complexes have positive zeta potential up to $> +20$ mV, while the complex DOTAP/DNA is negatively charged (~ -30.4 mV). It was reported that at low concentration of salt, particles formed by interaction of cationic lipid and DNA were positively charged at CR > 1 (63). However, in salt solution mimicking conditions of transfection studies (high salt), complexes of DNA with cationic vectors have negative zeta-potential (58-59,82). This difference in sign of the zeta potential is explained by competition between lipids and monovalent cations for neutralization of the negative charge of the DNA absorbed on the surface of the particles. In low salt conditions, there is little competition between lipids and Na^+ for the binding to DNA. Hence, DNA absorbed on the surface of the LD particles is coated by cannot reverse the overall positive charge of the LD complex (since lipid is present in excess). However, at about 70 mM Na^+ in HBS buffer, the concentration of Na^+ is high enough to modulate the lipid coating at the surface. Besides, small ions are more flexible to bind to the phosphate groups of DNA because cationic lipids are restricted by the hydrophobic interaction. So Na^+ could release the excessive lipid from the DNA absorbed on the surface and the zeta-potential becomes negative. The ϵ -oligolysines used in the present study carry a high positive charge (+21) and according to our data (12), when the peptides are added, 70 mM Na^+ is not enough to compete with ϵ -oligolysine for the binding to DNA. As a result, most of the particles in the LPD mixtures have positive and relatively high zeta-potential due to the excessive absorption of the ϵ -oligolysines on the outer surface of the particles formed as illustrated in Fig. 26.

Oberle et al (71) found that part of the plasmid DNA in the lipoplex (charge ratio of lipid/DNA=3) was not covered with lipids. This imperfection in the lipoplex formation leads to a partial exposure of plasmid DNA on the surface of the particles. The partial DNA exposure was observed by Huebner et al using cryoelectron microscopy as a multilamellar structure with unclosed bilayers at charge ratio (lipid/DNA) 5 and open rims of the outer lamellae at charge ratio (lipid/DNA) 1.1 (83). Our results suggest that peptides in the ternary LPD

complex cover the exposed DNA on the surface of the transfection complex contributing to the increased zeta potential in the presence of peptides.

It is also clear that particle size is an important parameter influencing transfection. However, no common optimal size is found for most transfection systems. Endocytosis is widely reported as the major pathway of cell internalization and there exist various endocytosis routes with different size limitations (7,84). As concerns variations of particle size related to the addition of co-polymers to the DNA/lipid recipes, results reported in literature are contradictory (33,56,59). It was reported that addition of poly(L-lysine) or branched histidine-lysine co-polymers to cationic liposome/DNA mixtures reduced the particle size (33,56) while addition of HIV-1 Tat protein transduction domain peptide enlarged it (59). The data are always limited in their studies and probably not enough to present the tendency of the sizes variation (33,56,59). So it is likely that those reported results only cover some small parts of the entire tendency, i.e. some fragments of the whole curve. The conflicting results may result from the partial coverage.

In our study, a variety of complex formulations were used to depict the size variation. At all studied charge ratios, it is observed that the sizes of DOTAP/ ϵ -peptide/DNA complexes are always larger than these of DOTAP/DNA. Concerning the correlation of biophysical properties and transfection efficiency, it is found that for the DOTAP/ ϵ -peptide/DNA complexes, a universal optimal zeta potential (above +20 mV) and particle size (less than 500 nm) might serve as important condition for effective transfection. As far as we know, such a correlation has not previously been pointed out and analyzed in a systematic way by correlating these physico-chemical properties with transfection.

4.3 The universal properties of supramolecular structures

SAXS data allowed us to conclude that self-assembly to a lamellar phase was spontaneously initiated both for the control complex DNA/DOTAP (as expected and shown before (62-63)) and for ternary complexes DOTAP/ ϵ -

peptide/DNA (LPD). The interlayer spacing of the multilamellar stacks is consistent with the thickness of one layer of double helical DNA and a bilayer of pure DOTAP. DNA chains confined within the DNA layer are arranged in parallel and the interaxial distance (d_{DNA}) varies with $\text{CR}_{+/-}$. The peptides in LPD complexes locate between the parallel DNA chains. Although peptide could participate in the complex formation, lipids are the building blocks to maintain the ordered multilamellar stacks, indicated by the less ordered structure at low L/D (Fig. 30 A).

To the best of our knowledge, this is the first time that the supramolecular structure of a ternary LPD complex that demonstrate an enhancement of transfection efficiency compared to the pure lipid-DNA system, has been directly probed. For liposome formulations based on lipid DOTAP, lamellar complexes are preferred due to the lipid packing constraints, while formulations including lipid DOPE form the inverted cylindrical hexagonal phase.

It is found that the increase of $\text{CR}_{+/-}$ to 3 results in a significant enlargement of d_{DNA} compared to $\text{CR}_{+/-}=1$ for LPD complexes. The charge ratio (CR) dependence of d_{DNA} was also observed for complex lipid/DNA (where either cationic lipid or its mixture with neutral lipids was used) (63). It could be explained by the intake of excess positive molecules into the complexes at $\text{CR}_{+/-}>1$. The increase of d_{DNA} allows DNA to bind more positive molecules.

The complex formation is driven by the counterion release when the opposite charged molecules neutralize each other (63,85-86). This mechanism favors the formation charge-neutral ($\text{CR}_{+/-}=1$) complexes for which there is perfect charge neutralization (63,85-86). However, the overcharged ($\text{CR}_{+/-}>1$) LPD complexes seem to absorb the additional positive molecules compared to $\text{CR}_{+/-}=1$, indicated by the increase of d_{DNA} .

A thermodynamic analysis of non-stoichiometric mixtures of oligo/poly anions (DNA) and oligo/polycations (ϵ -oligolysines; cationic lipid in bilayer or in liposome can be considered as a polycation) explains this behavior. Under non-

stoichiometric conditions (when $CR_{+/-}$ is not equal to 1.0), electrostatic interactions of all oligo/polycations with all oligo/polyanions is more favorable than the situation when the charges of polyanions is exactly balanced by the cationic ligands, with any excess of oligocations being free (not interacting with DNA). The origin of this effect is entropic. Both oligo/polycations and oligo/polyanions have large free energies, which can be lowered by entering into complexes and releasing counterions (63,85-86). It appears that total release of monovalent counterions is larger when the charge density of all polyionic species is reduced compared to the counterion release observed upon formation of 1:1 DNA:oligocation (or lipid) complex with excess oligo/polycations remaining free. This effect was discussed in detail for oligo/polycation-DNA systems (87-88).

A plateau of d_{DNA} versus $CR_{+/-}$ dependence was observed for $CR_{+/-} > 3$, implying a saturation of the positive molecules in the complexes. A remarkably similar saturation behavior is theoretically predicted for oligocation/DNA non-stoichiometric complexes under conditions of DNA excess (that is $CR_{-/+} > 3$) (87-88). Observation of saturation for a system with reversed charge stoichiometry (with excess of oligocations) indicates general polyelectrolyte behavior of polycation/polyanion mixtures. The limitation of intake of the excess cationic lipids or peptide may be due to electrostatic repulsion between the lipid bilayers. Since the interaction between DNA and lipids overcome the electrostatic repulsion between lipid bilayers to form the multilamellar stacks (61), the limitation of d_{DNA} growth keeps complexes away from the disassembly. It is found that both DNA packing density (d_{DNA}) and surface charge of LPD complexes correlate with $CR_{+/-}$.

Both SAXS and DLS data demonstrate that ϵ -peptides are incorporated into the LPD complex. The function of DOTAP might be disturbed by membrane fusion or serum interference, especially during *in vivo* transfection (3,43,65). Inclusion of the peptides into DOTAP/DNA complexes provides additional protection for DNA on a route from the extracellular solution to cell nucleus. Peptides possibly assist gene delivery as follow-on vectors even after DOTAP coating is abolished, e.g. by protecting DNA from digestion by DNase I in the cytosol.

Besides, the functionality of peptides can be protected by DOTAP coating. Due to the multiple barriers in the gene delivery process (3), such organization may be significant for the final successful gene expression and responsible for the synergistic effect of branched ϵ -oligolysines and cationic liposome DOTAP in transfection. Therefore, our results suggested an underlying mechanism for the enhanced transfection in LPD system. It is consistent with our transfection results in Fig. 18, which shows that LPD complexes are more efficient than PD complex and peptides tend to retain their transfection abilities in LPD complexes.

The present ternary LPD transfection system, based on ϵ -peptides, forms the basis for further optimization of transfection properties by the use of different and more effective liposomes and by further optimization of the properties of the peptide side chain by the inclusion of a nuclear localization signal sequence as well as cell targeting sequences. Observed differences in transfection efficiency between different cell lines might be exploited for development of cell-type specific drugs.

References

1. Bloomfield, V.A. (1997) DNA condensation by multivalent cations. *Biopolymers*, **44**, 269-282.
2. Bloomfield, V.A. (1996) DNA condensation. *Curr.Opin.Struct.Biol.*, **6**, 334-341.
3. Read, M.L., Logan, A. and Seymour, L.W. (2005) Barriers to gene delivery using synthetic vectors. *Adv.Genet.*, **53PA**, 19-46.
4. Bloomfield, V.A. (1991) Condensation of DNA by multivalent cations: considerations on mechanism. *Biopolymers*, **31**, 1471-1481.
5. Widom, J. and Baldwin, R.L. (1980) Cation-induced toroidal condensation of DNA studies with $\text{Co}^{3+}(\text{NH}_3)_6$. *J.Mol.Biol.*, **144**, 431-453.
6. Duguid, J.G. and Bloomfield, V.A. (1995) Aggregation of melted DNA by divalent metal ion-mediated cross-linking. *Biophys.J.*, **69**, 2642-2648.
7. Mintzer, M.A. and Simanek, E.E. (2009) Nonviral vectors for gene delivery. *Chem.Rev.*, **109**, 259-302.
8. Segura, T. and Shea, L.D. (2001) Materials for non-viral gene delivery. *Annu. Rev. Mater. Res.*, **31**, 25-46.
9. Vilfan, I.D., Conwell, C.C., Sarkar, T. and Hud, N.V. (2006) Time study of DNA condensate morphology: implications regarding the nucleation, growth, and equilibrium populations of toroids and rods. *Biochemistry*, **45**, 8174-8183.
10. Plum, G.E., Arscott, P.G. and Bloomfield, V.A. (1990) Condensation of DNA by trivalent cations. 2. Effects of cation structure. *Biopolymers*, **30**, 631-643.
11. Iwaki, T., Saito, T. and Yoshikawa, K. (2007) How are small ions involved in the compaction of DNA molecules? *Colloids Surf. B Biointerfaces*, **56**, 126-133.
12. Korolev, N., Berezhnoy, N.V., Eom, K.D., Tam, J.P. and Nordenskiöld, L. (2009) A universal description for the experimental behavior of salt-(in)dependent oligocation-induced DNA condensation. *Nucleic Acids Res.*, **37**, 7137-7150.
13. Manning, G.S. (1978) The molecular theory of polyelectrolyte solutions with application of the electrostatic properties of polynucleotides. *Q.Rev.Biophys.*, **11**, 179-246.
14. Eliyahu, H., Barenholz, Y. and Domb, A.J. (2005) Polymers for DNA delivery. *Molecules*, **10**, 34-64.
15. Gao, X., Kim, K.-S. and Liu, D. (2007) Nonviral gene delivery: What we know and what is next. *AAPS J.*, **9**, E92-E104.
16. Schaffer, D.V., Koerber, J.T. and Lim, K.I. (2008) Molecular engineering of viral gene delivery vehicles. *Annu. Rev. Biomed. Eng.*, **10**, 169-194.
17. Saccardo, P., Villaverde, A. and González-Montalbán, N. (2009) Peptide-mediated DNA condensation for non-viral gene therapy. *Biotech. Adv.*, **27**, 432-438

18. Martin, M.E. and Rice, K.G. (2007) Peptide-guided gene delivery. *AAPS J.*, **9**, E18-E29.
19. Yang, N.S. and Sun, W.H. (1995) Gene gun and other non-viral approaches for cancer gene therapy. *Nat. Med.*, **1**, 481 - 483.
20. Neumann, E., Schaefer-Ridder, M., Wang, Y. and Hofschneider, P.H. (1982) Gene transfer into mouse lyoma cells by electroporation in high electric fields. *EMBO J.*, **1**, 841-845.
21. Luo, D. and Saltzman, W.M. (2000) Synthetic DNA delivery systems. *Nat.Biotechnol.*, **18**, 33-37.
22. Nakase, I., Kobayashi, S. and Futaki, S. (2010) Endosome-disruptive peptides for improving cytosolic delivery of bioactive macromolecules. *Biopolymers*, **94**, 763-770.
23. Zhdanov, R.I., Podobed, O.V. and Vlassov, V.V. (2002) Cationic lipid-DNA complexes—lipoplexes—for gene transfer and therapy. *Bioelectrochemistry*, **58**, 53– 64.
24. Kichler, A., Leborgne, C., Marc, J., Danos, O. and Bechinger, B. (2003) Histidine-rich amphipathic peptide antibiotics promote efficient delivery of DNA into mammalian cells. *Proc.Natl.Acad.Sci.U.S.A.*, **100**, 1564-1568.
25. Bell, P.C., Bergsma, M., Dolbnya, I.P., Bras, W., Stuart, M.C., Rowan, A.E., Feiters, M.C. and Engberts, J.B. (2003) Transfection mediated by germini surfactants: engineered escape from the endosomal compartment. *J. Am. Chem. Soc.*, **125**, 1551-1558.
26. Plank, C., Zauner, W. and Wagner, E. (1998) Application of membrane-active peptides for drug and gene delivery across cellular membranes. *Adv. Drug Deliv. Rev.*, **34**, 21-35.
27. Li, W., Nicol, F. and Szoka, F.C., Jr. (2004) GALA: a designed synthetic pH-responsive amphipathic peptide with applications in drug and gene delivery. *Adv. Drug Deliv.Rev.*, **56**, 967-985.
28. Subbarao, N.K., Parente, R.A., Szoka, F.C., Jr., Nadasdi, L. and Pongracz, K. (1987) pH-dependent bilayer destabilization by an amphipathic peptide. *Biochemistry*, **26**, 2964-2972.
29. Wyman, T.B., Nicol, F., Zelphati, O., Scaria, P.V., Plank, C. and Szoka, F.C., Jr. (1997) Design, synthesis, and characterization of a cationic peptide that binds to nucleic acids and permeabilizes bilayers. *Biochemistry*, **36**, 3008-3017.
30. Akinc, A. and Langer, R. (2002) Measuring the pH environment of DNA delivered using nonviral vectors: implication for lysosomal trafficking. *Biotechnol.Bioeng.*, **78**, 503-508.
31. Midoux, P. and Monsigny, M. (1999) Efficient gene transfer by histidylated polylysine/pDNA complexes. *Bioconjugate Chem.*, **10**, 406-411.
32. Yu, W., Pirollo, K.F., Yu, B., Rait, A., Xiang, L., Huang, W., Zhou, Q., Ertem, G. and Chang, E.H. (2004) Enhanced transfection efficiency of a systemically delivered tumor-targeting immunolipoplex by inclusion of a pH-sensitive histidylated oligolysine peptide. *Nucleic Acids Res.*, **32**, e48.
33. Chen, Q.R., Zhang, L., Stass, S.A. and Mixson, A.J. (2001) Branched co-polymers of histidine and lysine are efficient carriers of plasmids. *Nucleic Acids Res.*, **29**, 1334-1340.

34. Le Bihan, O., Chevre, R., Mornet, S., Garnier, B., Pitard, B. and Lambert, O. (2011) Probing the in vitro mechanism of action of cationic lipid/DNA lipoplexes at a nanometric scale. *Nucleic Acids Res.*, **39**, 1595-1609.
35. Tarahovsky, Y.S., Koynova, R. and MacDonald, R.C. (2004) DNA release from lipoplexes by anionic lipids: correlation with lipid mesomorphism, interfacial curvatures, and membrane fusion. *Biophys.J.*, **87**, 1054-1064.
36. Dean, D.A., Strong, D.D. and Zimmer, W.E. (2005) Nuclear entry of nonviral vectors. *Gene Ther.*, **12**, 881-890.
37. Godbey, W.T., Wu, K.K. and Mikos, A.G. (1999) Tracking the intracellular path of poly(ethylenimine)/DNA complexes for gene delivery. *Proc.Natl.Acad.Sci.U.S.A.*, **96**, 5177-5181.
38. Dean, D.A. (1997) Import of plasmid DNA into the nucleus Is sequence specific. *Exp.Cell Res.*, **230**, 293 –302.
39. Rao, N.M. and Gopal, V. (2006) Cell biological and biophysical aspects of lipid-mediated gene delivery. *Biosci.Rep.*, **26**, 301–324.
40. Pedroso de Lima, M.C., Simoes, S., Pires, P., Faneca, H. and Duzgunes, N. (2001) Cationic lipid-DNA complexes in gene delivery: from biophysics to biological applications. *Adv.Drug Deliv.Revs.*, **47**, 277–294.
41. Liang, H., Harries, D. and Wong, G.C.L. (2005) Polymorphism of DNA-anionic complexes reveals hierarchy of ion-mediated interactions. *Proc.Natl.Acad.Sci.U.S.A.*, **102**, 11173-11178.
42. Ferrari, M.E., Rusalov, D., Enas, J. and Wheeler, C.J. (2002) Synergy between cationic lipid and co-lipid determines the macroscopic structure and transfection activity of lipoplexes. *Nucleic Acids Res.*, **30**, 1808-1816.
43. Koltover, I., Salditt, T., Rädler, J.O. and Safinya, C.R. (1998) An inverted hexagonal phase of cationic liposome–DNA complexes related to DNA release and delivery. *Science*, **281**, 78-81.
44. Safinya, C.R. (2001) Structures of lipid–DNA complexes: supramolecular assembly and gene delivery. *Curr.Opin.Struct.Biol.*, **11**, 440-448.
45. Ewert, K., Slack, N.L., Ahmad, A., Evans, H.M., Lin, A.J., Samuel, C.E. and Safinya, C.R. (2004) Cationic lipid-DNA complexes for gene therapy; understanding the relationship between complex structure and gene delivery pathways at the molecular level. *Curr.Med.Chem.*, **11**, 133-149.
46. Lin, A.J., Slack, N.L., Ahmad, A., Koltover, I., George, C.X., Samuel, C.E. and Safinya, C.R. (2000) Structure and structure-function studies of lipid/plasmid DNA complexes. *J. Drug Target.*, **8**, 13-27.
47. Xu, Y., Hui, S.W., Frederik, P. and Szoka, F.C.J. (1999) Physicochemical characterization and purification of cationic lipoplexes. *Biophys.J.*, **77**, 341–353.
48. Marchini, C., Pozzi, D., Montani, M., Alfonsi, C., Amici, A., Amenitsch, H., Candeloro De Sanctis, S. and Caracciolo, G. (2010) Tailoring lipoplex composition to the lipid composition of plasma membrane: A trojan horse for cell entry? *Langmuir*, **26**, 13867-13873.

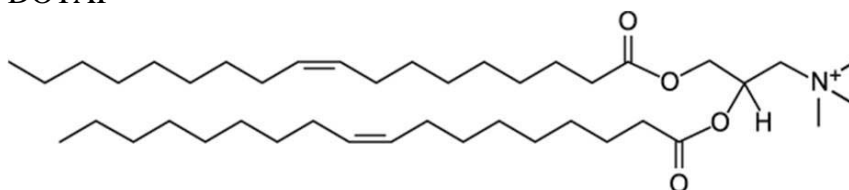
49. Kodama, K., Katayama, Y., Shoji, Y. and Nakashima, H. (2006) The features and shortcomings for gene delivery of current non-viral carriers. *Curr.Med.Chem.*, **13**, 2155-2161.
50. Duguid, J.G., Li, C., Shi, M., Logan, M.J., Alila, H., Rolland, A., Tomlinson, E., Sparrow, J.T. and Smith, L.C. (1998) A physicochemical approach for predicting the effectiveness of peptide-based gene delivery systems for use in plasmid-based gene therapy. *Biophys.J.*, **74**, 2802–2814.
51. Chen, Q.R., Zhang, L., Stass, S.A. and Mixson, A.J. (2000) Co-polymer of histidine and lysine markedly enhances transfection efficiency of liposomes. *Gene Ther.*, **7**, 1698-1705.
52. Chen, Q.R., Zhang, L., Luther, P.W. and Mixson, A.J. (2002) Optimal transfection with the HK polymer depends on its degree of branching and the pH of endocytic vesicles. *Nucleic Acids Res.*, **30**, 1338-1345.
53. Leng, Q. and Mixson, A.J. (2005) Modified branched peptides with a histidine-rich tail enhance in vitro gene transfection. *Nucleic Acids Res.*, **33**, e40.
54. Kichler, A., Mason, A.J. and Bechinger, B. (2006) Cationic amphipathic histidine-rich peptides for gene delivery. *Biochim.Biophys.Acta*, **1758**, 301-307.
55. Read, M.L., Singh, S., Ahmed, Z., Stevenson, M., Briggs, S.S., Oupicky, D., Barrett, L.B., Spice, R., Kendall, M., Berry, M. *et al.* (2005) A versatile reducible polycation-based system for efficient delivery of a broad range of nucleic acids. *Nucleic Acids Res.*, **33**, e86.
56. Gao, X. and Huang, L. (1996) Potentiation of cationic liposome-mediated gene delivery by polycations. *Biochemistry*, **35**, 1027-1036.
57. Sorgi, F.L., Bhattacharya, S. and Huang, L. (1997) Protamine sulfate enhances lipid-mediated gene transfer. *Gene Ther.*, **4**, 961-968.
58. Son, K.K., Tkach, D. and Patel, D.H. (2000) Zero potential of transfection complexes formed in serum-free medium can predict in vitro gene transfer efficiency of transfection reagents. *Biochim.Biophys.Acta*, **1468**, 11-14.
59. Hyndman, L., Lemoine, J.L., Huang, L., Porteous, D.J., Boyd, A.C. and Nan, X. (2004) HIV-1 Tat protein transduction domain peptide facilitates gene transfer in combination with cationic liposomes. *J.Contr.Release*, **99**, 435-444.
60. Rudolph, C., Plank, C., Lausier, J., Schillinger, U., Muller, R.H. and Rosenecker, J. (2003) Oligomers of the arginine-rich motif of the HIV-1 TAT protein are capable of transferring plasmid DNA into cells. *J.Biol.Chem.*, **278**, 11411 – 11418.
61. Rädler, J.O., Koltover, I., Salditt, T. and Safinya, C.R. (1997) Structure of DNA–cationic liposome complexes: DNA intercalation in multilamellar membranes in distinct Interhelical packing regimes. *Science*, **275**, 810-814.
62. Rädler, J., Koltover, I., Jamieson, A., Salditt, T. and Safinya, C.R. (1998) Structure and interfacial aspects of self-assembled cationic lipid-DNA gene carrier complexes. *Langmuir*, **14**, 4272-4283.
63. Koltover, I., Salditt, T. and Safinya, C.R. (1999) Phase diagram, stability, and overcharging of lamellar cationic lipid-DNA self-assembled complexes. *Biophys.J.*, **77**, 915-924.

64. Ma, B., Zhang, S., Jiang, H., Zhao, B. and Lv, H. (2007) Lipoplex morphologies and their influence on transfection efficiency in gene delivery. *J.Control.Release*, **123**, 184-194.
65. Koynova, R., Wang, L. and MacDonald, R.C. (2006) An intracellular lamellar–nonlamellar phase transition rationalizes the superior performance of some cationic lipid transfection agents. *Proc.Natl.Acad.Sci.U.S.A.*, **103**, 14373-14378.
66. Marchini, C., Montani, M., Amici, A., Amenitsch, H., Marianecchi, C., Pozzi, D. and Caracciolo, G. (2009) Structural stability and increase in size rationalize the efficiency of lipoplexes in serum. *Langmuir*, **25**, 3013-3021.
67. Huang, D., Korolev, N., Eom, K.D., Tam, J.P. and Nordenskiöld, L. (2008) Design and biophysical characterization of novel polycationic ϵ -peptides for DNA compaction and delivery. *Biomacromolecules*, **9**, 321-330.
68. Tam, J.P., Lu, Y.A. and Yang, J.L. (2002) Antimicrobial dendrimeric peptides. *Eur.J.Biochem.*, **269**, 923-932.
69. Chen, Q.-R., Zhang, L., Stass, S.A. and Mixson, A.J. (2000) Copolymer of histidine and lysine markedly enhances transfection efficiency of liposomes. *Gene Ther.*, **7**, 1698-1705.
70. Kunath, K., Merdan, T., Hegener, O., Haberlein, H. and Kissel, T. (2003) Integrin targeting using RGD-PEI conjugates for in vitro gene transfer. *J.Gene Med.*, **5**, 588-599.
71. Oberle, V., Bakowsky, U., Zuhorn, I.S. and Hoekstra, D. (2000) Lipoplex formation under equilibrium conditions reveals a three-step mechanism. *Biophys.J.*, **79**, 1447-1454.
72. Jeng, U.S., Su, C.H., Su, C.J., Liao, K.F., Chuang, W.T., Lai, Y.H., Chang, J.W., Chen, Y.J., Huang, Y.S., Lee, M.T. *et al.* (2010) A small/wide-angle X-ray scattering instrument for structural characterization of air-liquid interfaces, thin films and bulk specimens. *J.Appl.Cryst.*, **43**, 110-121
73. Su, C.-J., Chen, H.-L., Wei, M.-C., Peng, S.-F., Sung, H.-W. and Ivanov, V.A. (2009) Columnar mesophases of the complexes of DNA with low-generation poly(amido amine) dendrimers. *Biomacromolecules*, **10**, 773–783.
74. Futaki, S., Suzuki, T., Ohashi, W., Yagami, T., Tanaka, S., Ueda, K. and Sugiura, Y. (2001) Arginine-rich peptides. An abundant source of membrane-permeable peptides having potential as carriers for intracellular protein delivery. *J.Biol.Chem.*, **276**, 5836–5840.
75. Wender, P.A., Mitchell, D.J., Pattabiraman, K., Pelkey, E.T., Steinman, L. and Rothbard, J.B. (2000) The design, synthesis, and evaluation of molecules that enable or enhance cellular uptake: Peptoid molecular transporters. *Proc.Natl.Acad.Sci.U.S.A.*, **97**, 13003-13008.
76. Ignatovich, I.A., Dizhe, E.B., Pavlotskaya, A.V., Akifiev, B.N., Burov, S.V., Orlov, S.V. and Perevozchikov, A.P. (2003) Complexes of plasmid DNA with basic domain 47–57 of the HIV-1 TAT protein are transferred to mammalian cells by endocytosis-mediated pathways. *J.Biol.Chem.*, **278**, 42625–42636.
77. Hashida, H., Miyamoto, M., Cho, Y., Hida, Y., Kato, K., Kurokawa, T., Okushiba, S., Kondo, S., Dosaka-Akita, H. and Katoh, H. (2004) Fusion

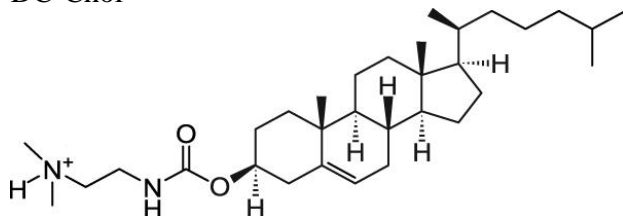
- of HIV-1 TAT protein transduction domain to poly-lysine as a new DNA delivery tool. *Br.J.Cancer*, **90**, 1252–1258.
78. Soundara Manickam, D.S., Bisht, H.S., Wan, L., Mao, G. and Oupicky, D. (2005) Influence of TAT-peptide polymerization on properties and transfection activity of TAT/DNA polyplexes. *J.Control Release*, **102**, 293-306.
 79. Gupta, B., Levchenko, T.S. and Torchilin, V.P. (2005) Intracellular delivery of large molecules and small particles by cell-penetrating proteins and peptides. *Adv.Drug Deliv.Revs.*, **57**, 637-651.
 80. Ross, P.C. and Hui, S.W. (1999) lipoplex size is a major determinant of *in vitro* lipofection efficiency. *Gene Ther.*, **6**, 651-659.
 81. Duguid, J.G., Li, C., Shi, M., Logan, M.J., Alila, H., Rolland, A., Tomlinson, E., Sparrow, J.T. and Smith, L.C. (1998) A physicochemical approach for predicting the effectiveness of peptide-based gene delivery systems for use in plasmid-based gene therapy. *Biophys.J.*, **74**, 2802-2814.
 82. Li, D., Ping, Y., Xu, F., Yu, H., Pan, H., Huang, H., Wang, Q., Tang, G. and Li, J. (2010) Construction of a star-shaped copolymer as a vector for FGF receptor-mediated gene delivery *in vitro* and *in vivo* *Biomacromolecules*, **11**, 2221-2229.
 83. Huebner, S., Battersby, B.J., Grimm, R. and Cevc, G. (1999) Lipid-DNA complex formation: Reorganization and rupture of lipid vesicles in the presence of DNA as observed by cryoelectron microscopy. *Biophys.J.*, **76**, 3158-3166.
 84. Rejman, J., Oberle, V., Zuhorn, I.S. and Hoekstra, D. (2004) Size-dependent internalization of particles via the pathways of clathrin and caveolae-mediated endocytosis. *Biochem.J.*, **377**, 159–169.
 85. Bruinsmaa, R. (1998) Electrostatics of DNA-cationic lipid complexes: isoelectric instability. *Eur.Phys.J.B*, **4**, 75-88.
 86. Caracciolo, G., Pozzi, D., Caminiti, R. and Amenitsch, H. (2006) Formation of overcharged cationic lipids/DNA complexes. *Chem.Phys.Lett.*, **429**, 250-254.
 87. Korolev, N., Lyubartsev, A.P. and Laaksonen, A. (2004) Electrostatic background of chromatin fiber stretching. *J.Biomol.Struct.Dyn.*, **22**, 215-226.
 88. Korolev, N., Lyubartsev, A.P. and Nordenskiöld, L. (2003) Application of the Poisson Boltzmann polyelectrolyte model for thermal denaturation of DNA in the presence of Na⁺ and polyamine cations. *Biophys.Chem.*, **104**, 55-66.

Appendix

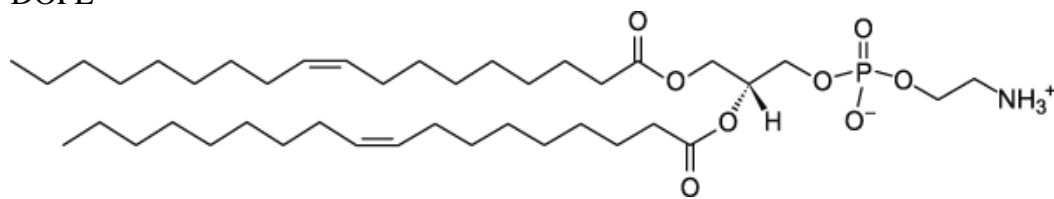
DOTAP



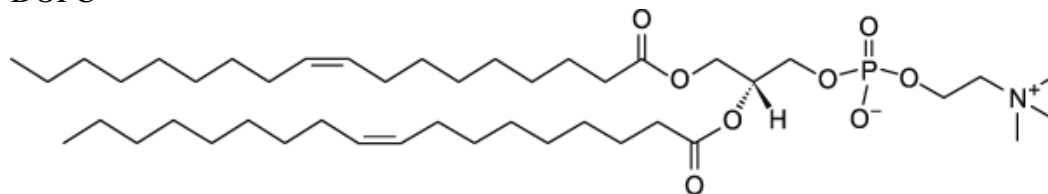
DC-Chol



DOPE



DOPC



Appendix I. Chemical structure of lipids

Buffer used in pH dependence of DNA condensation

pH 5.0	70 mM NaCl, 10 mM citrate; pH 5.0
pH 5.5	70 mM NaCl, 10 mM citrate; pH 5.5
pH 6.0	70 mM NaCl, 10 mM citrate; pH 6.0
pH 6.5	70 mM NaCl, 10 mM citrate; pH 6.5
pH 6.5	70 mM NaCl, 10 mM NaH ₂ PO ₄ ; pH 6.5
pH 6.5	70 mM NaCl, 25 mM Hepes and 0.75 mM Na ₂ HPO ₄ ; pH 6.5
pH 7.0	70 mM NaCl, 10 mM NaH ₂ PO ₄ ; pH 7.0
pH 7.0	70 mM NaCl, 25 mM Hepes and 0.75 mM Na ₂ HPO ₄ ; pH 7.0
pH 7.5	70 mM NaCl, 25 mM Hepes and 0.75 mM Na ₂ HPO ₄ ; pH 7.5
pH 7.5	70 mM NaCl, 10 mM NaH ₂ PO ₄ ; pH 7.5
pH 8.0	70 mM NaCl, 25 mM Hepes and 0.75 mM Na ₂ HPO ₄ ; pH 8.0

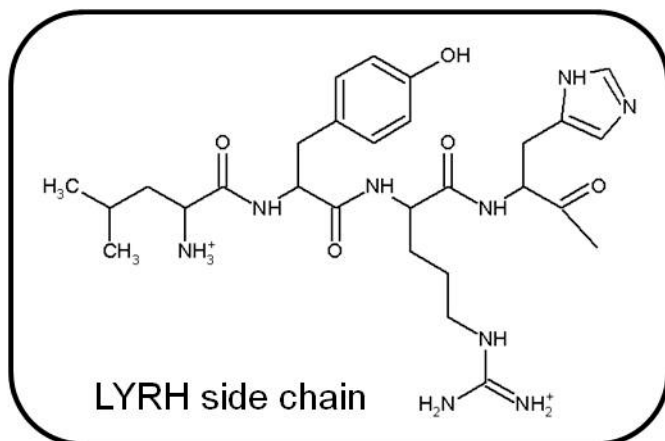
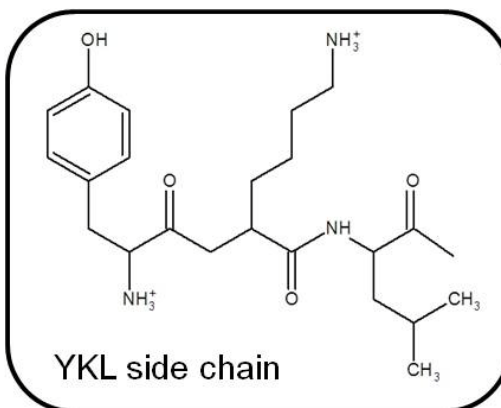
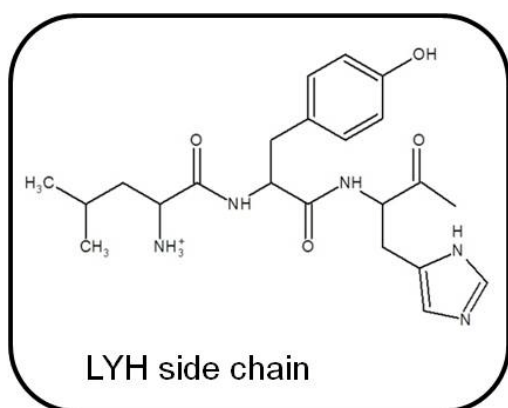
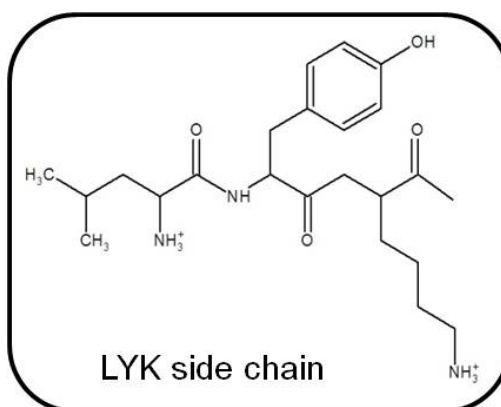
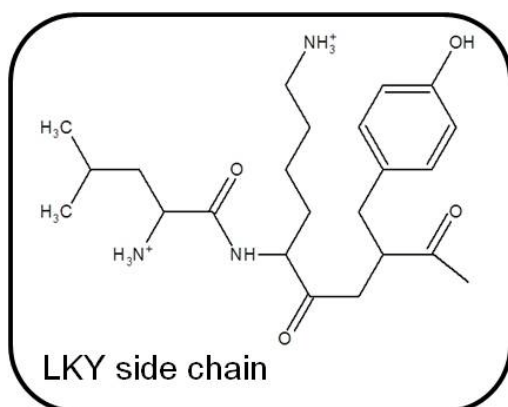
Buffer and media used in cell transfection

HBS	70 mM NaCl, 25 mM Hepes and and 0.75 mM Na ₂ HPO ₄ ; pH 7.05
PBS	137 mM NaCl, 2.7 mM KCl, 4.3 mM Na ₂ HPO ₄ and 1.47 mM KH ₂ PO ₄ ; pH 7.2
Media for cell culture	DMEM supplemented with 10% FBS, sodium pyruvate (100 mM), and L-glutamine (200 mM)

Buffer used in SAXS samples

HBS	70 mM NaCl, 25 mM Hepes and and 0.75 mM Na ₂ HPO ₄ ; pH 7.0
Low-salt buffer	10 mM Hepes and 0.75 mM Na ₂ HPO ₄ ; pH 7.0

Appendix II. Buffer and media recipes



Appendix III. Chemical structure of R' substitution side chains.